Norwegian University
of Life Sciences

Master's Thesis 2019 30 ECTS
Faculty of Science and Technology

Treatment of Municipal Wastewater in a Granular Sludge Reactor: Correlations between Fluorescence Fingerprints of Wastewater and the Behavior of Nutrients During Anaerobic and Aerobic Reactor Phases.

Simen Lunderød Øverbø
Water- and Environmental Technology

Acknowledgements

This thesis represents the end of my studies at the Norwegian University of Life Sciences (NMBU) and is the final work of a five-year Master's Degree Program in Water and Environmental Technology.

Foremost, I would like to thank my thesis advisers Professor Gregory V. Korshin at University of Washington (UW) for support, help and feedback during the work of this thesis during my stay here in Seattle, and Professor Harsha Ratnaweera at NMBU for input and feedback throughout the writing process. Furthermore, a special thanks to the Valle Scholarship and Scandinavian Exchange Program for enabling me to pursue graduate research at UW.

In addition, I would like to thank the experts who were involved in this research project providing invaluable help and support with everything from lab training, sampling and analysis, to data processing and interpretation: Professor Emeritus Knut Kvaal, Matthieu Landreau, Ph.D., and graduate students Maxwell Armenta, John Carter and Gaurav Mahamuni. In addition, I would like to give a special recognition to graduate student Surbhi Malik for the final proofreading of this thesis.

I'm also grateful to Lars Strømnes Engen, Joel Palage and Kristine Sandaa that spent the full academic year in Seattle with me, and to all the Huskies at UW that made this year unforgettable.

Lastly but not the least, I must express my very profound gratitude towards my family and to all my friends at NMBU for providing great support both academically and towards life in general during all these years.

Seattle, August, 2019

Simen Lunderød Øverbø

Abstract

Extensive research has been carried out to ascertain the nature of biological processes involved in the treatment of wastewater in granular sludge reactors. One emerging technology that has the potential to be used to gain a better understanding of the reactors behavior and performance is fluorescence spectroscopy, where the fluorescent components present in the wastewater during the reactor cycles are monitored. However, the changes of the main features of these fluorescence fingerprints, notably the 3D-EEMs, and their relationship with nutrient concentrations during the aerobic and anaerobic phases are currently lacking. This study had an ambition to establish whether there are parameters of the 3D-EEMs from wastewater, or their combinations, that are correlated with and indiciative of the removal of nitrogen and phosphorous via microbiological processes typical for granular sludge reactors.

A pilot sidestream granular sludge reactor performing nitrification and denitrification together with phosphorous removal is operated by researchers at the University of Washington (UW) in collaboration with King County Technology Assessment Program in Seattle, USA. This reactor has been sampled throughout its anaerobic and aerobic phases over a period from beginning of March 2019 to the end of June 2019.

Samples have been analyzed for total ammonia nitrogen, nitrite and nitrate as well as phosphorous concentrations. Fluorescence measurements have been made on a bench-top spectrofluorometer to capture the full 3D-EEMs of the samples. The 3D-EEMs have been processed using fluorescence regional integration (FRI), where four distinct fluorescence regions were identified. Parallel factor analysis (PARAFAC) has also been employed resulting in a two-component PARAFAC-model for both the anaerobic and aerobic phase of the reactor.

The linear relationship between the integrated fluorescence regions and nutrient concentrations, as well as the linear relationship between PARAFAC component relative concentrations and nutrient concentrations was assessed. The observed results indicate great differences between the different sampling series, yet whether these differences are due to seasonal variations or reactor efficacy is not fully understood to this point.

The data show that only the fluorescent region attributed to aromatic proteins with both tyrosine-like and tryphtophan-like substances was observed to have a significant linear relationship ($p<0.05$) with phosphorous in the anaerobic phase. In the aerobic phase, the same region was the only region in the full cycle profiles observed to have a significant linear relationship ($p<0.05$) with the nutrient concentrations throughout the whole sampling period.

In addition, distinct fluorescent regions in the 3D-EEMs were observed to have a stronger linear relationship with the nutrient concentration compared to the total recorded fluorescence spectra in the aerobic phase. This was observed for varying regions, but the region attributed to aromatic proteins with both tyrosine-like and tryphtophan-like substances was observed to have a stronger linear relationship than the total fluorescence spectra on all the full cycle series of the reactor.

In the context of monitoring wastewater treatment processes, fluorescence spectroscopy is still far from its full potential, and the use of bigger data sets in future studies would allow the application of a wide range of statistical models to provide useful insights to the reactor performance.

Sammendrag

Omfattende studier har blitt gjennomført for å forstå de biologiske prosessene som inngår i behandling av avløpsvann i bioreaktorer med granulært slam. En teknologi på fremmarsj som har potensiale til å bidra til en bedre forståelse av en bioreaktors virkemåte og effektivitet er fluorescensspektrometri, hvor fluorescerende komponenter i avløpsvannet overvåkes gjennom reaktorens syklus. Kunnskap om endringene i disse fluorescerende "fingeravtrykkene", kalt "3D-EEM", og deres forhold med konsentrasjonen av næringsstoffer i avløpsvannet gjennom den anaerobe og aerobe fasen i reaktoren er mangelfull. Denne studien har forsøkt å fastslå om det er parametere fra "3D-EEM"-ene til avløpsvann, eller kombinasjoner av disse, som korrelerer med og kan være med å indikere fjerning av nitrogen og fosfor gjennom de mikrobiologiske prosessene som er karakteristiske for en bioreaktor bestående av granulært slam som opererer med satsvise sykluser.

Forskere ved University of Washington (UW) drifter et sidestrøms pilotanlegg i samarbeid med King County Technology Assessment Program i Seattle, USA. Bioreaktoren gjennomfører nitrifikasjon og denitrifikasjon samt fosforfjerning. I perioden fra begynnelsen av mars 2019 og frem mot slutten av juni 2019 har det blitt tatt prøver av denne reaktoren både i den aerobe og anaerobe fasen.

Prøvene har blitt analysert for total ammonium nitrogen-, nitritt-, nitrat- og fosforkonsentrasjoner. Målinger av fluorescens har blitt gjennomført på lab med et spektrofluorometer for å analysere prøvenes fulle "3D-EEM"-er. Disse "3D-EEM"-ene har så blitt prossessert ved å integrere de respektive fluorescerende regionene i "3D-EEM"-ene, og det ble i denne studien observert fire fluorescerende regioner. Parallell faktor analyse (PARAFAC) har også blitt brukt til analyse av prøvene, hvilket resulterte i en PARAFAC-modell bestående av to komponenter både i den anaerobe og aerobe fasen til reaktoren.

Det lineære forholdet mellom de integrerte fluorescensregionene og næringsstoffkonsentrasjonene, samt det lineære forholdet mellom PARAFAC komponentenes relative konsentrasjon og næringsstoffkonsentrasjon ble studert. De observerte resultatene indikerte

svært store forskjeller mellom de ulike prøveseriene. Om disse forskjellene skyldes sesongvariasjoner eller reaktorens effektivitet er ikke fullt ut forstått på nåværende tidspunkt.

Kun den fluorescerende regionen knyttet til aromatiske proteiner med både tyrosin- og tryptofan-lignende substanser var observert til å ha et signifikant ($p<0.05$) lineært forhold til fosforkonsentrasjonen i den anaerobe fasen. I den aerobe fasen var dette den eneste regionen blant prøvene som dekket hele reaktorens syklus som ble observert til å ha et signifikant ($p<0.05$) lineært forhold med næringsstoffkonsentrasjonene gjennom hele prøvetakingsperioden.

Videre var enkelte fluorescerende områder i "3D-EEM"-ene observert til å ha et sterkere lineært forhold med næringsstoffkonsentrasjonene sammenlignet med det totale registrerte fluorescensspekteret i den aerobe fasen. Dette ble også observert for forskjellige områder, men området assosiert med aromatiske proteiner med både tyrosin- og tryptofan-lignende substanser var observert til å ha et sterkere lineært forhold enn det totale fluorescensspekteret for alle seriene som dekket fulle reaktorsykluser.

Fluorescensspektrometri er i denne sammenhengen, behandling av avløpsvann, langt fra å nå sitt fulle potensial, og bruken av større datasett i fremtidige studier vil åpne for muligheten til å benytte seg av en rekke statistiske modeller som har potensiale til å gi ytterligere informasjon om bioreaktorens effektivitet.

Table of Contents

List of Figures

List of Tables

List of Acronyms

3D-EEM	Three dimensional excitation-emission matrix
ABA	Absorbance based approach
ALE	Alginate-like exopolysaccharides
BOD	Biochemical oxygen demand
COD	Chemical oxycen demand
DO	Dissolved oxygen
DOM	Dissolved organic matter
EBPR	Enhanced biological phosphorous removal
EPS	Extracellular polymeric substances
FRI	Fluorescent regional integration
GAO	Glycogen accumulating organisms
IFE	Inner filtering effect
MBBR	Moving bed biofilm reactor
MBR	Membrane bioreactor
NDN	nitrification-denitrification
NDN-OHO	Nitrification-denitrification and ordinary heterotrophic organisms
NDN-PAO	Nitrification-denitrification and phosphorous accumulating organisms
NH_3-N	Ammonia nitrogen
NIT	Nitrification
NO_2-N	Nitrite nitrogen
NO_3-N	Nitrate nitrogen
OHO	Ordinary heterotrophic organisms
OM	Organic matter
ORP	Oxidation-reduction potential
PARAFAC	Parallel factor analysis

PCA	Principal component analysis
PLS	Partial least squares
PO_4-P	Orthophosphate as phosphorous
rbCOD	Readily biodegradable chemical oxygen demand
RU	Raman units
SBR	Sequencing batch reactor
SRT	Solids retention time
TAN	Total ammonia nitrogen
TOC	Total organic carbon
TP	Total phosphorous
TSS	Total suspended solids
WAS	Waste activated sludge
WGAS	Waste granular activated sludge
WWTP	Wastewater treatment plant

1. Introduction

1.1 Background

Treatment of municipal wastewater has previously been related mainly to the removal of biochemical oxygen demand (BOD) and total suspended solids (TSS) (Tchobanoglous et al., 2014). In recent decades, more stringent discharge standards have resulted in the need for rehabilitation and construction of new and improved wastewater treatment plants, with special emphasis on nutrient removal to comply with even stricter discharge permits (Vassos, 1993). Several physical, chemical and biological treatment processes have been developed to meet the new treatment requirements. (Tchobanoglous et al., 2014).

With time, several improvements to the traditional activated sludge process such as moving bed biofilm reactor (MBBR) and membrane bioreactor (MBR) have been developed (Tchobanoglous et al., 2014). One recent improvement to the traditional activated sludge process using flocculent sludge is granular activated sludge, where bacteria are grown into densely-structured and large granules. Granular activated sludge is already used in several full-scale plants worldwide, but the applications of granular sludge to existing continous flow systems to improve treatment performance of existing plants has not been assessed. The dense granules can be separated from the existing solids retention time (SRT) and be maintained at higher SRTs both promoting new granule growth and the maintenance of the added granules. The added granules will then be able to oxidize ammonia (nitrification) and thus enable nitrification even though the floc SRT in the system is low (Figdore, 2017)

Researchers at the University of Washington (UW) Civil Environmental Engineering Department are currently operating a pilot sidestream granular growth reactor in collaboration with King County Technology Assessment Program at King County West Point Treatment Plant, a treatment plant performing BOD removal trough activated sludge process and treating the wasted activated sludge (WAS) by anaerobic digestion. The digested solids are then dewatered trough centrifugation, resulting in a centrate

stream with a high ammonia concentration. This centrate stream is used to grow granules in the pilot reactor with the goal of improving nutrient removal (Figdore, 2017).

The performance of wastewater treatment plants is highly sensitive to environmental factors and conditions varying with time. Previously, the operation of treatment plants was dependent on experienced operating staff that had developed a "feel" for the processes at that particular plant. The introduction of more advanced treatment technologies has required the incorporation of sensors for monitoring and automating the treatment processes (Vassos, 1993). Nevertheless, the difficulty of continuous monitoring of both nitrogen, phosphorous and organics in the wastewater treatment plants still leaves wastewater treatment monitoring lacking sufficient controlling parameters (Li et al., 2008a). The use of off-line monitoring is both time consuming, and lacks the high resolution needed to provide adequate monitoring of the wastewater quality and treatment performance (Bourgeois et al., 2001) as well as resulting in a significant delay between the time of sampling and analysis. The use of on-line measurements will result in the possibilities of better control and early detection of abnormal situations (Al-Dasoqi et al., 2011).

Today, only a few on-line monitoring sensors are currently employed for sequencing batch reactors (SBRs) control such as easy to measure parameters like temperature, pH, dissolved oxygen (DO) and oxidation-reduction potential (ORP) where these parameters can be used to monitor the process stages for nitrogen and phosphorous removal indirectly (Li et al., 2008a). Additional parameters used to monitor treatment performance include flowrate, conductivity and probably ammonium and nitrate as a result of technological advancements (Haimi et al., 2013). Recent developments in data science and computing power have resulted in the emergence of soft-sensors, where easy-to-measure variables are processed to predict hard-to-measure variables such as chemical oxygen demand (COD) and total phosphorous (TP) (Wang et al., 2019).

As part of the development of new technologies in an attempt to improve the on-line monitoring of wastewater treatment processes, fluorescence spectroscopy has emerged as a potentially useful tool for monitoring wastewater treatment processes (Carstea et al., 2016). Parameters typically used to evaluate effluent quality, such as COD, total organic carbon (TOC) and biochemical oxygen demand (BOD) have been observed to correlate well with fluorescent components, and therefore suggesting that the use of fluorescence spectroscopy is a helpful and powerful tool in monitoring the treatment efficacy in wastewater treatment plants (Carstea et al., 2016; Cohen et al., 2014; Henderson et al., 2009).

The fluorescent components have also shown to correlate well with the total microbial activity in water. Especially the protein-like fluorescence have been shown to portray

the efficiency of the biological treatment process (Cohen et al., 2014). In addition, fluorescence spectroscopy has also shown its potential as a surrogate tool for detecting emerging trace organic compounds (Sgroi et al., 2017).

Recent studies have found weak but statistically significant correlations between the protein-like fluorescent components in the effluent of a wastewater treatment plant and, on the other hand, ammonium and total kjeldal nitrogen (TKN) (Riopel et al., 2014). In addition, information from fluorescence spectroscopy when coupled to multivariate statistical analysis (partial least squares (PLS), principal component analysis (PCA) and parallell factor analysis (PARAFAC)), has shown potential to replace other operating parameters such as phosphorous and nitrogen (Galinha et al., 2011; Galinha et al., 2012). Nevertheless, Korshin et al. (2018) highlights that the need for development and implementation of spectroscopic methods for water quality monitoring is still far from its full potential. To this date, only a few studies have assessed on-line monitoring of wastewater treatment processes through fluorescence monitoring (Galinha et al., 2011; Carstea et al., 2018).

One of the big challenges in the application of fluorescence as a monitoring tool is the numerous factors that affect the fluorescence signal. These include inner filter effects (IFEs), fouling, and quenching due to changes in pH, temperature and metal ion presence (Carstea, 2012; Lakowicz, 2006; Henderson et al., 2009; Hudson et al., 2007). In addition, the presence of scattering effects is especially prominent in wastewater samples, resulting in fluorescent regions being dominated by scattering rather than fluorescence (Carstea et al., 2016). These shifts in fluorescence peak positions make the choice of simple wavelength pairs difficult as these peak locations might vary due to the effects mentioned above, and numerous peak positions may be reported (Carstea et al., 2016).

Through the use of a bench-top spectrofluorometer, a three-dimensional excitation-emission matrix (3D-EEM) can be acquired covering a wide range of excitation/emission wavelength pairs and recorded fluorescence intensities. These 3D-EEMs have shown to have distinct features related to the location of the maxima of the excitation/emission wavelength pairs typically found in wastewater (Korshin et al., 2018) and therefore resulting in a "fingerprint" characteristic of the fluorescent compounds present in the solution. A bench-top spectrofluorometer has the drawbacks of low portability and lower times for spectral acquisition as they provide a wider range of excitation and emission pairs. The use of a benchtop spectrofluorometer is also time-consuming and lab-intensive, as well as 3–4 times the cost of a portable fluorescence sensor (Wasswa et al., 2019). Portable fluorescence sensors exist, but most are only equipped with sensors for a very limited number of fluorescence wavelengths. Sensors such as Turner^{TM} and Seapoint^{TM} typically offers 1-7 excitation/emission pairs (Wasswa et al., 2019).

Nevertheless, the use of a benchtop spectrofluorometer will be beneficial in terms of assessing the most relevant wavelengths and regions to use when selecting portable fluorescence sensors that make real-time data-logging and on-line monitoring possible in the future. The selection of the most relevant regions and wavelength pairs will be beneficial when selecting fluorescent probes to generate predictive models such as PCA or PLS that rely on large datasets for establishing training and prediction models (Li et al., 2008b)

To extract the information provided by the large amount of data generated by fluorescence spectroscopy, techniques such as manual peak-picking, PARAFAC and fluorescent regional integration (FRI) is commonly employed (Carstea et al., 2016; Mesquita et al., 2017). The use of FRI will monitor the intensity of the fluorescent regions typically found in wastewater samples, and these regions have recently been correlated with the presence of emerging trace organic compounds (Sgroi et al., 2017), but the application of FRI and its possible relationship with nutrient parameters as well as the application of PARAFAC modelling and its application to sidestream granular sludge reactors is currently lacking.

To date, studies that quantify the fluorescent "fingerprints" of sidestream granular sludge reactors are missing and much still remains to be understood of the fluorescence fingerprint characteristics and their possible relation with nutrient removal efficacy. There is currently a need for cheap and effective monitoring tools that have the potential of working as surrogates for monitoring the performance of such systems (Korshin et al., 2018). An important step in this direction is to analyze the fluorescent characteristics of such a system in greater detail to better understand these systems and lead the way towards better choices of fluorescent probes for on-line monitoring.

Greater understanding of the changes in the fluorescent fingerprints of a sidestream granular sludge reactor is of great interest for future joint research projects between the University of Washington (UW) and the Norwegian University of Life Sciences (NMBU).

1.1.1 Problem statement

Even though extensive research has been carried out to ascertain the nature of microbiological processes involved in the treatment of wastewater in granular sludge reactors as well as to establish main features of the fluorescence fingerprints, notably 3D-EEMs of wastewater of varying provenance, little is known what changes, if any, of these fingerprints take place in a granular sludge reactor during the anaerobic and aerobic phases of its work.

It is also practically important to establish whether there are parameters of 3D-EEMs of wastewater, or their combinations, that are correlated with and indicative of the removal of nutrients via microbiological processes typical for granular sludge reactors.

1.1.2 Objectives of study

Therefore, the main objectives of this study were to:

1. Monitor and quantify changes of 3D-EEMs from a sidestream granular sludge reactor throughout anaerobic and aerobic phases.
2. Apply PARAFAC and regional integration methods to extract information from the complete 3D-EEMs.
3. Assess the correlations between changes in the 3D-EEMs and nutrient concentrations and evaluate the utility of fluorescence based monitoring as a potential tool for online quantification of the nutrient removal in wastewater treatment operations.

2. Theory

2.1 Wastewater treatment

In the 20^{th} century, the focus of wastewater treatment was mainly related to the removal of constituents from the wastewater that was considered to be a source of contaminants when discharged to the environment. A paradigm shift in the 21^{th} century has now taken place and the wastewater is now considered a renewable and recoverable source of both resources, energy and water. It is also a reasonable assumption that wastewater treatment plants will move towards a position as a net exporter of energy instead of consumers of energy (Tchobanoglous et al., 2014)

2.1.1 Main wastewater treatment methods

Several different treatment methods are used in a wide variety of combinations in wastewater treatment plants depending on what type of treatment goals that are desired. These methods can generally be grouped into three main treatment approaches based upon which constituents are used to be removed.

The relevant unit processes are defined as follows by Tchobanoglous et al. (2014):

- Physical
- Chemical
- Biological

The physical unit processes refer to methods where applied physical forces dominate in the treatment. Typical physical unit processes include filtration, adsorption, sedimentation, flocculation, mixing and screening (Tchobanoglous et al., 2014).

Chemical unit processes includes the addition of chemicals or the use of other chemical reactions. Common chemical unit processes include gas transfer such as the addition of oxygen for aerobic reactions, disinfection via the addition of chlorine, and precipitation through the addition of a precipitate. The final precipitate will in most cases contain constituents swept out of the wastewater during settling as well as the constituents that reacted with the added precipitate. The removal of the precipitate is mostly through filtration, membrane processes or settling (Tchobanoglous et al., 2014).

2.1.2 Biological wastewater treatment methods

For municipal wastewater, the activated sludge process, with its roots back to the early 1880s in England, is a commonly used treatment technique that has mainly been designed for 85 % reduction in biochemical oxygen demand (BOD) and total suspended solids (TSS). The design of the activated sludge process has evolved throughout time in response to technological advances, the need for reduced capital and operating costs, research discoveries and the need for nutrient removal and higher-quality effluent (Tchobanoglous et al., 2014).

Together with the developments in both biological and chemical treatment operations as well as membrane technology, typical treatment process flows are illustrated in figure 2.1 on the facing page, where 2.1-(a) and 2.1-(b) depicts conventional biological treatment trains for the removal of BOD and TSS where 2.1-(b) has the addition of biological nutrient removal for the removal of nitrogen and phosphorous. Figure 2.1-(c) illustrates typical advanced treatment trains that follows the tertiary effluent from 2.1-(a) or 2.1-(b). Figure 2.1-(d) shows the treatment of sludge from the biological treatment steps as well as the sludge from the primary sedimentation steps (Tchobanoglous et al., 2014).

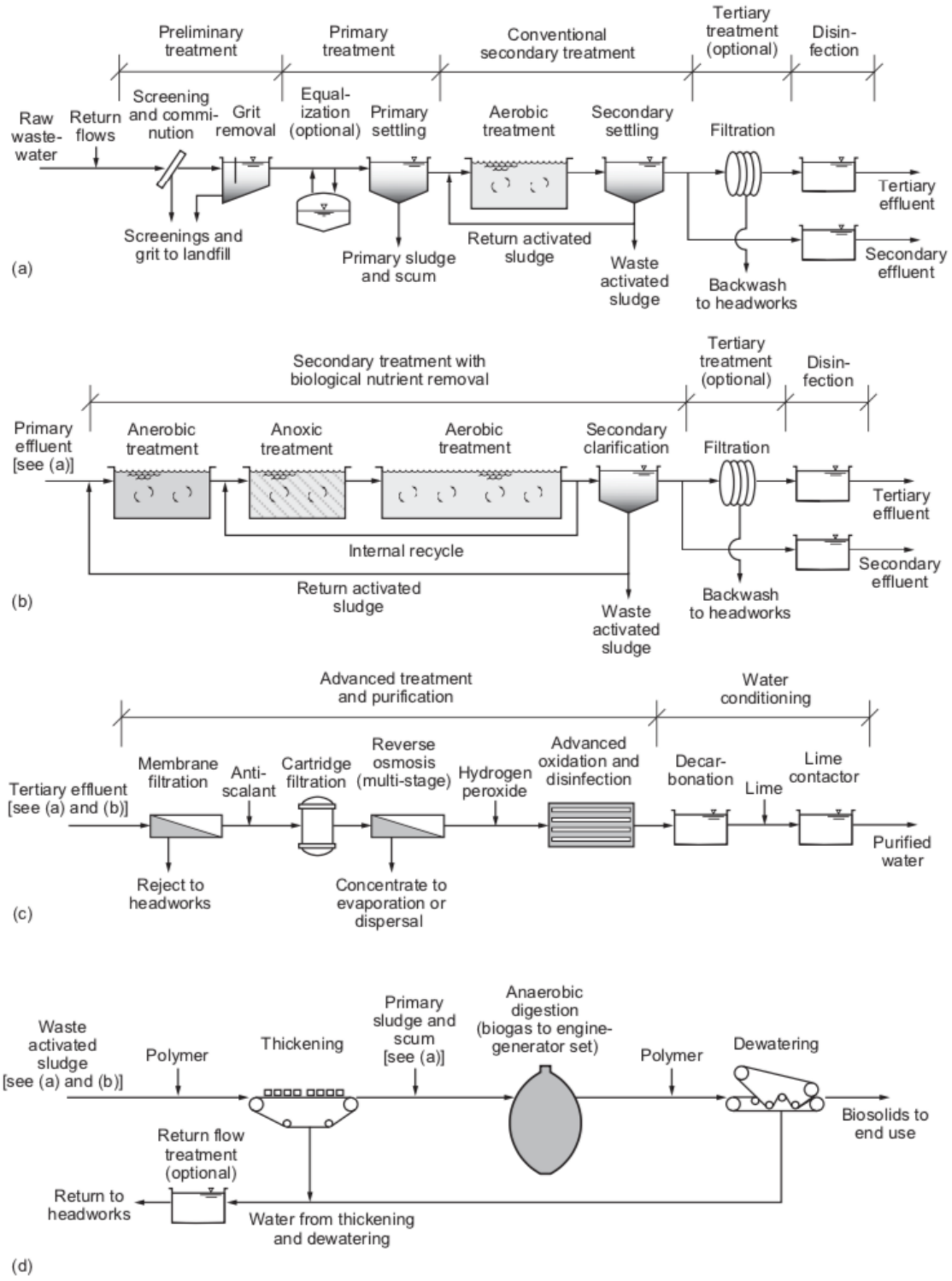

Figure 2.1: Typical wastewater and biosolids treatment flow diagrams (adapted from Tchobanoglous et al. (2014))

2.1.3 Biological nutrient removal

Wastewater treatment plants act as point sources of large nutrient loads to the recieving waterbodies (Tchobanoglous et al., 2014). These heavy anthropogenic loads to aquatic ecosystems may cause eutrophication, where algal blooms results in the production of toxins, odor and taste compounds, fish kills and hypoxic zones (Oglesby and Edmondson, 1966). The limiting macronutrient for the growth of algae is typically nitrogen in marine and brackish water bodies, and phosphorous in fresh water bodies (Conley et al., 2009). As a consequence, regulatory discharge permits have been implemented to protect the receiving ecosystems.

Both chemical and biological removal technologies exist for phosphorous removal, and minimal modifications are needed when upgrading traditional activated sludge wastewater treatment plants to meet the stricter phosphorous discharge permits. However, when nitrogen removal is required, a biological treatment option is the preferred treatment technology over physical-chemical treatment options (Figdore, 2017). The rate-limiting step in ammonia removal is related to nitrification, which is the biological oxidation of ammonia to nitrate, which also depends on the solids retention time (SRT). Implementing biological nitrogen removal usually requires multiple times the tank volume as ordinary BOD removal (Tchobanoglous et al., 2014), thus resulting in large space requirements and associated construction costs.

Several technologies have been developed to achieve biological nutrient removal notably membrane bioreactors (MBRs). What most of these biological technologies have in common is that they mainly increase the MLSS concentration in the reactor (Figdore, 2017). More advanced treatment processess such as anaerobic ammonium oxidation, Anammox, have also been developed to increase nitrogen removal capacity (Tchobanoglous et al., 2014).

A high ammonia nitrogen (NH_3-N) concentration (700 to 1500 mg/L) reject stream from sludge dewatering after mesophilic anaerobic digestion might account for 15–30 % of the total nitrogen load being returned to the secondary treatment operation. This reject stream is called centrate when centrifugation has been used for dewatering, and processess concerning the treatment of the centrate can greatly reduce the NH_3-N load. The centrate can even add nitrifying bacteria back to the secondary treatment process to enhance nitrification of existing BOD plants. This enables increased nitrification capacity in traditional flocculent activated sludge plants. Such improvements may even be required in the future to handle higher influent flow loads and to be able to meet lower NH_3-N discharge limits (Figdore, 2017).

2.1.4 Aerobic granular activated sludge

Through the use of selective pressures, such as applying short settling times of less than 5 minutes in SBRs (Figdore, 2017), up-flow liquid/solids separation (Tsuneda et al., 2003) or trough screening/sieving (Liu et al., 2014) the formation of aerobic granules of around 0.5–3mm in diameter is possible. Aerobic granular activated sludge is defined by Figdore (2017) as *"[...] an attached growth or biofilm process where carrier media is not required and rapidly-settling microbial granules containing a consortium of microorganisms are formed via application of key selective pressures [...]"*. The structural and functional difference between a typical sludge floc and aerobic granular sludge can be seen in figure 2.3, and a photomicrograph of aerobic granular sludge can be seen in figure 2.2.

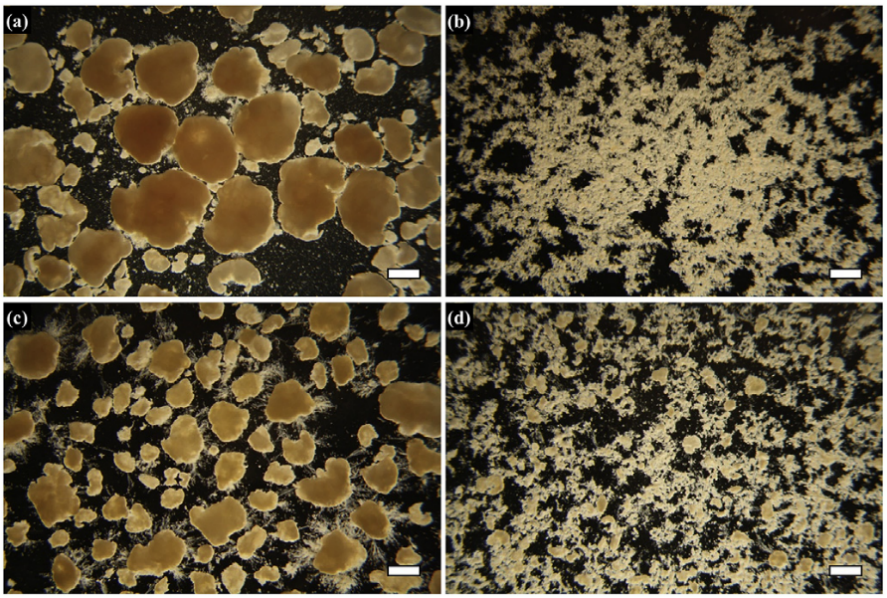

Figure 2.2: 6× magnification photomicrographs of sidestream granules at the beginning (a) and end (c) of bioaugmentation as well as mainstream flocs at the beginning (b) and end (d) of bioaugmentation. (scale bars: 1 mm) (adapted from Figdore et al. (2018b))

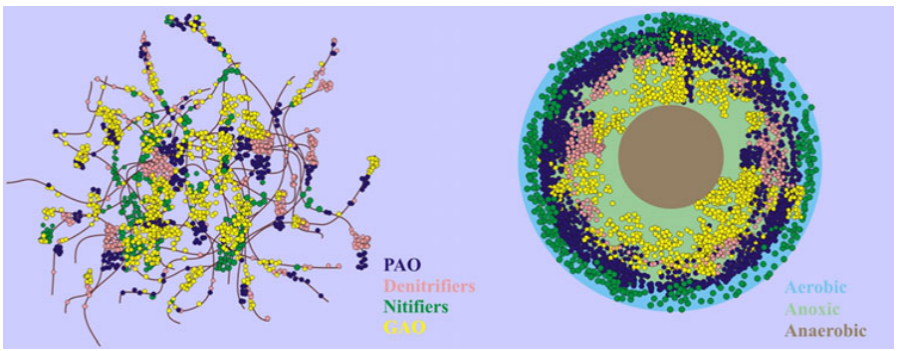

Figure 2.3: Structural and functional difference in aerobic granular sludge and sludge floc (adapted from Winkler et al. (2013))

Different growth conditions and biological processes occurring in the granule result in typically four broad types of aerobic granules (Figdore, 2017):

- Nitrification granules (NIT granules)
- Ordinary heterotrophic organisms granules (OHO granules)
- Nitrification-denitrification and ordinary heterotrophic organisms granules (NDN-OHO granules)
- Nitrification-denitrification and phosphorous accumulating organisms granules (NDN-PAO granules)

NIT granules perform ammonia and/or nitrite oxidation and are fed mainly by nitrite and ammonia. These granules do not perform any significant nitrogen removal as they are related to nitrification only. OHO granules remove nitrogen, but the removal is through nitrogen assimilation resulting from growth on carbon substrates as these granules grow with aerobic feeding and thus, limited denitrification. The heterotrophic organisms that use the carbon substrates are termed ordinary heterotrophic organisms (OHOs). NDN-OHO granules perform nitrification and denitrification but do not have anaerobic conditions promoting PAO/GAO growth, instead OHOs use the carbon substrates. NDN-PAO granules are grown under conditions selecting for both phosphorous accumulating organisms (PAOs) and nitrifying and denitrifying organisms. This results in granules that perform both nitrification-denitrification (NDN) and enhanced biological phosphorous removal (EBPR) (Figdore, 2017). As NDN-PAO granule technology is already applied to full-scale plants, they are described in greater detail below.

NDN-PAO granules

NDN-PAO granules are currently in use in approximately 40 plants as of 2017 including those under construction (Pronk et al., 2017). These full-scale SBR reactors are available under the brand name Nereda® (Giesen et al., 2013).

The main location and role of the key microbial groups in the NDN-PAO granules is shown in figure 2.4 on the next page.

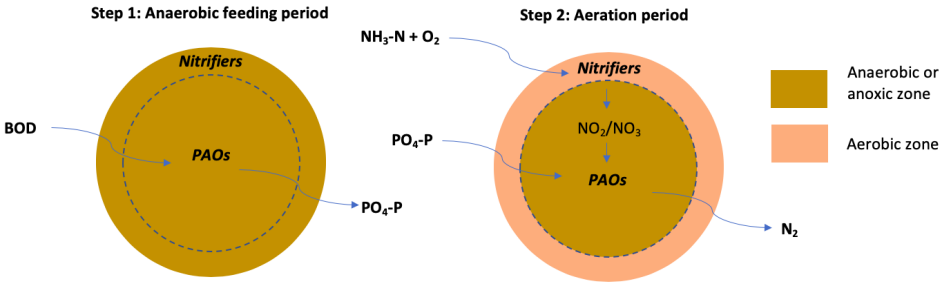

Figure 2.4: Location and role of key microbial groups in NDN-PAO granules (adapted from Figdore (2017))

In the anaerobic phase of the SBR cycle, influent readily biodegradable chemical oxygen demand (rbCOD) is assimilated and stored by PAOs. The rbCOD diffuses into the core of the granule in this anaerobic feast period, and at the same time, PO_4-P is released into the bulk liquid. In the next step the nitrifiers, ammonia oxidizing bacteria (AOBs) and nitrite-oxidizing bacteria (NOBs), oxidize ammonia to nitrite/nitrate in the outer aerobic layer (Figdore, 2017). The NOx produced by the nitrifiers during the aeration period can penetrate into the anoxic part of the granule. Here the NOx is used as an electron acceptor and the stored substrate from the feast period can be used for denitrification in the famine period. This anoxic growth resulting in the removal of nitrogen and phosphorous uptake is illustrated trough equation 2.1 from De Kreuk et al. (2006):

$$\text{stored COD} + \text{NO}_x + \text{PO}_4^{3-} -> \text{N}_2 + \text{CO}_2 + \text{H}_2\text{O} + \text{poly-P} \tag{2.1}$$

With growth conditions favouring PAOs, glycogen accumulating organisms (GAOs) may also be growing. Together, PAOs and GAOs are accounting for as much as 85 % of the microbial population. Both PAOs and GAOs have been observed to reduce NO_3-N to N2, but studies indicate that PAOs are primarly responsible for the reduction of NO_2-N to N2, wheras GAOs are mainly responsible for reduction of NO_3-N to NO_2-N. Nevertheless, selection is preferred towards PAOs over GAOs as GAOs does not provide enhanced biological phosphorous removal, and PAOs will therefore provide a more efficient use of the influent carbon. Selection of PAOs over GAOs can be done due to the different settling velocities as GAOs has a lower bacterial density than PAOs. This results in settled sludge having greater abundance of GAOs at the top, and therefore wasting the top portion will selectively remove GAOs (Figdore, 2017). In addition, using acetate as the main substrate will also favor PAO growth over GAOs (De Kreuk et al., 2006).

2.1.5 Bioaugmentation

Through the use of selecting pressures as described in subsection 2.1.4 on page 11, increased nitrification capacity can be achieved in existing treatment plants performing BOD removal only by uncoupling the SRT of the bioaugmented granular sludge from the SRT of the existing flocculent sludge. In addition, by growing nitrifiers in a sidestream granular sludge reactor, the granules can be fed to the mainstream system and then retained providing increased nitrification capacity.

The use of granule growth eliminates the need for carrier material and thereby makes pumping from the sidestream reactor to mainstream treatment straightforward (Figdore et al., 2018b). A schematic illustration of such a system can be seen in figure 3.1 on page 25.

Without any need for carrier material, the potential to recover nitrogen and phosphorous as well as methane production from waste granular activated sludge (WGAS) in the same way as for ordinary WAS is possible. In addition, the granular activated sludge contains large amounts of extracellular polymeric substances (EPS). These gel-like matrixes play a key role in the aggregation and adhesion of the microbial community. The EPS consists of biomacromolecules such as proteins, nucleic acids, lipids, polysaccharides and humic substances. These alginate-like exopolysaccharides (ALE) have the potential to be extracted from WGAS and become a low-cost alternative to seaweed-derived alginate (Figdore, 2017). It also has the potential to act as an additional revenue stream for the treatment plant (Pronk et al., 2017).

2.2 Fluorescence spectroscopy

Fluorescence spectroscopy is an optical technique where the absorbance of incident radiation results in an excitation of a loosely-held electron within a molecules double and triple bonds (Henderson et al., 2009). This absorption and excitation of electrons will in some instances be followed by the relaxation of the electron to a stable configuration and thus, stimulating the emission of a photon termed fluorescence. The wavelengths at which the absorption (termed excitation wavelength) and emitted photon wavelength (termed emission wavelength) occurs is located at distinct wavelengths specific to the molecule (Lakowicz, 2006).

Figure 2.5 on the facing page displays the energy transfers involved in fluorescence. Fluorescent organic matter is divided into two categories based upon their reaction to incident radiation – the compounds that absorb light energy are called chromophores,

and those that absorb and then re-emit the light energy are called fluorophores. Prior to emission, some of the energy is "lost" through non-radiative decay, collision and other processes resulting in the emitted photon having a longer wavelength than the original excitation wavelength, a process called the Stokes' Shift (Hudson et al., 2007).

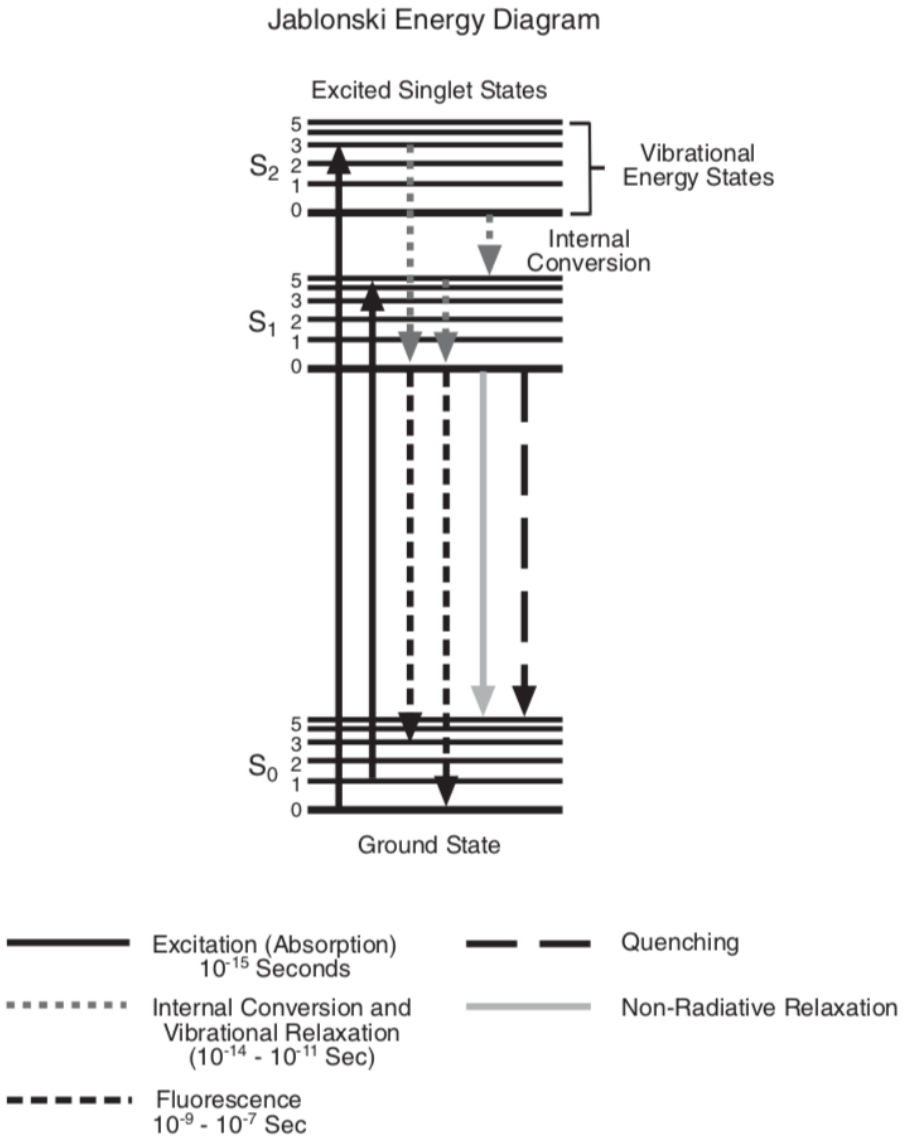

Figure 2.5: Jablonski Energy Diagram (adapted from Hudson et al. (2007))

The excitation and emission wavelengths of the fluorophore are characteristic for their molecular conformation, and at low concentrations the measured peak intensity is directly proportional to the responsible fluorophore concentration in the solution (Henderson et al., 2009). This specific feature of fluorescence makes single-molecule detection possible and results in a sensitivity in the range of 10-1000x compared to that of UV absportion spectroscopy, an already commercialized wastewater monitoring technique (Henderson et al., 2009). In addition to the increased sensitivity, the fluorescent meth-

ods are much less affected by turbidity in the medium (Pons et al., 2004).

2.3 Three dimensional excitation-emission matrixes

Fluorescence measurements have traditionally been presented as an emission spectra from irradiation at a fixed excitation wavelength (Lakowicz, 2006). Technological advances in the recent years have enabled the development of a technique where excitation, emission and fluorescence intensity are synchronously scanned over a wide range of wavelengths (Hudson et al., 2007), resulting in a grid consisting of a composite of emission scans from a single sample recorded by incrementing excitation wavelengths (excitation $\times$ emission $\times$ intensity). The resulting three dimensional excitation-emission matrix (3D-EEM) contains large amounts of data from each sample, and thereby enabling the application of a wide range of statistical analysis (Henderson et al., 2009)

3D-EEM fluorescence spectroscopy is a potent and highly sensitive tool for characterizing dissolved organic matter (DOM) in both freshwater, marine water and wastewater. As an optical measurement it have been shown to be a rapid and efficient tool in characterizing DOM structure and chemical composition requiring minimal sample pre-treatment. (Maqbool et al., 2016; Hudson et al., 2007).

Its use as a monitoring tool for different environmental applications has been widely investigated in several engineered systems including process control in wastewater treatment plants, monitoring specific pollutants in industrial wastewater, monitoring oil content in water and the potential of disinfection byproduct formations in drinking water treatment plants (Henderson et al., 2009). The potential applications of fluorescence spectroscopy to water quality monitoring have been addressed in several reviews, but its application to wastewater quality and treatment performance requires additional attention due to its highly complex composition and potential impact on the environment (Carstea et al., 2016).

The highly complex media composition from wastewater treatment plants (WWTPs) results in a wide amount of natural fluorophores, such as amino acids (tryphtophan, tyrosine and phenylalanine), aromatic organic matter (OM), coenzymes and vitamins. In addition, extracellular polymeric substances (EPS) released by cells comprise intra- or extra-cellular fluorescent molecules such as humic-like and protein-like substances that are also detectable by fluorescence spectroscopy (Mesquita et al., 2017). Figure 2.6 on the next page presents an example showing locations of fluorescent peaks that have been manually selected through the peak-picking method.

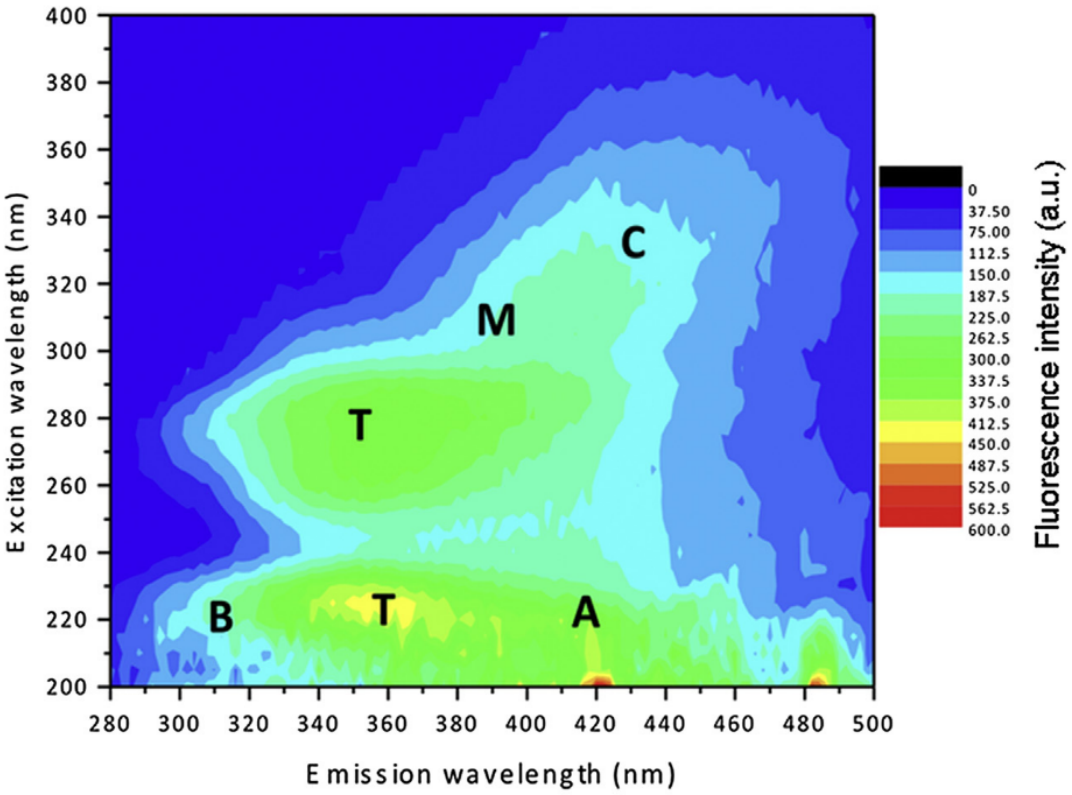

Figure 2.6: Example of an 3D-EEM of a water sample impacted by domestic wastewater with peaks manually identified trough peak-picking method (adapted from Hudson et al. (2007))

There are usually five key fluorescence peaks that's observed in freshwater aquatic samples, and these peaks have been classified by Coble (1996) as follows: Peak A – humic-like; Peak C – humic-like; Peak B – tyrosine-like; Peak T_1 and T_2 – tryphtophan-like; peak M – marine humic-like.

For analyzing wastewater samples, Sgroi et al. (2017) developed five distinct regions that embrace peaks from typical wastewater 3D-EEMs. These regions are based of regions previously defined by Chen et al. (2003) and can be seen in figure 2.7 on the following page and their corresponding wavelength boundaries can be seen in table 2.1 on the next page.

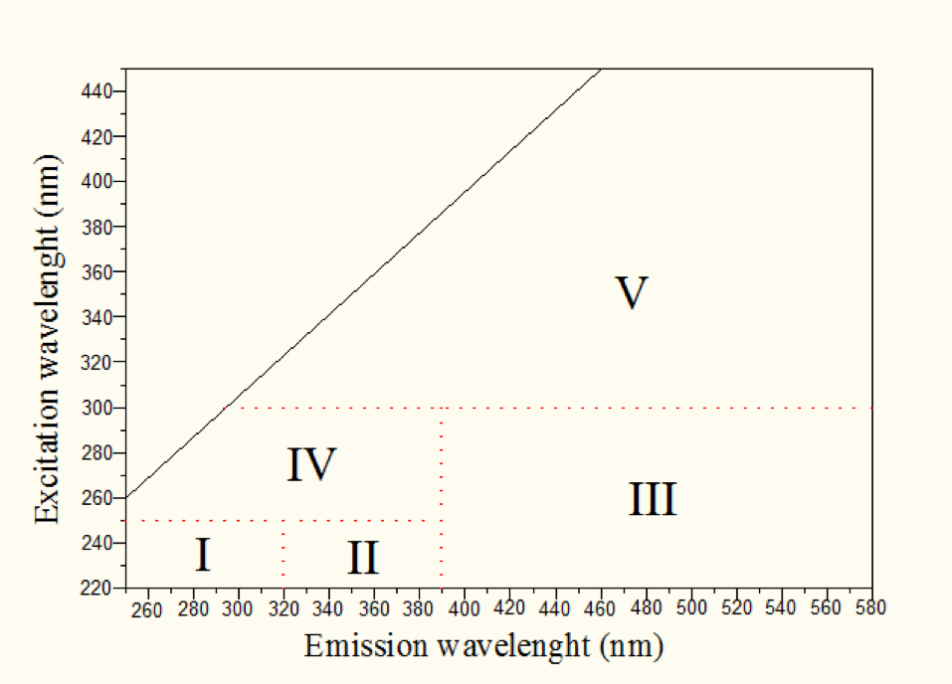

Figure 2.7: Fluorescent regions in an EEM (adapted from Sgroi et al. (2017))

Table 2.1: Fluorescence regions and excitation-emission wavelength boundaries (adapted from Sgroi et al. (2017))

Region	DOM components	Excitation wavelengths boundary (nm)	Emission wavelengths boundary (nm)
I	aromatic proteins, tyrosine-like substances	220–250	250–320
II	aromatic proteins, tryphtophan-like substances	220–250	320–390
III	fulvic-like and humic-like substances	220–300	390–580
IV	microbial byproducts, proteins, tryphtophan-like and biopolymers	250–300	250–390
V	humic-like substances	250–580	300–450

2.4 Matrix effects

The fluorescence signal from a sample can be altered by several environmental factors such as pH, salinity, composition, temperature and concentration (Carstea, 2012). This combined altering of the fluorescence signal through chemical or physical means is referred to as "matrix effects" (Henderson et al., 2009).

2.4.1 Inner filtering effects

The inner filtering effect (IFE) refers to an apparent decrease in emission quantum yield and/or a distortion of bandshape that results from absorption of excited and emitted radiation by the sample matrix (Henderson et al., 2009). IFEs is further divided into:

- Primary inner-filter effect
- Secondary inner-filter effect
- Inner filter effects due to the prescence of other substances

(Carstea, 2012).

These primary and secondary IFEs are illustrated in figure 2.8. The Primary IFE refers to the absorption of the excitation wavelength prior the beam reaching the fluorophore (Carstea, 2012). The secondary IFE occurs when the emitted photons from the fluorophore is reabsorbed before reaching the detector (Ohno, 2002). Finally, when other chromophores are present, they might act as filters as they absorb wavelengths in the same range as the present fluorophores in the solution. To account for these changes in fluorescence intensity, one might apply a correction factor (Valeur, 2001).

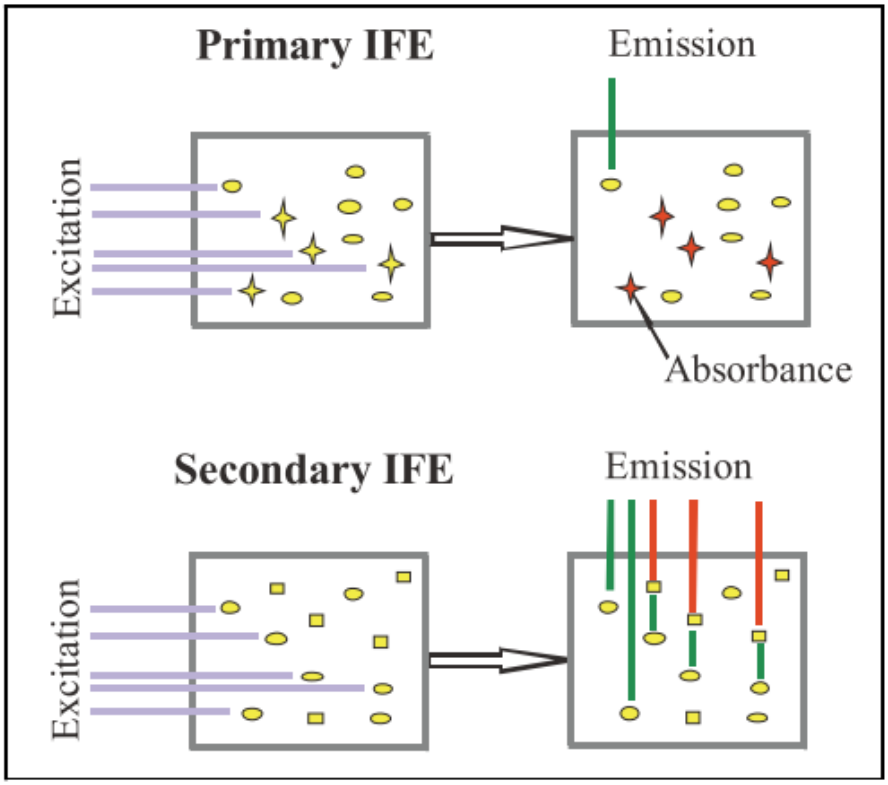

Figure 2.8: Primary and secondary inner filtering effects (adapted from Carstea (2012))

An usual approach to correct for both the primary and secondary IFE includes diluting the sample to ensure that the measured absorbance of the sample is below 0.05, and if absorbance is above 0.05, a mathematical correction might be applied. Several mathematical methods exists (Kothawala et al., 2013), but a commonly applied method is a model by Lakowicz (2006) where it is assumed that the absorbance and fluorescence occur at the midpoint of a 1 × 1 cm cuvette. This absorbance based approach (ABA) assumes that the sum of absorbances at each pair of wavelengths is directly related to suppression of the fluorescence intensity (Kothawala et al., 2013). The corrected absorbance (excitation) and fluorescence (emission) is thus given by the following relationship:

$$\mathrm{F}^{corr}_{\lambda_{\mathrm{ex}}\lambda_{\mathrm{em}}} = \mathrm{F}^{obs}_{\lambda_{\mathrm{ex}}\lambda_{\mathrm{em}}} \times 10^{(0.5\times(\mathrm{A}_{\lambda_{\mathrm{ex}}}\times\mathrm{A}_{\lambda_{\mathrm{em}}}))} \tag{2.2}$$

Where:

- $\mathrm{F}^{corr}_{\lambda_{\mathrm{ex}}\lambda_{\mathrm{em}}}$ is the corrected fluorescence intensity at each pair of excitation (λ_{ex}) and emission wavelength (λ_{em}) in the 3D-EEM
- $\mathrm{F}^{obs}_{\lambda_{\mathrm{ex}}\lambda_{\mathrm{em}}}$ is the measured fluorescence intensity at each excitation and emission wavelength pair
- $\mathrm{A}_{\lambda_{\mathrm{ex}}}\times\mathrm{A}_{\lambda_{\mathrm{em}}}$ is the measured absorbance at each excitation and emission wavelength pair

2.4.2 Quenching of fluorescence

Any process that decreases the fluorescence intensity of a molecule is referred to as fluorescence quenching, and due to the variable and complex composition of wastewater, potential influences of fluorescence quenching due to variability in pH, temperature and metal ions should therefore be evaluated (Henderson et al., 2009).

pH quenching

According to a review by Patel-Sorrentino et al. (2002), three fluorescence quenching effects due to changes in pH are hypothesized:

- competition between metal ions and H^+
- alteration of the excitable electrons molecular orbitals
- changes of macromolecular configuration of humic substances

The competition between metal ions and H^+ results in complexation-decomplexation processes that may quench fluorescence. The alteration of the molecular orbitals is due to the ionization of excitable electrons after pH alteration. Finally, the macromolecular configuration is related to the fact that humic substances coil at lower pH, and this coiled configuration could quench present fluorophores (Carstea, 2012).

Furthermore, a review by Henderson et al. (2009) observes an increase in the range of 0 to <30 % for all fluorescent peaks in the 3D-EEM with increasing pH, however, the effect is reversible in the range of pH 2–12 and is considered unimportant if the pH range is small (<2 units). In addition, Henderson et al. (2009) also highlights the fact that alterations in pH will impact the solubility of metal ions (see "Metal ions quenching" section below).

Metal ions quenching

Depending on the effluent chemistry, any wastewater can contain significant concentrations of heavy metals such as mercury and copper, most of it originating from industrial sources (Ahluwalia and Goyal, 2007). In addition, chemical treatment processes such as coagulation, as well as metals leaching from pipeworks due to processess such as corrosion might also introduce metals to the system (Henderson et al., 2009).

Complexation of the fluorescent molecules with metal ions is mostly attributed to the humic substances and less to the amino acids (Carstea, 2012). However, Henderson et al. (2009) reports the need for further research as studies report varying conclusions as well as most studies consider laboratory experiments with addition of free metal ions, whereas the metals in wastewater might be in organo-colloidal or particulate form. Reynolds and Ahmad (1995) conclude as well after reviewing the effect of metal ions on the fluorescence of sewage wastewater, that the final effluent from sewage plants exhibits little fluorescence quenching but pollution incidents may introduce large metal concentrations that will affect the observed fluorescence.

Temperature quenching

Temperature is considered the most important fluorescence quencher in the case of wastewater as increasing temperature is determining the electrons within a molecule to return to their ground state through a radiationless process, and therefore decreasing the fluorescence (Carstea, 2012). Henderson et al. (2009) reports strong fluorescence quenching of DOM fluorescence intensity with respect to temperature where every 1 °C

rise in temperature in the range of 10–45 °C results in a 1 % decrease in peak T (humic-like substances) and peak C (tryphtophan-like substances).

Even though the temperature effects strongly impact the fluorescence response, it is easily corrected for by either:

- applying correction factors
- performing fluorescence analysis at a constant temperature

(Henderson et al., 2009)

As the temperature effects are reversible and linear (Vodacek and Philpot, 1987), correction factors may be applied. However, different fluorophores might need different correction factors related to their size fractions (Seredyńska-Sobecka et al., 2007). Due to seasonal variability in wastewater temperature, the use of correction factors might need to be developed further.

2.4.3 Scattering effects

Peaks resulting from water scattering might interfere with the quantitative analysis as well as the visualization of 3D-EEMs. There are three types of scattering that might interfere with the acquired 3D-EEM: Rayleigh scattering, Tyndall scattering and Raman scattering (Zepp et al., 2004). Examples of scattering effects can be seen in Figure 2.9.

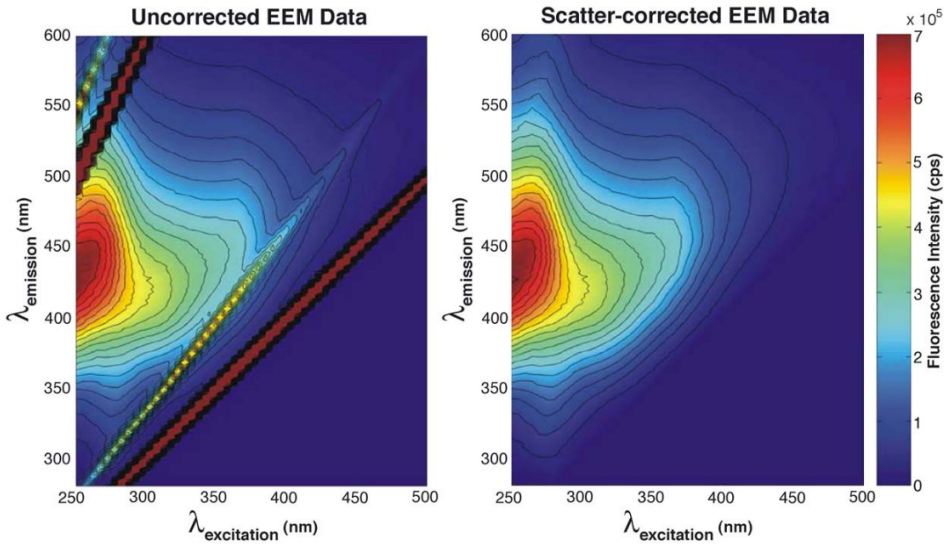

Figure 2.9: Example of scattering effects in an 3D-EEM (adapted from Zepp et al. (2004))

Rayleigh scattering

Both Rayleigh and Tyndall scatter peaks occur in the 3D-EEMs at the same wavelength as the excitation light (Zepp et al., 2004). The Rayleigh scatter is a result of light scattering due to particles and molecules with a smaller size than the wavelength of the excitation light and does not represent any energy loss. This results in elastic scatter where the scattered light has the same wavelength as the excitation wavelength (Carstea, 2012). In addition to the scatter with the same wavelength, termed 1st order Rayleigh scatter, the presence of 2nd order Rayleigh scattering will be visible at emission wavelength = 2 × excitation wavelength (Hudson et al., 2007). The 2nd order Rayleigh scattering is due to the way the monochromator used for excitation of the fluorophores is constructed (Carstea, 2012). The Rayleigh scattering efficiency varies approximately in inverse proportion to the fourth power of the exciting wavelength (Zepp et al., 2004).

Tyndall scattering

Tyndall scattering originates from reflection of particulate matter in the analyzed sample and can be greatly reduced through filtration of the sample (0.2-μm) (Zepp et al., 2004).

Raman scattering

The Raman scatter line is considered an optical manifestation of the scattering properties of water originating from vibration of the covalent molecular O—H bonds when applying light energy. (Hudson et al., 2007). The Raman scattering is an inelastic scatter, meaning that the emitted wavelength will be longer than the excitation wavelength. The Raman scattering line will manifest itself as a diagonal line in the 3D-EEM with an increasing systematic deviation from the Rayleigh-Tyndall scatter line (Carstea, 2012). The Raman scattering is generally a lot less intense than the Rayleigh scattering (Zepp et al., 2004)

Its location in the 3D-EEM is at $\lambda_{ex}/\lambda_{em}$ = 260–350/280–400 nm, and due to its proximity to tyrosine-like fluorescence, its fluorescence properties might be obscured by the Raman scattering line (Hudson et al., 2007). The tyrosine-like peak, peak B (Coble, 1996), is therefore rarely analyzed in detail in wastewater samples due to the potential of scattering interference (Carstea et al., 2016).

3. Materials and Methods

3.1 Pilot Sidestream Granular Sludge Reactor

The pilot-scale sidestream treatment reactor is located at King County West Point wastewater treatment plant in Seattle, USA. The sidestream reactor is part of a bigger pilot plant, and as of this report, it is still under construction. The full pilot treatment plant schematic can be seen in figure 3.1

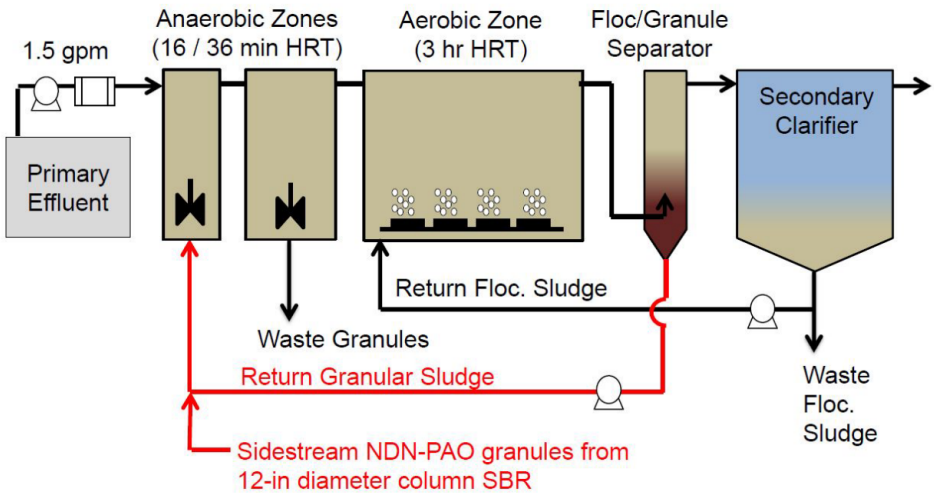

Figure 3.1: Schematic view of pilot mainstream process (adapted from Figdore et al. (2018a))

The sidestream reactor, a SBR reactor, is column-shaped with a 12-inch nominal diameter of SCH80 clear PVC pipe. The reactor liquid volume is 176L at full liquid level (2.44m). Treated effluent is discharged at the 50 % level. The discharge valve can be seen as the top valve in figure 3.4 on page 27.

A schematic view can be seen in figure 3.2 on the following page.

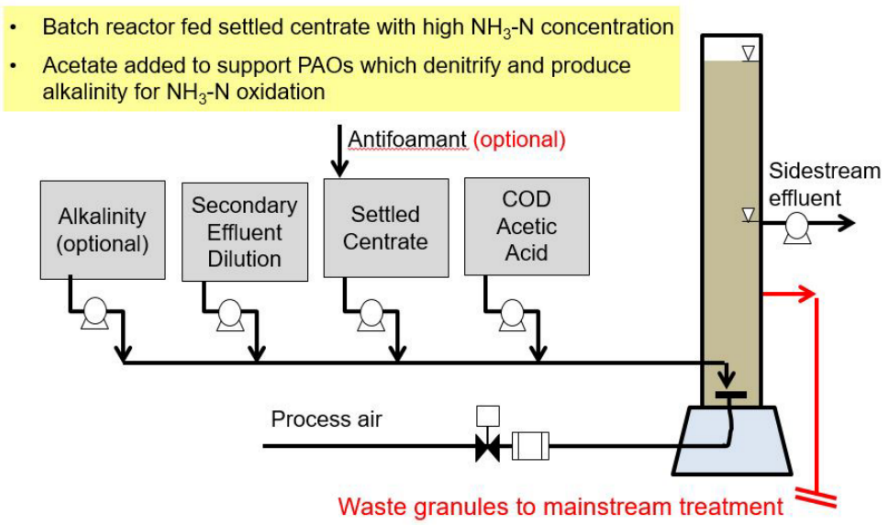

Figure 3.2: Schematic view of a sidestream granular sludge reactor (adapted from Figdore et al. (2018a))

The SBR-cycle is 6 hours in total, and its control circuit timing can be seen in figure 3.3.

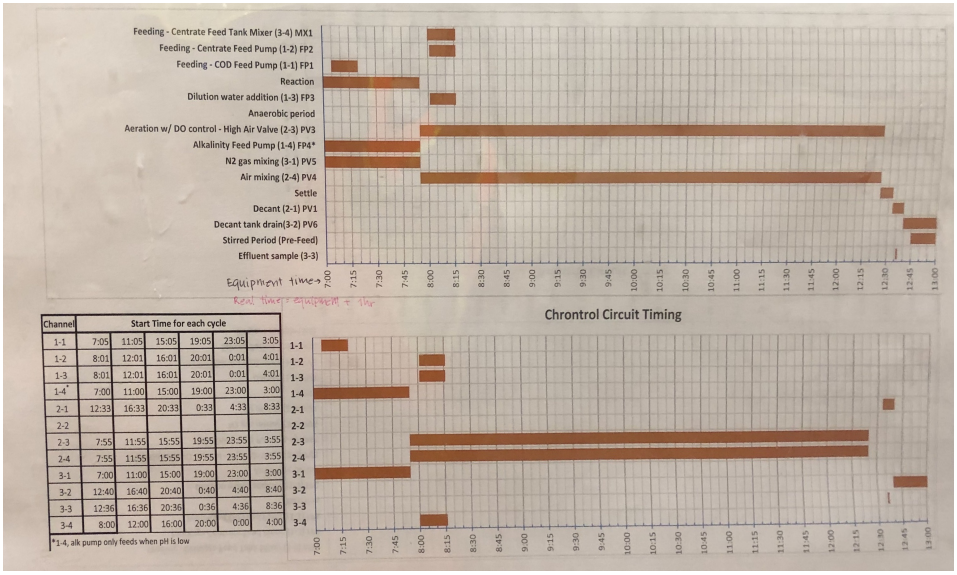

Channel	Start Time for each cycle					
1-1	7:05	11:05	15:05	19:05	23:05	3:05
1-2	8:01	12:01	16:01	20:01	0:01	4:01
1-3	8:01	12:01	16:01	20:01	0:01	4:01
1-4*	7:00	11:00	15:00	19:00	23:00	3:00
2-1	12:33	16:33	20:33	0:33	4:33	8:33
2-2						
2-3	7:55	11:55	15:55	19:55	23:55	3:55
2-4	7:55	11:55	15:55	19:55	23:55	3:55
3-1	7:00	11:00	15:00	19:00	23:00	3:00
3-2	12:40	16:40	20:40	0:40	4:40	8:40
3-3	12:36	16:36	20:36	0:36	4:36	8:36
3-4	8:00	12:00	16:00	20:00	0:00	4:00

Figure 3.3: Control circuit timing of NDN-PAO reactor

The anaerobic phase is initiated with unaerated COD fed with a <1.0L concentrated sodium acetate solution. This results in a minimal change in liquid level in the reactor and a high F/M ratio. Dilution effects due to COD feeding are therefore considered to be negligible. The reactor is sparged with nitrogen gas to ensure mixing of the reactor contents.

The aerobic phase is initiated with aeration and the addition of aerated secondary effluent dilution water from the treatment plant and centrate from the digesters at the plant. The secondary effluent and centrate are stored in separate day tanks. Centrate

is obtained three times per week and screened trough a 425 μm sieve prior to storage in the day tank. DO is controlled between 1.5 and 2.1 mg/L during aeration. Average air flow rate during aeration have been 5.24 L/min since January 2019.

The aeration is followed by a 7-minute settling period followed by a 3-minute gravity discharge down to the 50 % liquid level. A 25-minute unmixed period then follows intended to allow for enhanced denitrification. The cycle ends with 5 minutes of nitrogen gas sparging prior to the COD feed in the following cycle.

The reactor is shown in figure 3.4, shaded with a yellow color. Acetate is fed from the green tank, decant effluent is discharged to the orange tank and dilution water and centrate day tanks are shown in blue and purple respectively.

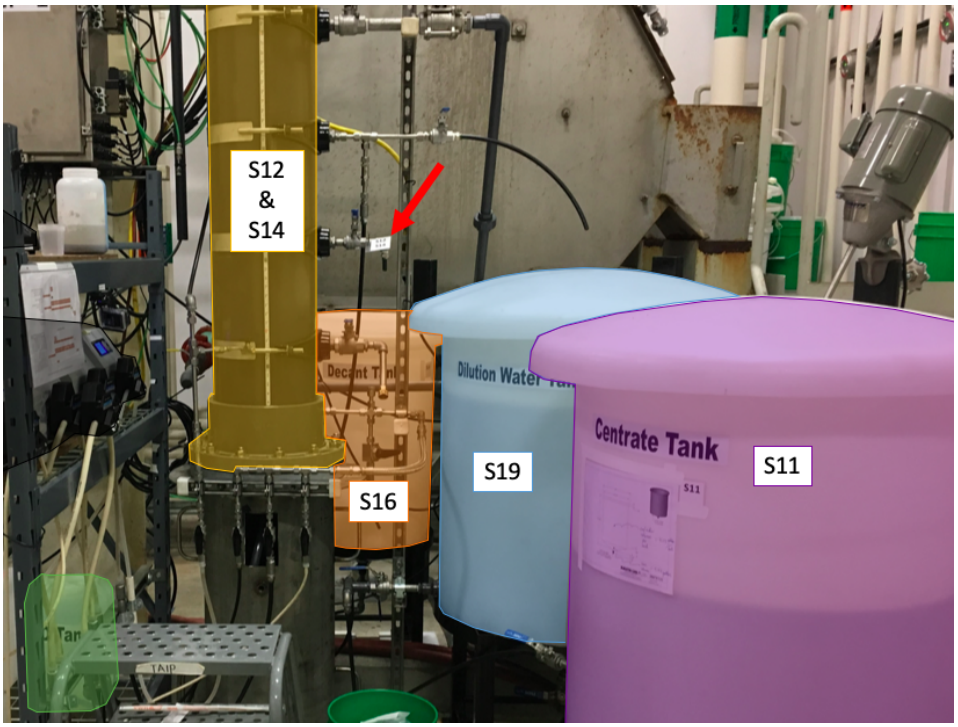

Figure 3.4: Picture of sidestream reactor (photo: Maxwell Armenta)

The reactor consists of NDN-PAO granules which shown in figure 3.5 on the next page. Note the fast settling time as this photo was taken shortly after sampling the granules.

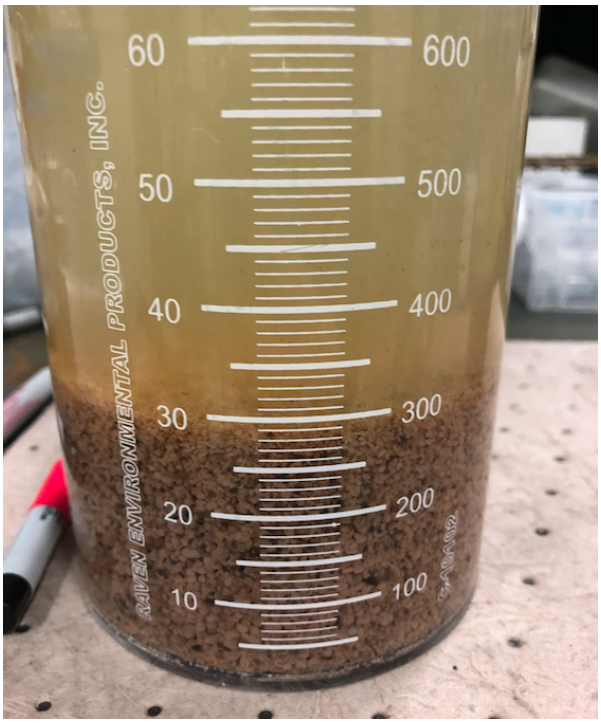

Figure 3.5: Picture of NDN-PAO granules (photo: Simen Lunderød Øverbø)

3.2 Sampling

The sampling of the sidestream granular sludge reactor has been performed in the period March–June 2019. Sampling has been performed in such a way as to being able to capture potential seasonal variations. As part of this project being coupled with the work of another graduate student's research project at the University of Washington, the sampling has been divided into the following two types of sampling series:

- full-cycle series
- mini-series

The full-cycle series cover the full anaerobic and aerobic phases of the reactor and consis of approximately 10 samples from each phase. The mini-series provide a smaller snapshot of the reactor's performance and consists of 2 samples from the anaerobic phase (start and stop) as well as approximately 4 samples from the first 1-2 hours of the aerobic phase. These data sets have been further divided into anaerobic phase and aerobic phase as the reactor operates at half the reactor volume during the anaerobic phase and full volume in the aerobic phase.

Consequently, the mini-series do not provide a high-resolution monitoring of the anaerobic cycle. As only the first 1-2 hours of the aeration phase is covered, only the ammonia

removal rate is measured in the aeration phase. Phosphorous concentration is measured for the anaerobic phase. Nevertheless, the mini-series are routinely sampled, and thus are expected to still provide useful insight to the analysis of the fluorescent properties of the samples.

The full-cycle series have been sampled on the following days:

- 2019-03-07
- 2019-05-30
- 2019-06-25

The mini-cycle series have been sampled on:

- 2019-04-25
- 2019-04-29
- 2019-05-02
- 2019-05-06
- 2019-05-09
- 2019-05-17
- 2019-05-24

Please note that no mini-cycle series have been sampled in June due to external time constraint factors resulting in the prioritizing of one full-cycle series over multiple mini-series.

Samples taken during the aerobic and anaerobic phase have been obtained from the valve with the red arrow shown in figure 3.4 on page 27. Samples taken during the anaerobic phase have been labeled with S12. Datum for these time-series have been set to the start of acetate feeding and the end is before aeration starts. Samples from the aerobic phase have been labeled with S14 and the datum for these time series has been set to the end of the dilution water and centrate feed.

These samples have been stored at 4°C prior to analysis. For the full-cycle series, orthophosphate as phosphorous (PO_4-P) , ammonia nitrogen (NH_3-N), nitrite nitrogen (NO_2-N) and nitrate nitrogen (NO_3-N) have been analyzed externally by graduate student Maxwell Armenta at the University of Washington. Nutrient analysis has been performed after filtration of the samples (0.45 μm), on the Gallery^{TM} Analyzer from Thermo Scientific^{TM}. ORP, pH and temperature is monitored on-line. It should be

noted that ammonia nitrogen is reported here as NH_3-N even though ammonia nitrogen exists in aqueous solution in equilibrium as either ammonia gas (NH_3) or ammonium ion (NH_4^+) (Tchobanoglous et al., 2014). Most ammonia nitrogen in wastewater is in the form of NH_4^+ (Tchobanoglous et al., 2014), and the Gallery^{TM} Analyzer measures total ammonia nitrogen (TAN) but it will be reported here as NH_3-N as this has been previous practice at UW.

3.3 3D-EEM Processing

To assess the potential of fluorescence spectroscopy as an online monitoring tool, the samples have not been altered through dilution or filtration. As highlighted by Galinha et al. (2012), several studies have assessed the information of specific fluorescent compounds that are present in the media through analysis of compounds such as extracellular polymeric substances (EPS) extracted from wastewater samples. However, the whole sample may also contain important information and should therefore not be excluded a priori.

Fluorescence measurements have been performed using a Horiba Aqualog® spectrofluorometer following standard operating procedures. The scanning range of excitation wavelengths was 200–600nm with an 1nm increment and the emission wavelength was from 245.16–826.06nm with an 2.33nm increment (4 pixel binning). Integration time was set to 0.5s and CCD gain to medium. The spectrofluorometer was turned on 20-30 minutes prior to analysis to allow proper time for the lamp to heat up. Samples were at the same time removed from the 4°C cooler to allow them to reach room temperature and reduce potential temperature effects.

Samples have been blank-subtracted with a recorded blank containing Milli-Q® water to remove Raman scatter peaks and normalized to the area under the Raman peak (excitation wavelength 350nm and emission wavelength 390–420nm) into Raman units (RU). After blank subtraction, negative values and 0-values are set to 10^{-12} to enable log-plots if needed.

3.3.1 Matrix Effects

To reduce the potential scatter effects, additional post-processing has been performed in MATLAB® through a script developed by Zepp et al. (2004). The script can be found in full in the referenced article. In short, the script improves the Rayleigh and Raman scattering removal over the conventional blank-subtraction technique, where remaining

scatter peaks are excised and replaced using the Delaunay triangulation technique for a three-dimensional interpolation of the remaining data.

For inner filtering effects corrections, the use of equation (2.2) and the absorbance based approach has been assessed.

Processed 3D-EEMs can be seen in full in appendix A on page 63.

3.3.2 Fluorescence Regional Integration

For quantification of the recorded 3D-EEM fluorescence intensity, the fluorescence regional integration technique has been assessed. The technique, developed by Chen et al. (2003) divides the 3D-EEM into five operationally defined regions through consistent excitation and emission wavelength boundaries. These regions have been adapted and slightly modified following regions proposed by Sgroi et al. (2017); these regions can be seen in table 2.1 on page 18.

After comparing the proposed regions from Sgroi et al. (2017), some overlap between region I and II has been recorded (see figure 3.6) for typical 3D-EEM peaks observed in the aerobic and the anaerobic phase. This overlap has resulted in the combination of region I and II into one region "I+II" comprising aromatic proteins with both tyrosine-like and tryphtophan-like substances.

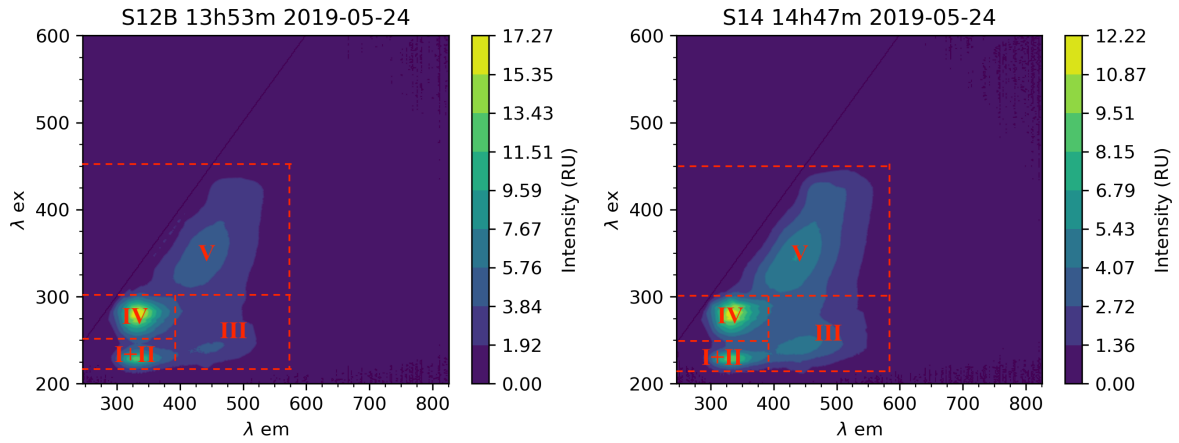

Figure 3.6: Selection of regions for FRI

With these defined regions, the total volume Φ_v under region V will always be greater than volume Φ_{III} under region III. To account for this effect, the volumetric integration of each region is normalized to the projected excitation and emission area for each region resulting in a normalized region-specific 3D-EEM intensity volume.

The FRI technique from Chen et al. (2003) integrates the area beneath the 3D-EEM. The volume (Φ_i) beneath region "i" is given by:

$$\Phi_i = \int_{ex} \int_{em} I\left(\lambda_{\mathrm{ex}}\lambda_{\mathrm{em}}\right) \mathrm{d}\lambda_{\mathrm{ex}}\mathrm{d}\lambda_{\mathrm{em}} \tag{3.1}$$

For discrete data, the volume (Φ_i) beneath region "i" is given by:

$$\Phi_i = \sum_{\mathrm{ex}} \sum_{\mathrm{em}} I\left(\lambda_{\mathrm{ex}}\lambda_{\mathrm{em}}\right) \Delta\lambda_{\mathrm{ex}}\Delta\lambda_{\mathrm{em}} \tag{3.2}$$

Where:

- $\Delta\lambda_{\mathrm{ex}}$ is the excitation wavelength interval and
- $\Delta\lambda_{\mathrm{em}}$ is the emission wavelength interval
- $I\left(\lambda_{\mathrm{ex}}\lambda_{\mathrm{em}}\right)$ is the recorded fluorescence intensity at each excitation/emission wavelength pair

The normalized excitation-emission area volumes ($\Phi_{i,n}$, $\Phi_{\mathrm{T,n}}$) were calculated as follows:

$$\Phi_{i,n} = \mathrm{MF}_i\Phi_i \tag{3.3}$$

$$\Phi_{\mathrm{T,n}} = \sum_{i=1}^{4} \Phi_{i,\mathrm{n}} \tag{3.4}$$

The multiplication factor (MF_i) for each region is equal to the inverse of the fractional projected excitation-emission area. In addition, through normalization of the regions, the effects of dominance of shoulders resulting from the extension of peaks from secondary or tertiary excitation/emission responses is reduced (Chen et al., 2003).

The percent fluorescence response ($P_{i,\mathrm{n}}$) were calculated as follows:

$$P_{i,\mathrm{n}} = \frac{\Phi_{i,\mathrm{n}}}{\Phi_{\mathrm{T,n}}} \times 100\% \tag{3.5}$$

The calculated FRI parameters can be seen in table 3.1 on the facing page. $\Delta\lambda_{ex}$ and $\Delta\lambda_{em}$ are set prior to scanning the sample on the Horiba Aqualog® spectrofluorometer.

These increments were set to:

- $\Delta\lambda_{ex} = 1$ nm
- $\Delta\lambda_{em} = 2.33$ nm

Table 3.1: FRI parameters

3D-EEM region	**no. of data points per region**	**projected ex/em area (nm^2)**	**fractional projected area**	**MF$_i$**
I+II	1984	4622.72	0.033	29.991
III	6642	15475.86	0.112	8.959
IV	3213	7486.29	0.054	18.519
V	47664	111057.12	0.801	1.248
sum	59503	138641.99	1.000	

3.3.3 PARAFAC modeling

PARAFAC is a commonly used techinque for modeling and visualizing complex multivatirate data. Compared to PCA, another commonly used technique, PARAFAC has the advantage of providing both qualitative and quantitative model of the data over just the qualitative characterization from PCA. PARAFAC has the additional advantage of separating the complex signal measured into its individual underlying fluorescent phenomena with its specific excitation and emission spectra (Stedmon and Bro, 2008).

The approach of PARAFAC modeling of 3D-EEMs is described in great detail by Stedmon and Bro (2008) and Bro (1997). In essence, PARAFAC decomposes N-way arrays into N loading matrices. 3D-EEMs are multi-way (three-way), and combining the data from a series of samples will result in a three-way box of data, see figure 3.7 on the next page.

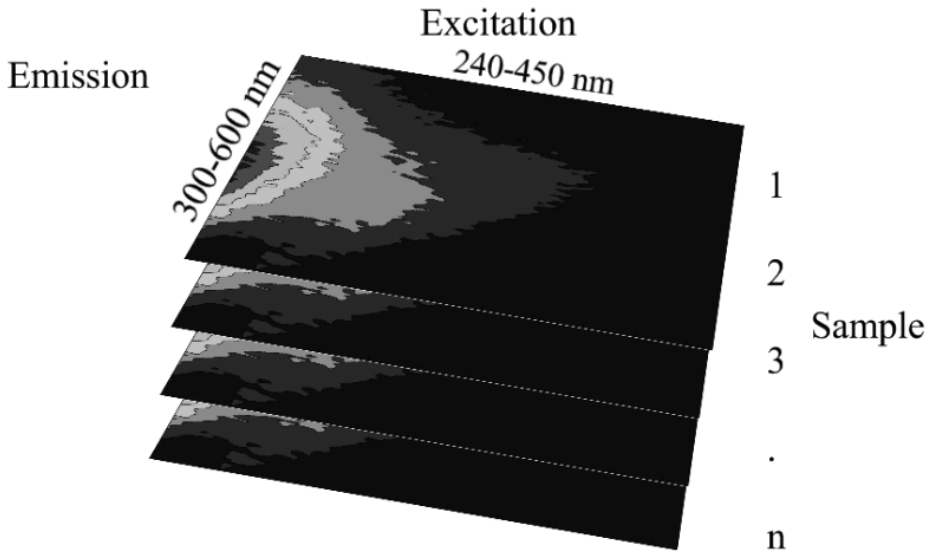

Figure 3.7: Example of a three-dimensional box of 3D-EEM data (adapted from Stedmon and Bro (2008))

The three-way data is then modeled using equation 3.6, by minimizing the sum of squares of the residuals (ε_{ijk}).

$$x_{ijk} = \sum_{f=1}^{F} a_{if} b_{jf} c_{kf} + \varepsilon_{ijk}, i = 1, ., I; j = 1, ., J; k = 1, ., K; \tag{3.6}$$

For the analysis of 3D-EEMs, x_{ijk} is the fluorescence intensity of sample i, measured at emission wavelength j and excitation wavelength k, and ε_{ijk} representing residuals not explained by the model.

The outcome of the PARAFAC model is the parameters a, b, and c. Ideally these parameters represents the concentration, emission spectra and excitation spectra respectively of the underlying analyzed fluorophores (Stedmon and Bro, 2008). A graphical representation of a two-component PARAFAC model of the data array $\mathbf{X}$ can be seen in figure 3.8.

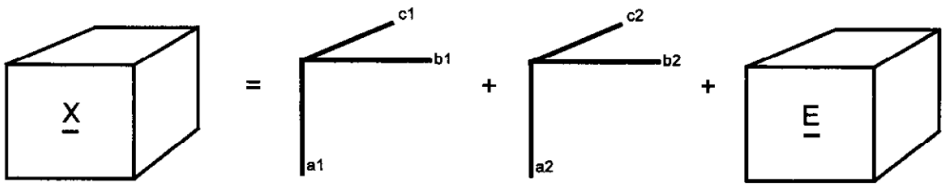

Figure 3.8: Graphical representation of a two-component PARAFAC model of the data array $\mathbf{X}$ (adapted from Bro (1997))

Prior to developing the PARAFAC model, samples were pre-processed as described in

section 3.3 on page 30. The PARAFAC models were generated with the N-way toolbox for MATLAB®.

4. Results and Discussion

4.1 Inner filtering effects

For the inner filtering effects correction, equation (2.2) and the absorbance based approach have been assessed as the recorded absorbance is above 0.05 for several wavelengths.

Figure 4.1 shows the absorbance profile for two samples from the anaerobic and aerobic phase during the 2019-05-30 sample series. High absorbance values at lower wavelengths has been observed for the samples in both the aerobic and anaerobic phase.

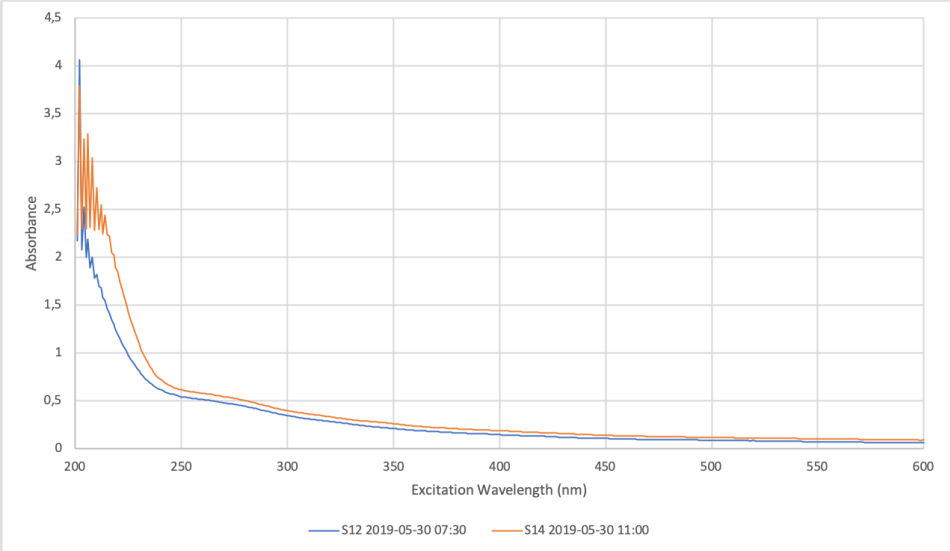

Figure 4.1: Absorbance measurements from anaerobic and aerobic phase

As the absorbance value is greater than 1 at several wavelengths, the use of equation (2.2) introduces too much noise in the recorded 3D-EEM as the intensity in these areas will be greatly exaggerated. Therefore, corrections for IFE have not been applied for the recorded samples. Furthermore, to be able to perform IFE corrections during potential on-line monitoring, additional absorbance measurements will be required besides the fluorescence measurement if equation (2.2) is to be applied.

4.2 March Full Cycle Profile

Results from the 2019-03-07 Cycle profile are provided below. Additional parameters are available in table 4.12 on page 55; these parameters have been provided by graduate student Maxwell Armenta.

4.2.1 March Fluorescence Response and FRI Interpretation

The linear relationship between the nutrient removal rates and the FRI intensity volumes has been assessed as well as the percentage fluorescence response from each region. The recorded intensities from the anaerobic phase can be seen in table B.1 on page 71 together with the recorded PO_4-P values. Table 4.1 on the facing page shows the calculated R^2 values between the FRI intensities and nutrient concentration, and the calculated R^2 values between the percentage fluorescence response and nutrient concentration.

Even though the number of data points are low (n=10), there is a significant relationship ($p<0.05$) between all of the intensity-areas and nutrient concentrations. The strongest relationship (R^2=0.788) is observed in the region attributed to the overall total recorded fluorescence signal, $\Phi_{T,n}$.

The percentage fluorescence response from the region attributed to fulvic- and humic-like substances, region III (Sgroi et al., 2017), showed the strongest relationship with the PO_4-P concentration (R^2=0.812). In addition, the percentage fluorescence response from region IV, attributed to microbial byproducts, proteins, biopolymers and tryphtophan-like substances (Sgroi et al., 2017) did not show any significant linear relationship with the PO_4-P concentration.

Table 4.1: Calculated R^2 of the linear relationship between FRI intensity volumes ($\Phi_{i,n}$), percentage fluorescence response ($P_{i,n}$) and nutrient concentrations for the 2019-03-07 anaerobic cycle profile

	PO_4-P (mg/L)	p-value	n
$\Phi_{\mathrm{I+II},n}$	0.759	**<0.05**	10
$\Phi_{\mathrm{III},n}$	0.607	**<0.05**	10
$\Phi_{\mathrm{IV},n}$	0.758	**<0.05**	10
$\Phi_{\mathrm{V},n}$	0.777	**<0.05**	10
$\Phi_{\mathrm{T},n}$	0.788	**<0.05**	10
$P_{\mathrm{I+II},n}$	0.685	**<0.05**	10
$P_{\mathrm{III},n}$	0.812	**<0.05**	10
$P_{\mathrm{IV},n}$	0.371	>0.05	10
$P_{\mathrm{V},n}$	0.681	**<0.05**	10

Results from the recorded nutrient concentrations and the FRI intensity volumes can be seen in table B.2 on page 71 for the aerobic phase. The calculated R^2 values can be seen in table 4.2. It's worth noting that not all samples were analyzed for PO_4-P, so n=8 for PO_4-P whereas n=13 for the analysis of the inorganic nitrogen species.

Table 4.2: Calculated R^2 of the linear relationship between FRI intensity volumes ($\Phi_{i,n}$), percentage fluorescence response ($P_{i,n}$) and nutrients concentrations for the 2019-03-07 aerobic cycle profile

	PO_4-P (mg/L)	n	p-value	NH_3-N (mg/L)	n	p-value	NO_3-N (mg/L)	n	p-value	NO_2-N (mg/L)	n	p-value
$\Phi_{\mathrm{I+II},n}$	0.896	8	**<0.05**	0.940	13	**<0.05**	0.911	13	**<0.05**	0.966	13	**<0.05**
$\Phi_{\mathrm{III},n}$	0.807	8	**<0.05**	0.894	13	**<0.05**	0.960	13	**<0.05**	0.958	13	**<0.05**
$\Phi_{\mathrm{IV},n}$	0.519	8	**<0.05**	0.608	13	**<0.05**	0.503	13	**<0.05**	0.601	13	**<0.05**
$\Phi_{\mathrm{V},n}$	0.735	8	**<0.05**	0.803	13	**<0.05**	0.918	13	**<0.05**	0.896	13	**<0.05**
$\Phi_{\mathrm{T},n}$	0.885	8	**<0.05**	0.925	13	**<0.05**	0.903	13	**<0.05**	0.956	13	**<0.05**
$P_{\mathrm{I+II},n}$	0.862	8	**<0.05**	0.931	13	**<0.05**	0.945	13	**<0.05**	0.975	13	**<0.05**
$P_{\mathrm{III},n}$	0.741	8	**<0.05**	0.788	13	**<0.05**	0.713	13	**<0.05**	0.799	13	**<0.05**
$P_{\mathrm{IV},n}$	0.643	8	**<0.05**	0.763	13	**<0.05**	0.893	13	**<0.05**	0.833	13	**<0.05**
$P_{\mathrm{V},n}$	0.876	8	**<0.05**	0.922	13	**<0.05**	0.908	13	**<0.05**	0.956	13	**<0.05**

Interestingly enough, as can be seen in table 4.2, the relationship between the FRI intensity values for $\Phi_{\mathrm{IV},n}$ is observed to be the lowest for all recorded nutrient concentrations in the aerobic phase. Region $\Phi_{\mathrm{I+II},n}$, attributed to aromatic proteins, tyrosine- and tryphtophan-like substances (Sgroi et al., 2017) is observed to have the strongest relationship with PO_4-P, NH_3-N and NO_2-N, whereas region $\Phi_{\mathrm{III},n}$, is observed to have the strongest relationship with NO_3-N. As for the anaerobic phase, the observed rela-

tionship between separate regions and nutrient concentration is greater than the overall fluorescence intensity area, $\Phi_{T,n}$. The percentage fluorescence response from region I+II is observed to have the strongest relationship with NH_3-N, NO_2-N and NO_3-N concentration. On the other hand, region V, attributed to humic-like substances (Sgroi et al., 2017) is observed to have the strongest relationship with the PO_4-P concentration. However, it is not observed to be remarkably different from the relationship with the percentage fluorescence response from I+II and PO_4-P concentration (R^2 values of 0.876 and 0.862 respectively).

4.3 May Full Cycle Profile

A summary of the 2019-05-30 Cycle profile is provided below. Additional parameters are available in table 4.12 on page 55, these parameters have also been provided by graduate student Maxwell Armenta.

4.3.1 May Fluorescence Response and FRI Interpretation

The linear relationship between the nutrient removal rates and the FRI intensity volumes and percentage fluorescence response from each region has been assessed for the 2019-05-30 cycle. The recorded intensities from the anaerobic phase can be seen in table B.3 on page 72 together with the recorded PO_4-P values. Table 4.3 on the facing page shows the calculated R^2 values between the FRI intensities and nutrient concentrations.

For the May 30th cycle profile, there is still observed a significant ($p<0.05$) relationship between all of the intensity-areas and the nutrient concentrations in the anaerobic phase. Some independent regions are observed to have a stronger relationship than the sum of all the regions($\Phi_{T,n}$). The strongest relationship is observed in area $\Phi_{III,n}$ and the weakest is observed for area $\Phi_{V,n}$. The percentage fluorescence response from region IV is observed to have the strongest relationship with the PO_4-P concentration, whereas region I+II is observed to have the weakest relationship. However, all percentage fluorescence response regions are observed to have a significant ($p<0.05$) relationship with the PO_4-P concentration for the May 30th cycle profile.

Table 4.3: Calculated R^2 of the linear relationship between FRI intensity volumes ($\Phi_{i,n}$), percentage fluorescence response ($P_{i,n}$) and nutrient concentrations for the 2019-05-30 anaerobic cycle profile

	PO_4-P (mg/L)	p-value	n
$\Phi_{\mathrm{I+II},n}$	0.715	**<0.05**	10
$\Phi_{\mathrm{III},n}$	0.946	**<0.05**	10
$\Phi_{\mathrm{IV},n}$	0.856	**<0.05**	10
$\Phi_{\mathrm{V},n}$	0.689	**<0.05**	10
$\Phi_{\mathrm{T},n}$	0.754	**<0.05**	10
$P_{\mathrm{I+II},n}$	0.536	**<0.05**	10
$P_{\mathrm{III},n}$	0.835	**<0.05**	10
$P_{\mathrm{IV},n}$	0.914	**<0.05**	10
$P_{\mathrm{V},n}$	0.741	**<0.05**	10

For the May 30th aerobic phase, a different relationship is observed. As can be seen in table 4.4 only area $\Phi_{\mathrm{I+II},n}$ is observed to have a significant ($p<0.05$) relationship with all the measured nutrient parameters, and it is the only region that has an observed significant relationship with the measured NO_2-N concentrations. Area $\Phi_{\mathrm{IV},n}$ did not show any significant relationship with any of the measured nutrient concentrations during the May 30th aerobic cycle profile. The percentage fluorescence response from area I+II is also the only area that is observed to have a significant ($p<0.05$) relationship with all of the measured nutrient concentrations.

Table 4.4: Calculated R^2 of the linear relationship between FRI intensity volumes ($\Phi_{i,n}$), percentage fluorescence response ($P_{i,n}$) and nutrients concentrations for the 2019-05-30 aerobic cycle profile

	PO_4-P (mg/L)	n	p-value	NH_3-N (mg/L)	n	p-value	NO_3-N (mg/L)	n	p-value	NO_2-N (mg/L)	n	p-value
$\Phi_{\mathrm{I+II},n}$	0.698	10	**<0.05**	0.654	10	**<0.05**	0.414	10	**<0.05**	0.55	10	**<0.05**
$\Phi_{\mathrm{III},n}$	0.009	10	>0.05	0.094	10	>0.05	0.414	10	**<0.05**	0.283	10	>0.05
$\Phi_{\mathrm{IV},n}$	0.057	10	>0.05	0.006	10	>0.05	0.052	10	>0.05	0.01	10	>0.05
$\Phi_{\mathrm{V},n}$	0.51	10	**<0.05**	0.462	10	**<0.05**	0.252	10	>0.05	0.345	10	>0.05
$\Phi_{\mathrm{T},n}$	0.416	10	**<0.05**	0.315	10	>0.05	0.106	10	>0.05	0.198	10	>0.05
$P_{\mathrm{I+II},n}$	0.608	10	**<0.05**	0.78	10	**<0.05**	0.914	10	**<0.05**	0.932	10	**<0.05**
$P_{\mathrm{III},n}$	0.098	10	>0.05	0.02	10	>0.05	0.034	10	>0.05	0.002	10	>0.05
$P_{\mathrm{IV},n}$	0.011	10	>0.05	0.083	10	>0.05	0.338	10	>0.05	0.221	10	>0.05
$P_{\mathrm{V},n}$	0.305	10	>0.05	0.192	10	>0.05	0.034	10	>0.05	0.109	10	>0.05

4.4 June Full Cycle Profile

A summary of the 2019-06-25 Cycle profile is provided below. Additional parameters are available in table 4.12 on page 55, these parameters have been provided by graduate student John Carter.

4.4.1 June Fluorescence Response and FRI Interpretation

The linear relationship between the nutrient removal rates and the FRI intensity volumes and percentage fluorescence response from each region has been assessed for the 2019-06-25 cycle profile. The recorded intensities from the anaerobic phase can be seen in table B.5 on page 72 together with the recorded PO_4-P values. Table 4.5 shows the calculated R^2 values between the FRI intensities and nutrient concentrations as well as percentage fluorescence response and nutrient concentrations.

As can be seen in table 4.5, only region $\Phi_{I+II,n}$ was observed to have a significant ($p<0.05$) linear relationship between the FRI intensity volume and the PO_4-P concentration. Again, a stronger relationship is observed between separate regions ($\Phi_{I+II,n}$) than between the total area ($\Phi_{T,n}$) and PO_4-P concentration. The same is observed for the percentage fluorescence response from region I+II where it is the only region with a significant ($p<0.05$) relationship with the PO_4-P concentration.

Table 4.5: Calculated R^2 of the linear relationship between FRI intensity volumes ($\Phi_{i,n}$), percentage fluorescence response ($P_{i,n}$) and nutrient concentrations for the 2019-06-25 anaerobic cycle profile

	PO_4-P (mg/L)	p-value	n
$\Phi_{I+II,n}$	0.509	**<0.05**	10
$\Phi_{III,n}$	0.116	>0.05	10
$\Phi_{IV,n}$	0.089	>0.05	10
$\Phi_{V,n}$	0.001	>0.05	10
$\Phi_{T,n}$	0.359	>0.05	10
$P_{I+II,n}$	0.631	**<0.05**	10
$P_{III,n}$	0.281	>0.05	10
$P_{IV,n}$	0.001	>0.05	10
$P_{V,n}$	0.283	>0.05	10

Recorded intensities and percentage fluorescence response for the aerobic phase can be

seen in table B.6 on page 72 together with the recorded nutrient values. For this cycle profile, as can be seen in table 4.6, region $\Phi_{\mathrm{I+II},n}$ is observed to have the strongest relationship with the inorganic nitrogen species, and region $\Phi_{\mathrm{IV},n}$ is observed to have the strongest relationship with the PO_4-P concentration. Region $\Phi_{\mathrm{V},n}$ was the only region that did not show any significant linear relationships between the nutrient concentrations. Even though the differences are small, the total area ($\Phi_{\mathrm{T},n}$) is observed to have a weaker relationship with nutrient concentrations than separate regions ($\Phi_{\mathrm{I+II},n}$ and $\Phi_{\mathrm{IV},n}$) of the 3D-EEMs. The percentage fluorescence response from all regions are observed to have a significant relationship with the nutrient concentrations.

Table 4.6: Calculated R^2 of the linear relationship between FRI intensity volumes ($\Phi_{i,n}$), percentage fluorescence response ($P_{i,n}$) and nutrient concentrations for the 2019-06-25 aerobic cycle profile

	PO_4-P (mg/L)	n	p-value	NH_3-N (mg/L)	n	p-value	NO_3-N (mg/L)	n	p-value	NO_2-N (mg/L)	n	p-value
$\Phi_{\mathrm{I+II},n}$	0.618	14	**<0.05**	0.713	14	**<0.05**	0.728	14	**<0.05**	0.867	14	**<0.05**
$\Phi_{\mathrm{III},n}$	0.598	14	**<0.05**	0.568	14	**<0.05**	0.676	14	**<0.05**	0.562	14	**<0.05**
$\Phi_{\mathrm{IV},n}$	0.62	14	**<0.05**	0.659	14	**<0.05**	0.706	14	**<0.05**	0.749	14	**<0.05**
$\Phi_{\mathrm{V},n}$	0.12	14	>0.05	0.133	14	>0.05	0.103	14	>0.05	0.104	14	>0.05
$\Phi_{\mathrm{T},n}$	0.613	14	**<0.05**	0.694	14	**<0.05**	0.712	14	**<0.05**	0.83	14	**<0.05**
$P_{\mathrm{I+II},n}$	0.582	14	**<0.05**	0.678	14	**<0.05**	0.694	14	**<0.05**	0.856	14	**<0.05**
$P_{\mathrm{III},n}$	0.685	14	**<0.05**	0.732	14	**<0.05**	0.783	14	**<0.05**	0.852	14	**<0.05**
$P_{\mathrm{IV},n}$	0.485	14	**<0.05**	0.448	14	**<0.05**	0.526	14	**<0.05**	0.465	14	**<0.05**
$P_{\mathrm{V},n}$	0.618	14	**<0.05**	0.69	14	**<0.05**	0.738	14	**<0.05**	0.878	14	**<0.05**

4.5 Mini-series

A summary of the mini-series collected from April trough May is provided in the following subsection.

4.5.1 Mini-series Fluorescence Response and FRI Interpretation

Recorded FRI intensity volumes and nutrient concentrations can be seen in table B.7 on page 73 for the anaerobic phase and B.8 on page 73 for the aerobic phase.

Table 4.7 on the following page shows the calculated R^2 values between the FRI intensities and PO_4-P concentrations and percentage fluorescence response from each region and PO_4-P concentrations. The recorded samples did not show any significant ($p>0.05$) linear relationship between any of the recorded fluorescence intensity areas. To establish whether this is due to seasonal variations or not would need further research.

Table 4.7: Calculated R^2 of the linear relationship between FRI intensity volumes ($\Phi_{i,n}$), percentage fluorescence response ($P_{i,n}$) and nutrient concentrations for the mini-series anaerobic samples

	PO_4-P (mg/L)	p-value	n
$\Phi_{\mathrm{I+II},n}$	0.146	>0.05	14
$\Phi_{\mathrm{III},n}$	0.014	>0.05	14
$\Phi_{\mathrm{IV},n}$	0.012	>0.05	14
$\Phi_{\mathrm{V},n}$	0.006	>0.05	14
$\Phi_{\mathrm{T},n}$	0.053	>0.05	14
$P_{\mathrm{I+II},n}$	0.197	>0.05	14
$P_{\mathrm{III},n}$	0.028	>0.05	14
$P_{\mathrm{IV},n}$	0.117	>0.05	14
$P_{\mathrm{V},n}$	0.149	>0.05	14

Data for the aerobic phase can be seen in table B.8 on page 73. The relationship between the FRI intensities and NH_3-N concentration has been assessed as well as the percentage fluorescence response and its relationship with NH_3-N concentration. All the FRI regions showed a significant ($p<0.05$) linear relationship with the recorded nutrient concentration. Region $\Phi_{\mathrm{I+II},n}$ was observed to have the strongest relationship and this region also had a stronger relationship than the sum of all the areas ($\Phi_{\mathrm{T},n}$). Interestingly, only the percentage fluorescence response from region IV showed a significant ($p<0.05$) relationship with NH_3-N concentration.

Table 4.8: Calculated R^2 of the linear relationship between FRI intensity volumes ($\Phi_{i,n}$), percentage fluorescence response ($P_{i,n}$) and nutrient concentrations for the mini-series aerobic samples

	NH_3-N (mg/L)	p-value	n
$\Phi_{\mathrm{I+II},n}$	0.502	**<0.05**	29
$\Phi_{\mathrm{III},n}$	0.366	**<0.05**	29
$\Phi_{\mathrm{IV},n}$	0.229	**<0.05**	29
$\Phi_{\mathrm{V},n}$	0.303	**<0.05**	29
$\Phi_{\mathrm{T},n}$	0.408	**<0.05**	29
$P_{\mathrm{I+II},n}$	0.131	>0.05	29
$P_{\mathrm{III},n}$	0.018	>0.05	29
$P_{\mathrm{IV},n}$	0.155	**<0.05**	29
$P_{\mathrm{V},n}$	0.03	>0.05	29

4.6 PARAFAC Data Interpretation

Prior to generating the PARAFAC model, the datasets from the full cycle profiles from both March, May and June were combined into two datasets, one from the anaerobic phase and the other from the aerobic phase. This resulted in two PARAFAC models, where the anaerobic PARAFAC model consists of 30 samples and the aerobic consists of 37 samples.

The core consistency diagnostic was used to determine the appropriate number of PARAFAC components, this diagnostic is available in appendix C on page 75. In essence, the core consistency should remain as close to 100 as possible. This resulted in the choice of a two-component model for both the anaerobic and the aerobic phase models. The inclusion of a third component results in the core consistency dropping below 100.

Stedmon and Bro (2008) recommend modeling datasets with 20–100 samples, but using datasets far above 100 samples would in general make the modeling simpler. With the use of 30 and 37 samples respectively, the 2 component models were not able to distinguish all the fluorophores into separate components, resulting in components with multiple peaks. The difficulty of distinguishing between components have also been reported by Murphy et al. (2011). In addition, it is not possible to determine the concentration of the analytes in the samples without knowing the concentration in one sample (Bro, 1997). Therefore, the extracted concentrations are referred to as relative concentrations.

Nevertheless, next are the extracted components from the anaerobic and aerobic phase and their relationship with nutrient concentration. The calculated scores for the components in both the anaerobic and aerobic PARAFAC model can be seen in table C.1 on page 76 and C.2 on page 77 respectively in appendix C on page 75.

4.6.1 Anaerobic PARAFAC Model Interpretation

The anaerobic PARAFAC model resulted in two components both comprising of 2 peaks each. Component 1 and 2 can be seen in figure 4.2 on the following page. A comparison of the anaerobic and aerobic model can be seen in table 4.9 on the next page.

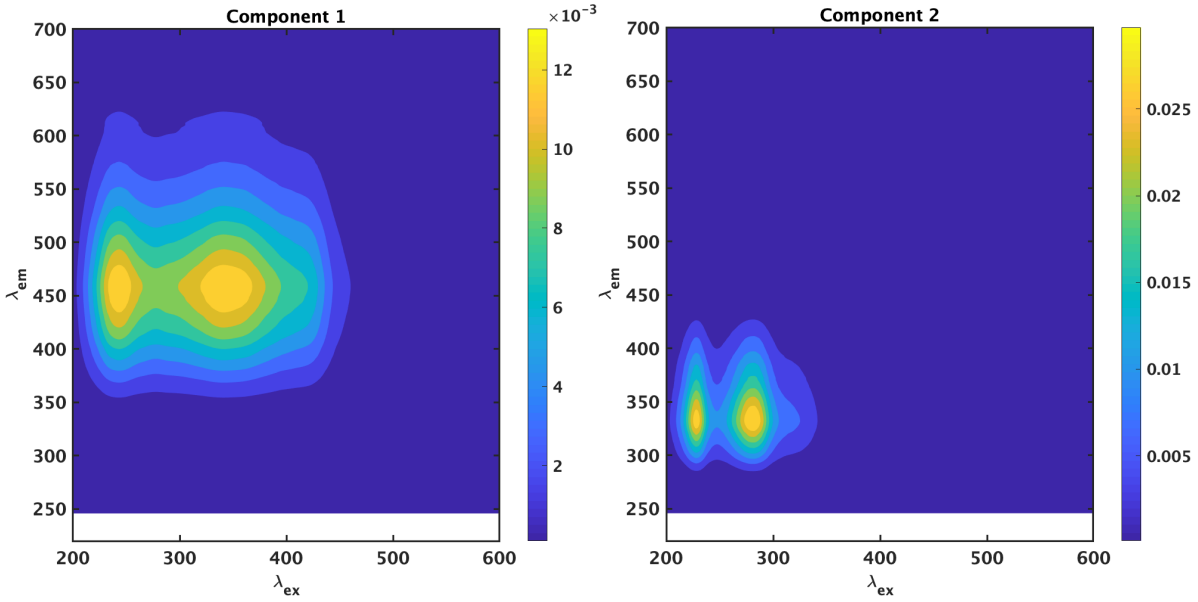

Figure 4.2: Anaerobic PARAFAC model components

Component 1 has its largest peak at around $\lambda_{ex}/\lambda_{em}$=350/460 nm and the second peak at $\lambda_{ex}/\lambda_{em}$=250/460 nm. On assessing these peaks with regions defined by Coble (1996) and Sgroi et al. (2017), it was found that component 1 in the PARAFAC analysis comprises of both humic-like and fulvic-like substances. Component 2 has its largest peaks at around $\lambda_{ex}/\lambda_{em}$=280/330 nm and $\lambda_{ex}/\lambda_{em}$=220/320 nm comprising both microbial byproducts, proteins, tryphtophan-like and biopolymers as well as aromatic proteins and tyrosine-like substances.

The linear relationship between the relative concentration of the PARAFAC components have been assessed, and the results are provided in table 4.10 on the facing page.

Table 4.9: PARAFAC components from the anaerobic and aerobic PARAFAC model

	Component designation	Excitation (nm)	Emission (nm)
Anaerobic	Component 1	250 & 350	460 & 460
Anaerobic	Component 2	220 & 280	320 & 330
Aerobic	Component 1	250 & 350	460 & 460
Aerobic	Component 2	220 & 280	320 & 330

Table 4.10: Calculated R^2 of the linear relationship between relative concentrations of PARAFAC components and measured nutrient concentrations in the anaerobic phase

	PO_4-P (mg/L)	p-value	n
C1	0.019	>0.05	30
C2	0.061	>0.05	30
C1 - June excluded	0.615	**<0.05**	20
C2 - June excluded	0.038	>0.05	20

No significant correlations were found between component 1 and component 2 relative concentrations and the PO_4-P concentrations when looking at the model as a whole. Interestingly enough, the June relative concentration varied widely from the observed relative concentrations in both March and May. No significant linear relationship was observed between component 2 without the June samples and PO_4-P concentrations, but a linear relationship ($p<0.05$) was observed between component 1 relative concentration and PO_4-P concentration when excluding the June component 1 relative concentrations as can be seen in table 4.10 and figure 4.3.

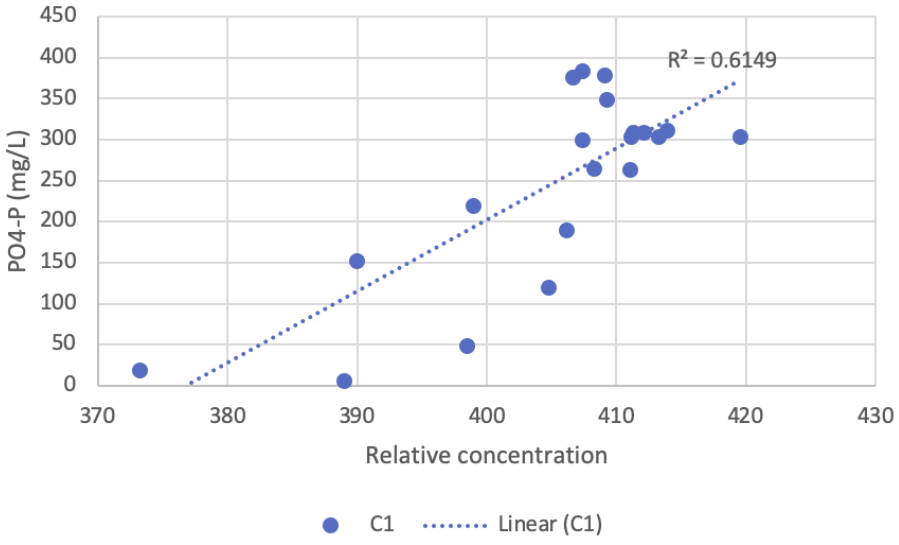

Figure 4.3: Relationship in the anaerobic phase between component 1 relative concentration and PO_4-P concentration after exclusion of June component 1 data

4.6.2 Aerobic PARAFAC Model Interpretation

The PARAFAC model for the aerobic samples shows similar characteristics as the PARAFAC model for the anaerobic samples. The components can be seen in fig-

ure 4.4. The components show similar traits with component 1 having its largest peaks at $\lambda_{ex}/\lambda_{em}$=350/460 nm and the second peak at $\lambda_{ex}/\lambda_{em}$=250/460 nm. Component 2 has its largest peaks at around $\lambda_{ex}/\lambda_{em}$=280/330 nm and $\lambda_{ex}/\lambda_{em}$=220/320 nm. Notably, component 2 has a more prominent peak around $\lambda_{ex}/\lambda_{em}$=220/320 nm in the anaerobic PARAFAC component than what has been observed in the aerobic PARAFAC model component 2.

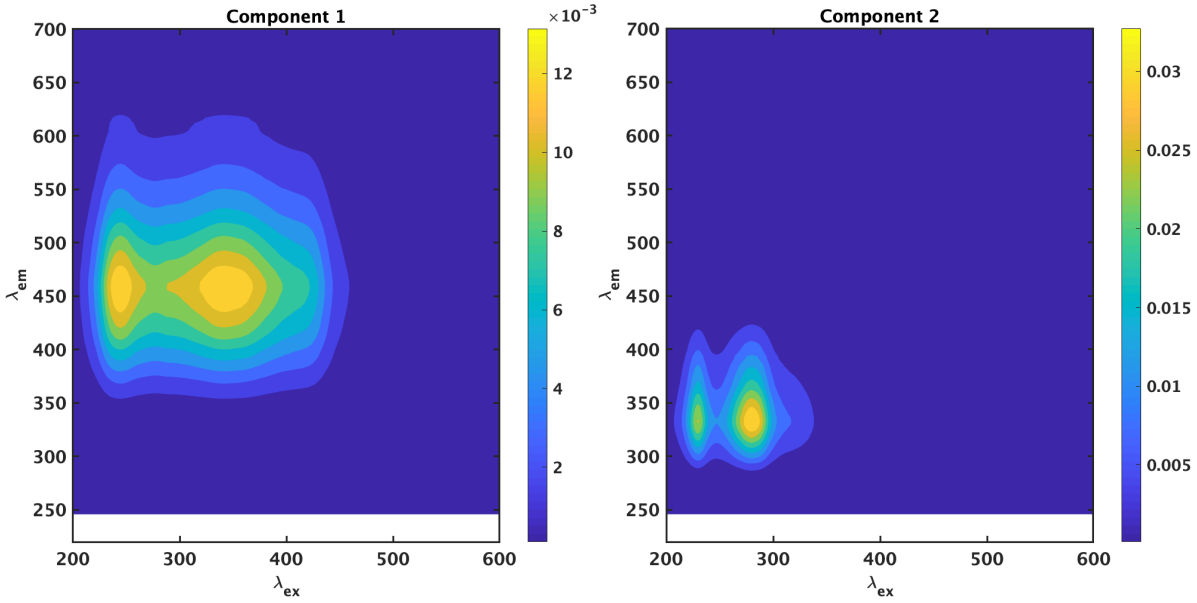

Figure 4.4: Aerobic PARAFAC model components

The linear relationship between the aerobic PARAFAC components and nutrient concentrations can be seen in table 4.11. It can be inferred that the relative concentration of component 2 shows a weak but significant ($p<0.05$) relationship between NO_3-N and NO_2-N. No relationship was observed between component 2 relative concentration and PO_4-P and NH_3-N concentration.

Table 4.11: Calculated R^2 of the linear relationship between relative concentrations of PARAFAC components and measured nutrient concentrations in the aerobic phase

	PO_4-P (mg/L)	p-value	n	NH_3-N (mg/L)	p-value	n	NO_3-N (mg/L)	p-value	n	NO_2-N (mg/L)	p-value	n
C1	0.193	**<0.05**	32	0.900	**<0.05**	37	0.189	**<0.05**	37	0.379	**<0.05**	37
C2	0.029	>0.05	32	0.053	>0.05	37	0.388	**<0.05**	37	0.306	**<0.05**	37
C1 - June excluded	0.162	>0.05	18	0.342	**<0.05**	23	0.014	>0.05	23	0.000	>0.05	23
C2 - June excluded	0.005	>0.05	18	0.003	>0.05	23	0.373	**<0.05**	23	0.292	**<0.05**	23

As observed with the anerobic PARAFAC model, the relative concentration from the June sample deviates widely from the observed relative concentrations in both March and May. A strong relationship between component 1 relative concentration and NH_3-N

is observed, as well as a significant ($p<0.05$), but weak, relationship between NO_3-N and NO_2-N. After the exclusion of the June samples, as can be seen in figure 4.5, a weak but significant relationship ($p<0.05$) is still observed between component 1 relative concentration and NH_3-N concentration. After the exclusion of the June samples, no significant relationship is observed with the relative concentration of component 1 and NO_3-N and NO_2-N concentration. However, component 2 relative concentration is still showing a significant relationship with NO_3-N and NO_2-N concentration even after the exclusion of the June samples.

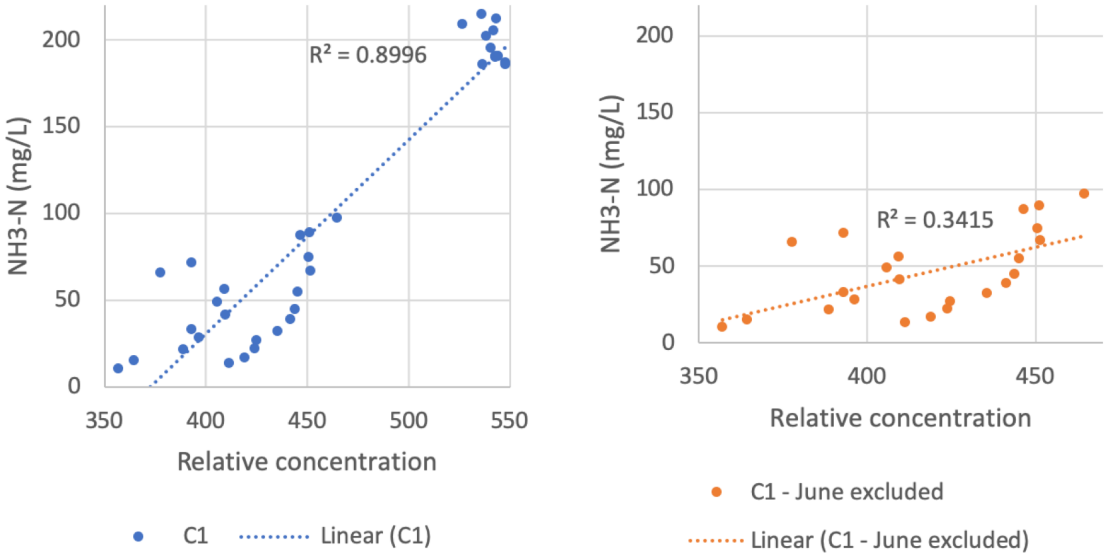

Figure 4.5: Relationship in the aerobic phase between C1 relative concentration and NH_3-N concentration (left) and C1 relative concentration and NH_3-N concentration after exclusion of June data (right)

4.7 March, May and June Cycle Profiles

As noted in subsection 4.3.1 on page 40 and 4.4.1 on page 42 the separate fluorescence regions ($\Phi_{I+II,n}$, $\Phi_{III,n}$, $\Phi_{IV,n}$, $\Phi_{V,n}$) shows a stronger relationship separately than the total fluorescence area ($\Phi_{T,n}$) in the anaerobic phase. Only region $\Phi_{I+II,n}$ shows a significant relationship with PO_4-P. Out of all three anaerobic cycle profiles, the region with the strongest linear relationship between FRI intensity volume and PO_4-P concentration is varying from $\Phi_{T,n}$, $\Phi_{III,n}$ and $\Phi_{I+II,n}$ for March, May and June respectively.

For illustration, the relationship between the FRI intensity volume in region $\Phi_{I+II,n}$ and PO_4-P concentration for the anaerobic phase for all full cycle profiles is plotted in figure 4.6 on the following page. This is the only region that was observed to have a significant relationship ($p<0.05$) between the fluorescence intensities and PO_4-P concen-

tration. As illustrated, the relationship between the FRI intensity volume and PO_4-P concentration varies widely. The March full cycle is even observed to have a strong exponential relationship between region $\Phi_{I+II,n}$ and PO_4-P, however, this relationship is not observed in the May and June profile.

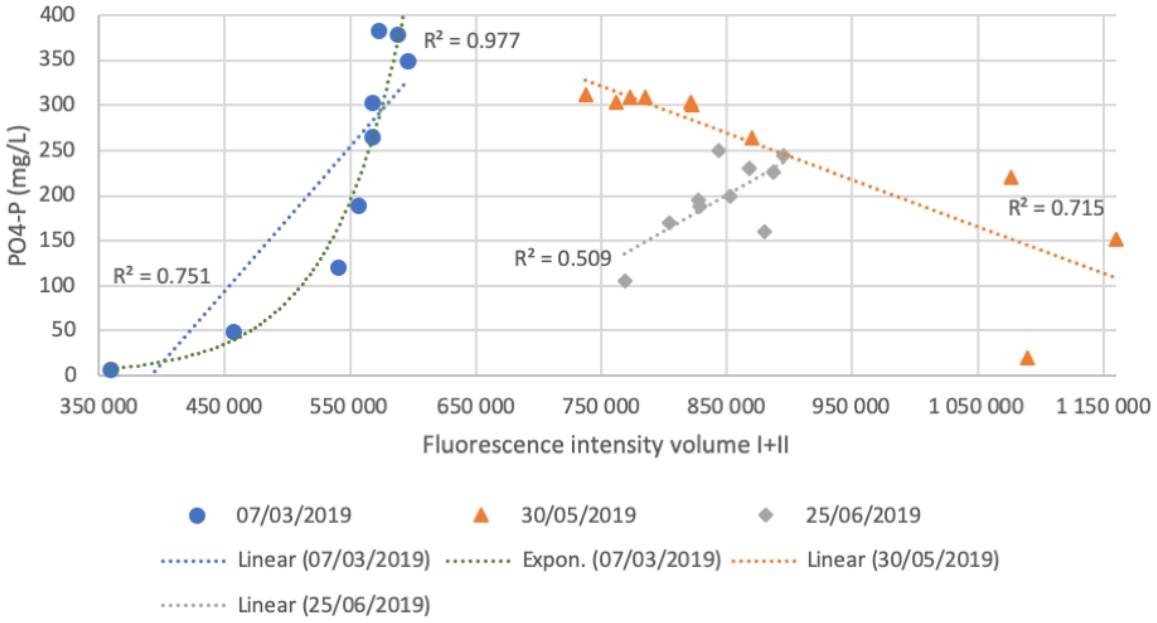

Figure 4.6: Relationship between PO_4-P and the recorded FRI intensity volumes for region $\Phi_{I+II,n}$ in the anaerobic phase

Great variations in the aerobic phase are also observed. Only region $\Phi_{I+II,n}$ shows a significant relationship with all the measured nutrient parameters out of all the regions for both the March, May and June cycle profile.

In the aerobic phase, the relationship is observed to be more consistent compared to the anaerobic phase. The relationship between the FRI intensity volume in region $\Phi_{I+II,n}$ and recorded nutrient concentrations can be seen in figure 4.7 on the next page.

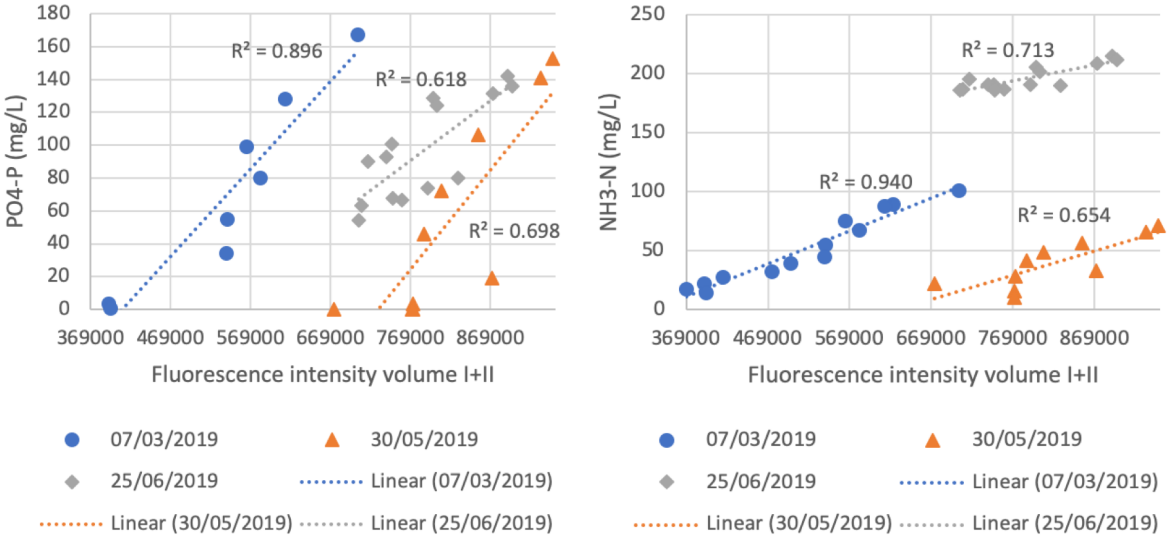

Figure 4.7: Relationship between PO4-P, NH_3-N and the recorded FRI intensity volumes for region $\Phi_{I+II,n}$ in the aerobic phase

The percentage fluorescence response and its relationship with the nutrient concentrations are also observed to vary and not be consistent with the FRI regions. Nevertheless, the percentage response from region I+II is the only region with a significant ($p<0.05$) relationship with all the nutrient parameters for both the March, May and June cycles. This relationship can be seen in figure 4.8 and 4.9 on the next page.

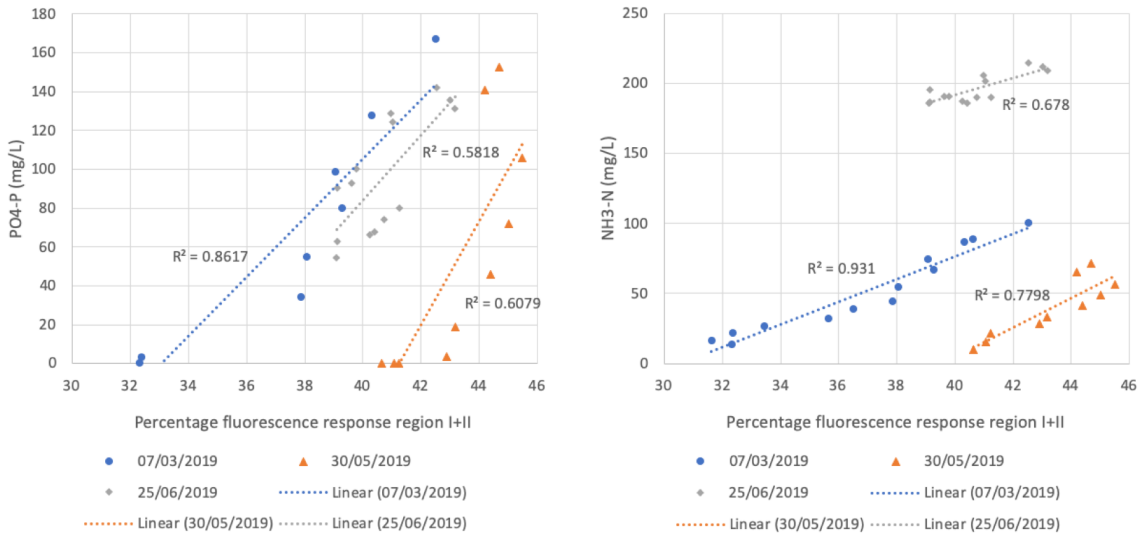

Figure 4.8: Relationship between PO_4-P, NH_3-N and the recorded percentage fluorescence response in the aerobic phase for region I+II

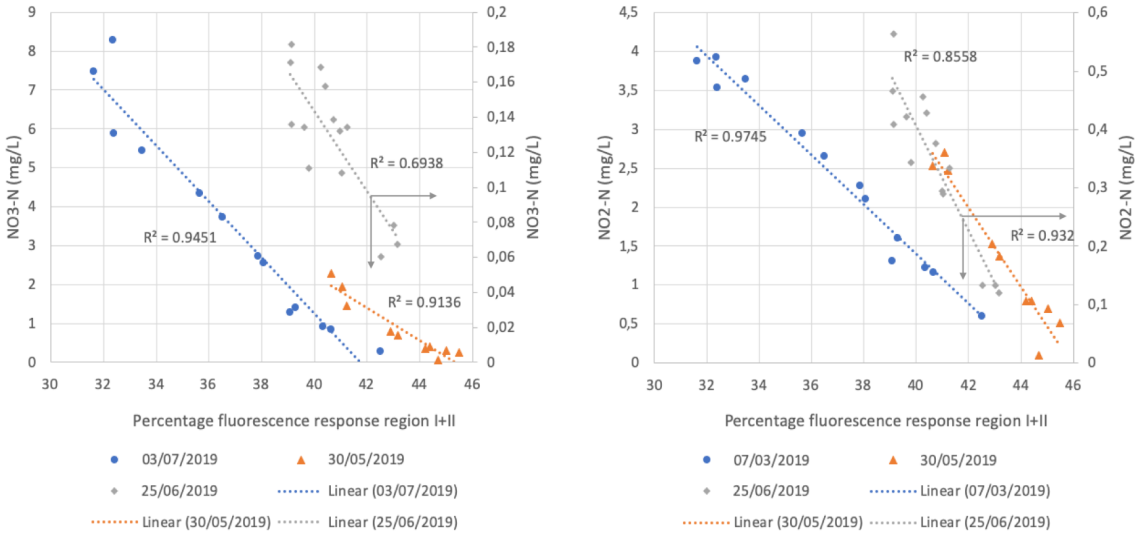

Figure 4.9: Relationship between NO_3-N, NO_2-N and the recorded percentage fluorescence response in the aerobic phase for region I+II. (Please note that the June cycle profile is plotted on the secondary axis)

Both PO_4-P and NH_3-N concentrations are observed to correlate positively with the recorded FRI intensity volume in region $\Phi_{I+II,n}$. On the other hand, the opposite is observed for NO_3-N and NO_2-N concentrations, see figure 4.10.

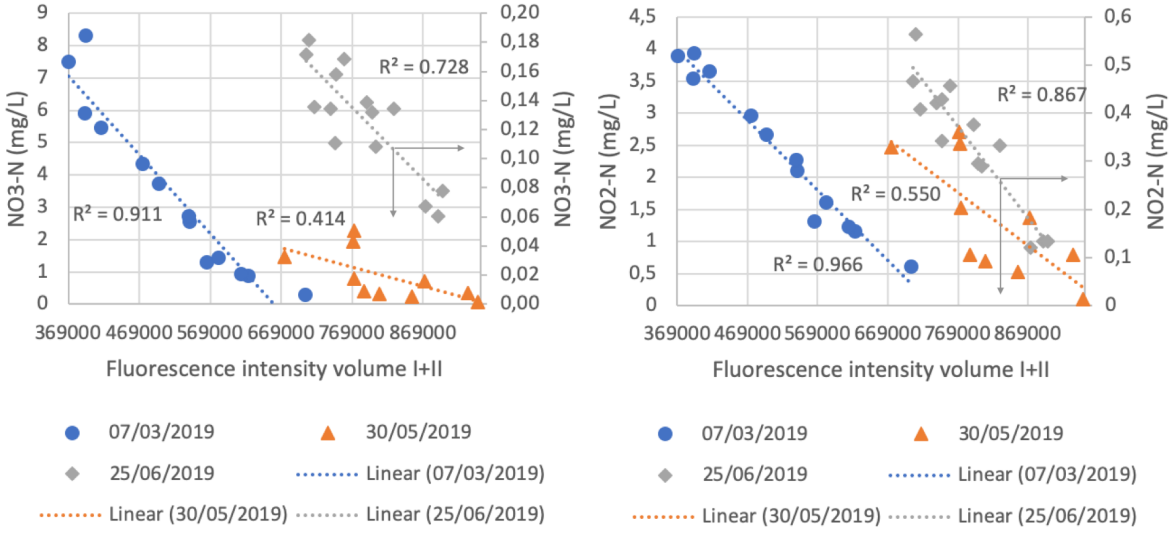

Figure 4.10: Relationship between NO_3-N, NO_2-N and the recorded FRI intensity volumes for region $\Phi_{I+II,n}$ in the aerobic phase. (Please note that the June cycle profile is plotted on the secondary axis)

Once again, great variations between the different sampling series are observed. The underlying cause is not yet understood in great detail. It might be due to both seasonal variations and changes in the influent quality and composition. In addition, differences in the EPS composition in the reactor during the aerobic and anaerobic phases might also

be a contributing factor, as changes in the EPS content and composition are observed to occur during reactor cycles in granular sludge reactors (Rusanowska et al., 2019).

For the potential monitoring of the anaerobic phase, region $\Phi_{IV,n}$ attributed to microbial byproducts, proteins, tryphtophan-like substances and biopolymers (Sgroi et al., 2017) showed significant correlation in both March and May profiles. Even though region $\Phi_{III,n}$ showed a stronger relationship in the 2019-05-30 cycle profile, its relationship in the 2019-03-07 profile was the lowest of all regions. Nevertheless, region $\Phi_{I+II,n}$ attributed to aromatic proteins, tyrosine- and tryphtophan-like substances (Sgroi et al., 2017) showed significant correlations for all full cycle profiles. No other regions showed any significant correlations in the anaerobic phase for the June full cycle profile. Therefore, region $\Phi_{I+II,n}$ is observed to have the most interesting properties for the potential of online monitoring.

In the aerobic phase, region $\Phi_{I+II,n}$ shows the most promising excitation/emission wavelengths to choose for monitoring, whereas region $\Phi_{IV,n}$, which was observed to have a strong relationship in the anaerobic phase showed weak correlations in the aerobic phase.

These observed results, even though low in the number of samples, showed that if fluorescent probes for on-line monitoring are to be installed, probes with excitation/emission wavelengths in region I+II would be a good starting point in the anaerobic phase, whereas probes with excitation/emission wavelengths in region I+II would be a good starting point in the aerobic phase. It should be noted that probes in the I+II region will most likely be impacted by IFEs and therefore, additional assessment of IFE should be considered.

Major differences in the percent fluorescence response throughout the cycle in both the anaerobic phase and the aerobic phase are observed.

In the anaerobic phase (see figure 4.11 on the next page), region $\Phi_{I+II,n}$ is observed to contribute to a lower percentage of the total fluorescence response in the March and June cycle profiles compared to the May cycle. The opposite is observed for region $\Phi_{III,n}$ except during the last 10 minutes of the anaerobic phase. The May cycle profile is also observed to have the most percentage fluorescence response variation in region $\Phi_{III,n}$. In addition, the greatest changes is the percentage of the fluorescent response seems to happen around the first 25–30 minutes of the anaerobic phase.

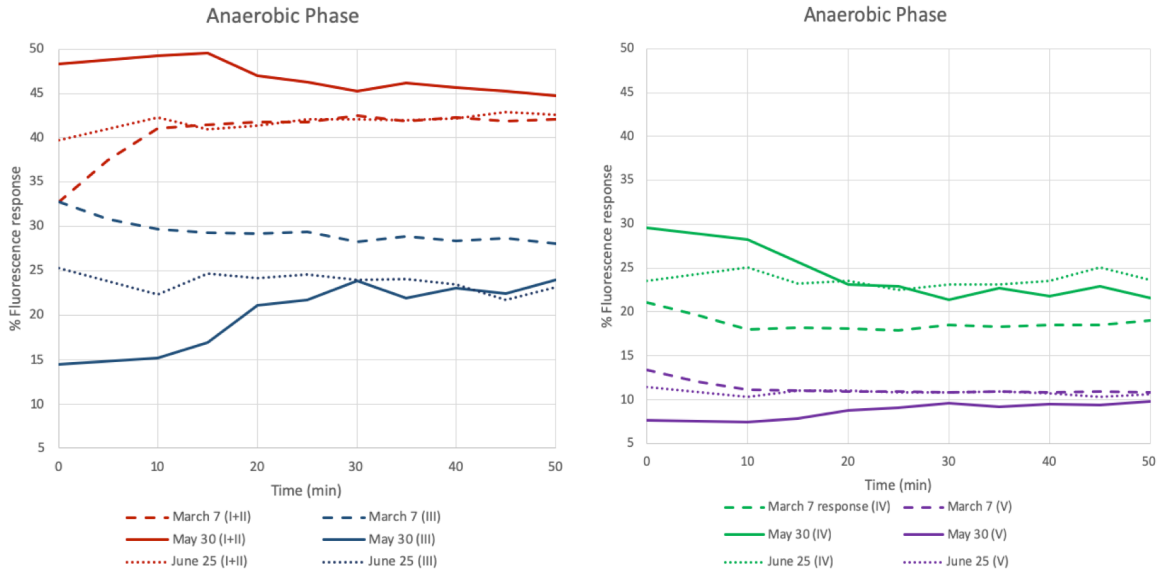

Figure 4.11: Comparison of percentage fluorescent response in the anaerobic phase

For the aerobic phase (see figure 4.12), region $\Phi_{\mathrm{I+II},n}$ shows a decreasing trend for all three cycle profiles whereas region $\Phi_{\mathrm{III},n}$ and $\Phi_{\mathrm{V},n}$ shows an increasing trend. Region $\Phi_{\mathrm{IV},n}$ is also observed to have an increasing trend for the May and March profile, and a decreasing trend for the June profile. The May profile is also observed to vary widely in region $\Phi_{\mathrm{III},n}$ and $\Phi_{\mathrm{IV},n}$.

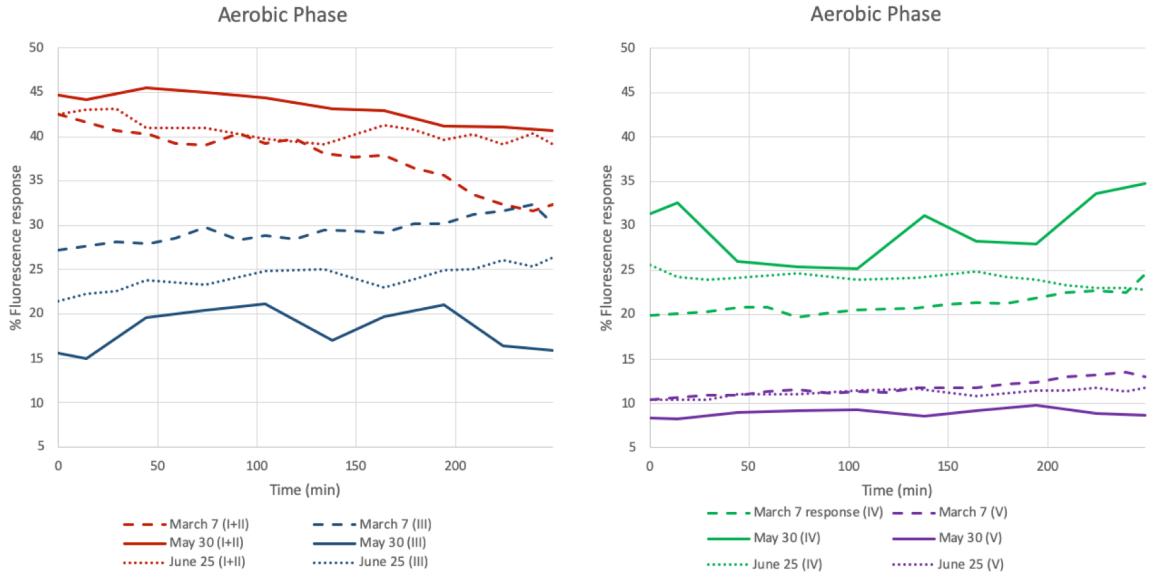

Figure 4.12: Comparison of percentage fluorescent response in the aerobic phase

The underlying cause of the observed differences between the cycle profiles is not understood in great detail, and might be attributed to seasonal variations or even the

differences in the performance of the reactor itself. As shown in table 4.12, there are great differences in activity and performance of the reactor between the three full cycle series.

Table 4.12: Selected operational parameters from the full cycle profiles

Parameter	**Units**	**Value**	**Value**	**Value**
Cycle profile		March	May	June
Sidestream Reactor				
Operating Height	ft	8	8	8
Diameter	in	12	12	12
Full Volume	L	176	176	176
Volume Exchange Ratio	–	0.5	0.45	
MLSS	mg/L	12 080	12142	9189
VSS/TSS	–	0.7	0.72	0.85
Activity and Performance				
Initial Equivalent Ammonia	mgN/L	113.7	82	224.5
Ammonia Removed by Synthesis	mgN/L	10.5	6.6	9.4
Ammoina Oxidized	mgN/L	89.4	68.9	42.4
N removed by SND	mgN/L	76.2	60.3	41.8
P removed	g/cycle	2.5	2.6	-2
Removal Rates				
Ammonia Removal Rate	mg/L/min	0.354	0.2577	0.1534
Specific Ammonia Removal Rate	mgN/gVSS/hr	2.52	1.76	1.18
Initial Specific P-uptake Rate	mgP/gVSS/hr	2.92	6.8115	
Anaerobic Phase Influent				
Acetate Feed Tank Concentration	gCOD/L	78	85	
Acetate Feed Volume	L	0.99	0.73	
Aerobic Phase Influent				
Centrate Feed Tank Ammonia	mgN/L	775.3	719.235	977.15
Centrate Feed Tank Ortho-P	mgP/L	107.4	147.86	122.97
Centrate Feed Tank Acetate	mgCOD/L	3.8		
Centrate Feed Tank TSS	mg/L	64		
Centrate Feed Tank Volume	L	22.8	16.77	
Dilution Feed Tank Ammonia	mgN/L	32.7	30.413	32.59
Dilution Feed Tank Orth-P	mgP/L	2.4	3.041	3.05
Dilution Feed Tank TSS	mg/L	10		
Dilution Feed Tank Volume	L	62.4	62.4	
Effluent				
Effluent Ammonia	mgN/L	13.8	86.5	172.68
Effluent Nitrite	mgN/L	4.1	0.6	0.438
Effluent Nitrate	mgN/L	9.1	0.3	0.151
Effluent Ortho-P	mgP/L	1.5	39.2	57.25
Effluent TSS	mg/L	83	85	142
Data provided by		Maxwell Armenta	Maxwell Armenta	John Carter

With the implementation of fluorescent monitoring equipment, greater understanding of the observed behaviour is possible, and even early detection of abnormalities might

be possible.

5. Conclusions

To date, few studies have been carried out to monitor the behaviour of the 3D-EEMs, which has a potential for online process monitoring, during both anaerobic and aerobic phases in a sidestream granular sludge reactor.

This study successfully presented and examined the observed changes in the 3D-EEMs in both of these phases of the reactor. Four distinct fluorescent regions in the 3D-EEMs were selected for quantification. In addition, the changes in the percentage fluorescence response from each region were monitored for both the anaerobic and aerobic phase of the reactor.

Information from the complete 3D-EEMs were processed through regional integration and the percentage fluorescence response from each region was also evaluated. The linear relationship between this data and the recorded nutrient concentrations was then assessed. Great variations between each of the regions relationship with the measured nutrient concentration were observed. For the full-cycle profiles, only region $\Phi_{I+II,n}$, attributed to aromatic proteins with both tyrosine-like and tryphtophan-like substances (Sgroi et al., 2017), was observed to have a significant linear relationship ($p<0.05$) with PO_4-P in the anaerobic phase. The mini-series did not show any significant relationship between PO_4-P and the recorded fluorescence intensity areas.

In the aerobic phase, region $\Phi_{I+II,n}$ was also the only region in the full cycle profiles observed to have a significant relationship with the nutrient concentrations throughout the whole sampling period. In addition, distinct fluorescent regions in the 3D-EEMs were observed to have a stronger relationship with the nutrient concentration compared to the total recorded fluorescence spectra. These regions differed and some times included multiple regions, but region $\Phi_{I+II,n}$ was observed to have a stronger linear relationship than the total fluorescence spectra on all the full cycle series of the reactor during the aerobic phase.

Two PARAFAC models were generated from the full cycle profiles from March, May and June. Both of these models resulted in a 2-component model. These models were not able to completely separate the fluorophores present in the solution resulting in

PARAFAC components consisting of more than one peak. Nevertheless, the extracted components relationship with nutrient concentrations were assessed and no significant relationship between the components were observed for the anaerobic PARAFAC-model. The June cycle profile was observed to have very varying relative concentrations and a weak, but significant ($p<0.05$), linear relationship were observed between component 1 and PO_4-P after the exclusion of the June samples.

In the aerobic PARAFAC-model, relative concentrations from the June cycle profile were also observed to be greatly different than the March and May samples. No significant relationship was observed between component 1 and PO_4-P after the exclusion of the June samples, but component 1 and NH_3-N concentration as well as component 2 and NO_3-N and NO_2-N showed a significant linear relationship ($p<0.05$) after the exclusion of the June samples.

The linear relationships between the 3D-EEMs and nutrient concentrations have been observed to vary widely. The use of fluorescence based monitoring as a potential tool for online quantitation of the nutrient removal in wastewater treatment is far from its potential. Further researchis needed to establish the full extent and significance of relationships between the fluorescent properties of wastewater and nutrient removal efficacy.

5.1 Recommendations for further research

The great deviations in the observed results necessitates monitoring of the fluorescent properties of the sidestream granular sludge reactor, especially in region $\Phi_{\mathrm{I+II},n}$. This can be done through the use of a fluorescent probe in addition to a bench-top spectrofluorometer for an extended sampling period. Both instruments will cover differences between reactor performance on a small time-scale (days and weeks) as well as differences between reactor performance varying with seasons (months).

Multiple data sets covering the full reactor cycle would enable the application of a wide range of statistical methods requiring large data sets for training and validation, and could then provide additional useful insights to the reactor performance.

References

Ahluwalia, S. S. and Goyal, D. (2007). Microbial and plant derived biomass for removal of heavy metals from wastewater. *Bioresource Technology* 98 (12): 2243–2257. DOI: 10.1016/J.BIORTECH.2005.12.006.

Bourgeois, W., Burgess, J. E., and Stuetz, R. M. (2001). *On-line monitoring of wastewater quality: A review*. DOI: 10.1002/jctb.393.

Bro, R. (1997). PARAFAC. Tutorial and applications. *Chemometrics and Intelligent Laboratory Systems* 38 (2): 149–171. DOI: 10.1016/S0169-7439(97)00032-4.

Carstea, E. M. (2012). Fluorescence Spectroscopy as a Potential Tool for In-Situ Monitoring of Dissolved Organic Matter in Surface Water Systems. In: *Water Pollution*. Ed. by N. Balkis. Rijeka: IntechOpen. Chap. 3. DOI: 10.5772/28979.

Carstea, E. M., Bridgeman, J., Baker, A., and Reynolds, D. M. (2016). Fluorescence spectroscopy for wastewater monitoring: A review. *Water Research* 95: 205–219. DOI: 10.1016/J.WATRES.2016.03.021.

Carstea, E. M., Zakharova, Y. S., and Bridgeman, J. (2018). Online Fluorescence Monitoring of Effluent Organic Matter in Wastewater Treatment Plants. *Journal of Environmental Engineering*. DOI: 10.1061/(asce)ee.1943-7870.0001360.

Chen, W., Westerhoff, P., Leenheer, J. A., and Booksh, K. (2003). Fluorescence Excitation-Emission Matrix Regional Integration to Quantify Spectra for Dissolved Organic Matter. *Environmental Science and Technology* 37 (24): 5701–5710. DOI: 10.1021/es034354c.

Coble, P. G. (1996). Characterization of marine and terrestrial DOM in seawater using excitation-emission matrix spectroscopy. *Marine Chemistry* 51 (4): 325–346. DOI: 10.1016/0304-4203(95)00062-3.

Cohen, E., Levy, G. J., and Borisover, M. (2014). Fluorescent components of organic matter in wastewater: Efficacy and selectivity of the water treatment. *Water Research* 55: 323–334. DOI: 10.1016/J.WATRES.2014.02.040.

Conley, D. J., Paerl, H. W., Howarth, R. W., Boesch, D. F., Seitzinger, S. P., Havens, K. E., Lancelot, C., and Likens, G. E. (2009). *Ecology - Controlling eutrophication: Nitrogen and phosphorus*. DOI: 10.1126/science.1167755.

Al-Dasoqi, N., Mason, A., Alkhaddar, R., and Al-Shamma'a, A. (2011). Use of Sensors in Wastewater Quality Monitoring—A Review of Available Technologies. In: DOI: 10.1061/41173(414)354.

De Kreuk, M. K., Van Loosdrecht, M. C. M., and Heijnen, J. J. (2006). *Aerobic granular sludge : scaling up a new technology*.

Figdore, B. A. (2017). Nitrification bioaugmentation in mainstream flocculent activated sludge systems using sidestream aerobic granular sludge. PhD thesis. Seattle.

Figdore, B. A., Stensel, H. D., Winkler, M. K., Armenta, M., Bucher, B., Sukapanpotharam, P., and Smyth, J. (2018a). Aerobic Granular Sludge Bioaugmentation in Low-SRT Flocculent Activated Sludge: Bench-Scale Demonstration and Pilot Testing. *Proceedings of the Water Environment Federation*. DOI: 10.2175/193864718825136071.

Figdore, B. A., David Stensel, H., and Winkler, M.-K. H. (2018b). Bioaugmentation of sidestream nitrifying-denitrifying phosphorus-accumulating granules in a low-SRT activated sludge system at low temperature. *Water Research* 135: 241–250. DOI: 10.1016/J.WATRES.2018.02.035.

Galinha, C. F., Carvalho, G., Portugal, C. A., Guglielmi, G., Oliveira, R., Crespo, J. G., and Reis, M. A. (2011). Real-time monitoring of membrane bioreactors with 2D-fluorescence data and statistically based models. *Water Science and Technology*. DOI: 10.2166/wst.2011.195.

Galinha, C. F., Carvalho, G., Portugal, C. A., Guglielmi, G., Reis, M. A., and Crespo, J. G. (2012). Multivariate statistically-based modelling of a membrane bioreactor for wastewater treatment using 2D fluorescence monitoring data. *Water Research* 46 (11): 3623–3636. DOI: 10.1016/J.WATRES.2012.04.010.

Giesen, A., de Bruin, L. M., Niermans, R. P., and van der Roest, H. F. (2013). Advancements in the application of aerobic granular biomass technology for sustainable treatment of wastewater. *Water Practice and Technology*. DOI: 10.2166/wpt.2013.007.

Haimi, H., Mulas, M., Corona, F., and Vahala, R. (2013). Data-derived soft-sensors for biological wastewater treatment plants: An overview. *Environmental Modelling & Software* 47: 88–107. DOI: 10.1016/J.ENVSOFT.2013.05.009.

Henderson, R., Baker, A., Murphy, K., Hambly, A., Stuetz, R., and Khan, S. (2009). Fluorescence as a potential monitoring tool for recycled water systems: A review. *Water Research* 43 (4): 863–881. DOI: 10.1016/J.WATRES.2008.11.027.

Hudson, N., Baker, A., and Reynolds, D. (2007). *Fluorescence analysis of dissolved organic matter in natural, waste and polluted waters - A review*. DOI: 10.1002/rra.1005.

Korshin, G. V., Sgroi, M., and Ratnaweera, H. (2018). Spectroscopic surrogates for real time monitoring of water quality in wastewater treatment and water reuse. *Current Opinion in Environmental Science & Health* 2: 12–19. DOI: 10.1016/J.COESH.2017.11.003.

Kothawala, D. N., Murphy, K. R., Stedmon, C. A., Weyhenmeyer, G. A., and Tranvik, L. J. (2013). Inner filter correction of dissolved organic matter fluorescence. *Limnology and Oceanography: Methods*. DOI: 10.4319/lom.2013.11.616.

Lakowicz, J. R. (2006). *Principles of fluorescence spectroscopy*. 3rd ed. New York: New York : Springer.

Li, J., Ni, Y., Peng, Y., Gu, G., Lu, J., Wei, S., Cheng, G., and Ou, C. (2008a). On-line controlling system for nitrogen and phosphorus removal of municipal wastewater in a sequencing batch reactor (SBR). *Frontiers of Environmental Science & Engineering in China* 2 (1): 99–102. DOI: 10.1007/s11783-008-0017-9.

Li, W.-H., Sheng, G.-P., Liu, X.-W., and Yu, H.-Q. (2008b). Characterizing the extracellular and intracellular fluorescent products of activated sludge in a sequencing batch reactor. *Water Research* 42 (12): 3173–3181. DOI: 10.1016/J.WATRES.2008.03.010.

Liu, H., Xiao, H., Huang, S., Ma, H., and Liu, H. (2014). Aerobic granules cultivated and operated in continuous-flow bioreactor under particle-size selective pressure. *Journal of Environmental Sciences* 26 (11): 2215–2221. DOI: 10.1016/J.JES.2014.09.004.

Maqbool, T., Quang, V. L., Cho, J., and Hur, J. (2016). Characterizing fluorescent dissolved organic matter in a membrane bioreactor via excitation-emission matrix combined with parallel factor analysis. *Bioresource Technology*. DOI: 10.1016/j.biortech.2016.02.089.

Mesquita, D. P., Quintelas, C., Amaral, A. L., and Ferreira, E. C. (2017). *Monitoring biological wastewater treatment processes: recent advances in spectroscopy applications*. DOI: 10.1007/s11157-017-9439-9.

Murphy, K. R., Hambly, A., Singh, S., Henderson, R. K., Baker, A., Stuetz, R., and Khan, S. J. (2011). Organic matter fluorescence in municipal water recycling schemes: Toward a unified PARAFAC model. *Environmental Science and Technology*. DOI: 10.1021/es103015e.

Oglesby, R. T. and Edmondson, W. T. (1966). Control of Eutrophication. *Journal (Water Pollution Control Federation)* 38 (9): 1452–1460. URL: http://www.jstor.org/stable/25035632.

Ohno, T. (2002). Fluorescence Inner-Filtering Correction for Determining the Humification Index of Dissolved Organic Matter. *Environmental Science & Technology* 36 (4): 742–746. DOI: 10.1021/es0155276.

Patel-Sorrentino, N., Mounier, S., and Benaim, J. (2002). Excitation–emission fluorescence matrix to study pH influence on organic matter fluorescence in the Amazon basin rivers. *Water Research* 36 (10): 2571–2581. DOI: 10.1016/S0043-1354(01)00469-9.

Pons, M.-N., Bonté, S. L., and Potier, O. (2004). Spectral analysis and fingerprinting for biomedia characterisation. *Journal of Biotechnology* 113 (1-3): 211–230. DOI: 10.1016/J.JBIOTEC.2004.03.028.

Pronk, M., Giesen, A., Thompson, A., Robertson, S., and Van Loosdrecht, M. (2017). Aerobic granular biomass technology: Advancements in design, applications and further developments. *Water Practice and Technology*. DOI: 10.2166/wpt.2017.101.

Reynolds, D. and Ahmad, S. (1995). The effect of metal ions on the fluorescence of sewage wastewater. *Water Research* 29 (9): 2214–2216. DOI: 10.1016/0043-1354(95)00046-N.

Riopel, R., Caron, F., and Siemann, S. (2014). Fluorescence Characterization of Natural Organic Matter at a Northern Ontario Wastewater Treatment Plant. *Water, Air, and Soil Pollution*. DOI: 10.1007/s11270-014-2126-3.

Rusanowska, P., Cydzik-Kwiatkowska, A., Światczak, P., and Wojnowska-Baryła, I. (2019). Changes in extracellular polymeric substances (EPS) content and composition in aerobic granule size-fractions during reactor cycles at different organic loads. *Bioresource Technology* 272: 188–193. DOI: 10.1016/j.biortech.2018.10.022.

Seredyńska-Sobecka, B., Baker, A., and Lead, J. R. (2007). Characterisation of colloidal and particulate organic carbon in freshwaters by thermal fluorescence quenching. *Water Research* 41 (14): 3069–3076. DOI: 10.1016/J.WATRES.2007.04.017.

Sgroi, M., Roccaro, P., Korshin, G. V., Greco, V., Sciuto, S., Anumol, T., Snyder, S. A., and Vagliasindi, F. G. (2017). Use of fluorescence EEM to monitor the removal of emerging contaminants in full scale wastewater treatment plants. *Journal of Hazardous Materials* 323: 367–376. DOI: 10.1016/J.JHAZMAT.2016.05.035.

Stedmon, C. A. and Bro, R. (2008). Characterizing dissolved organic matter fluorescence with parallel factor analysis: A tutorial. *Limnology and Oceanography: Methods*. DOI: 10.4319/lom.2008.6.572.

Tchobanoglous, G., Abu-Orf, M., Bowden, G., Pfrang, W., Eddy, M., and AECOM (2014). *Wastewater engineering: treatment and resource recovery*. 5th ed. New York: McGraw-Hill Education.

Tsuneda, S., Nagano, T., Hoshino, T., Ejiri, Y., Noda, N., and Hirata, A. (2003). Characterization of nitrifying granules produced in an aerobic upflow fluidized bed reactor. *Water Research* 37 (20): 4965–4973. DOI: 10.1016/J.WATRES.2003.08.017.

Valeur, B. (2001). *Molecular Fluorescence: Principles and Applications, Publisher Wiley.*

Vassos, T. (1993). Future Directions in Instrumentation, Control and Automation in the Water and Wastewater Industry. *Water Science and Technology* 28: 9–14. DOI: 10.2166/wst.1993.0640.

Vodacek, A. and Philpot, W. D. (1987). Environmental effects on laser-induced fluorescence spectra of natural waters. *Remote Sensing of Environment* 21 (1): 83–95. DOI: 10.1016/0034-4257(87)90008-3.

Wang, X., Kvaal, K., and Ratnaweera, H. (2019). Explicit and interpretable nonlinear soft sensor models for influent surveillance at a full-scale wastewater treatment plant. *Journal of Process Control* 77: 1–6. DOI: 10.1016/J.JPROCONT.2019.03.005.

Wasswa, J., Mladenov, N., and Pearce, W. (2019). Assessing the potential of fluorescence spectroscopy to monitor contaminants in source waters and water reuse systems. *Environmental Science: Water Research and Technology.* DOI: 10.1039/c8ew00472b.

Winkler, M. K., Kleerebezem, R., De Bruin, L. M., Verheijen, P. J., Abbas, B., Habermacher, J., and Van Loosdrecht, M. C. (2013). Microbial diversity differences within aerobic granular sludge and activated sludge flocs. *Applied Microbiology and Biotechnology.* DOI: 10.1007/s00253-012-4472-7.

Zepp, R. G., Sheldon, W. M., and Moran, M. A. (2004). Dissolved organic fluorophores in southeastern US coastal waters: Correction method for eliminating Rayleigh and Raman scattering peaks in excitation-emission matrices. In: *Marine Chemistry.* Vol. 89. 1-4. Elsevier: 15–36. DOI: 10.1016/j.marchem.2004.02.006.

Appendix A. Measured 3D-EEMs

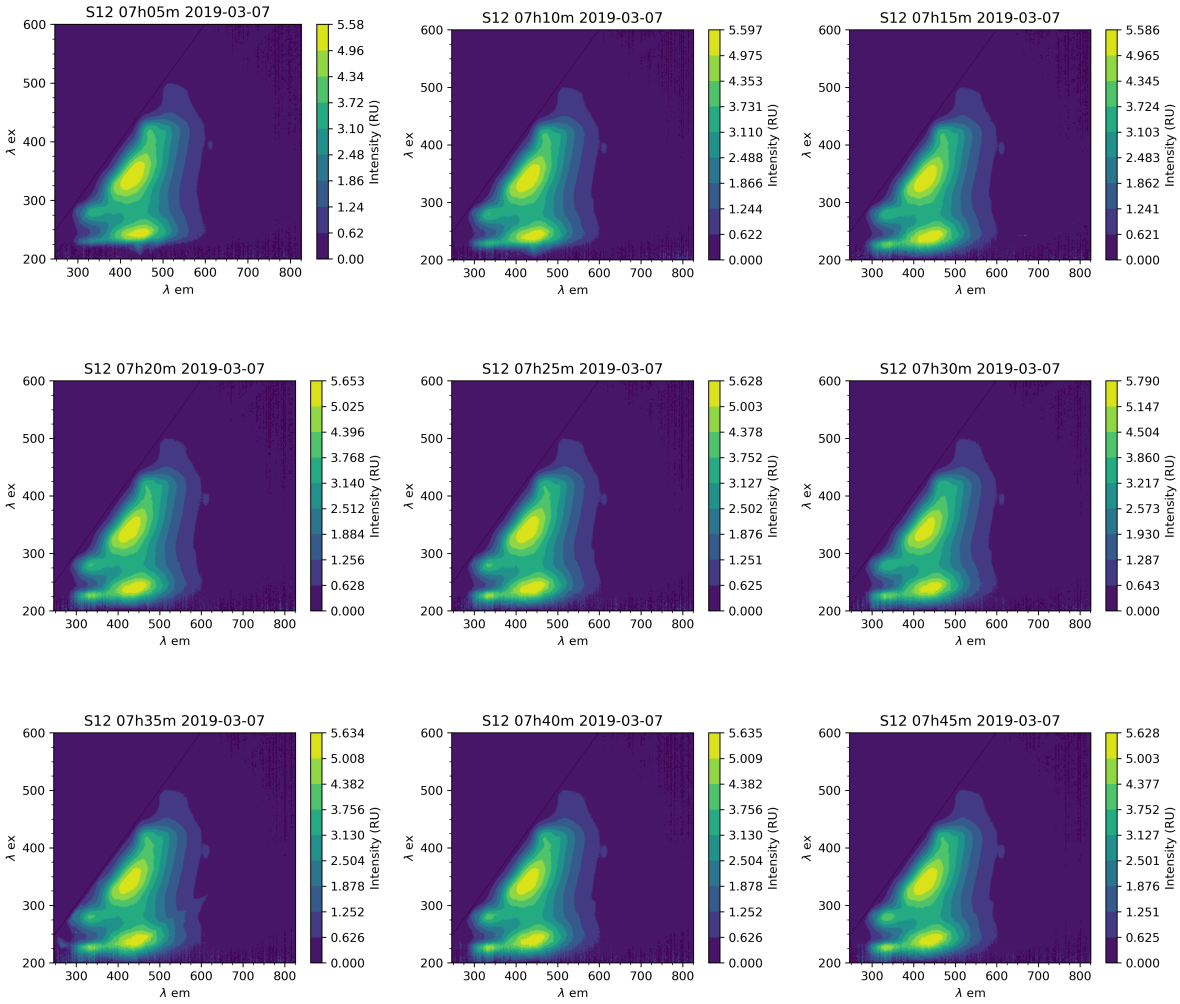

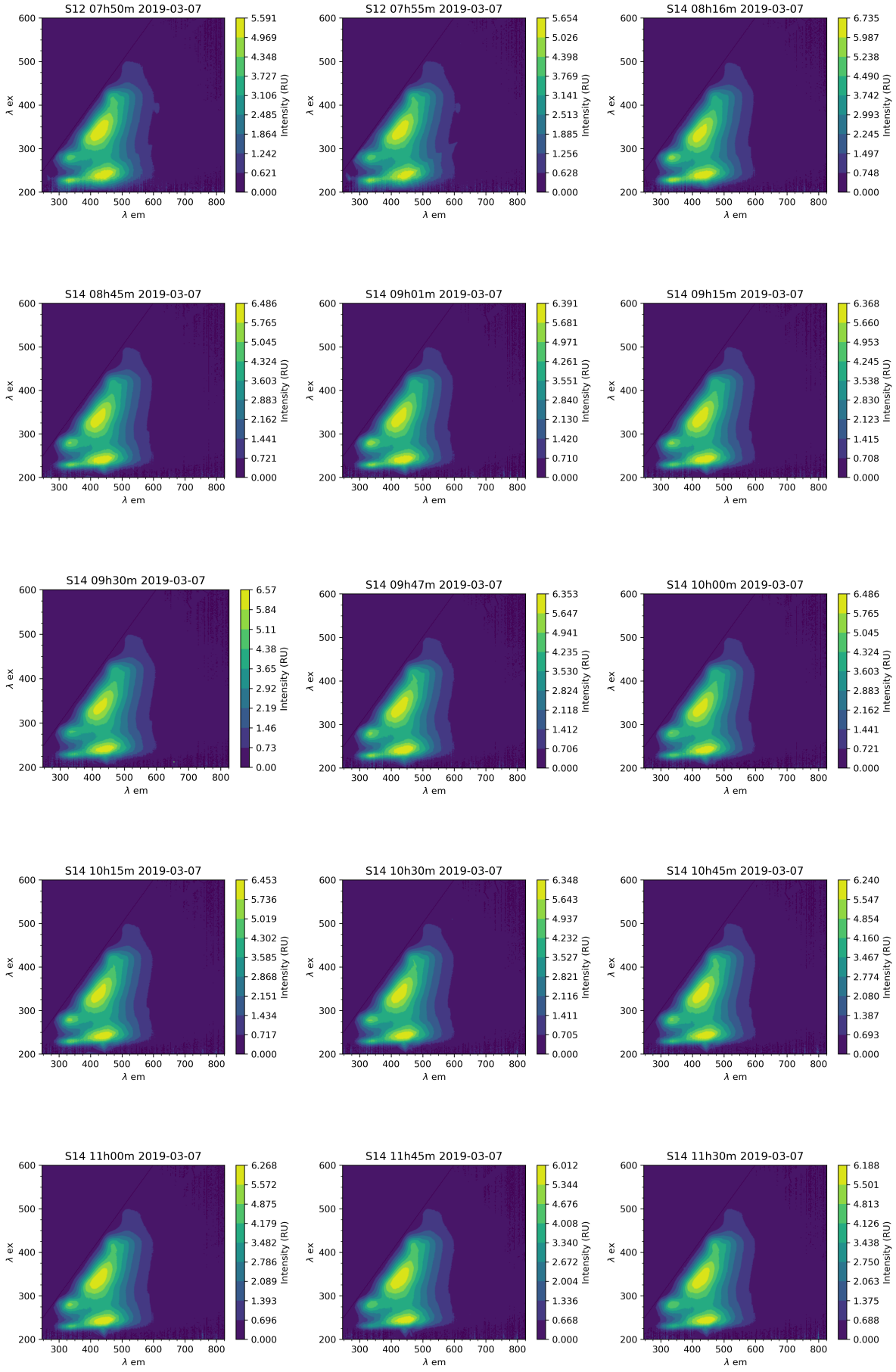
S12 07h50m 2019-03-07
S12 07h55m 2019-03-07
S14 08h16m 2019-03-07
S14 08h45m 2019-03-07
S14 09h01m 2019-03-07
S14 09h15m 2019-03-07
S14 09h30m 2019-03-07
S14 09h47m 2019-03-07
S14 10h00m 2019-03-07
S14 10h15m 2019-03-07
S14 10h30m 2019-03-07
S14 10h45m 2019-03-07
S14 11h00m 2019-03-07
S14 11h45m 2019-03-07
S14 11h30m 2019-03-07
λ ex
λ em
Intensity (RU)

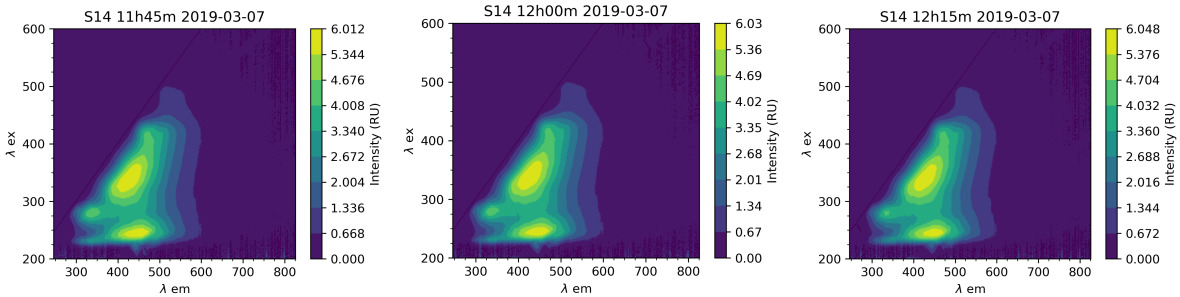
S14 11h45m 2019-03-07
S14 12h00m 2019-03-07
S14 12h15m 2019-03-07
λ ex
λ em
Intensity (RU)

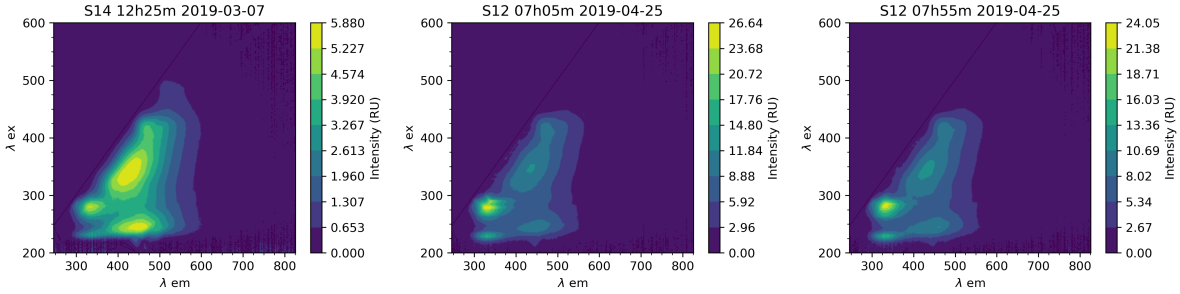
S14 12h25m 2019-03-07
S12 07h05m 2019-04-25
S12 07h55m 2019-04-25
λ ex
λ em
Intensity (RU)

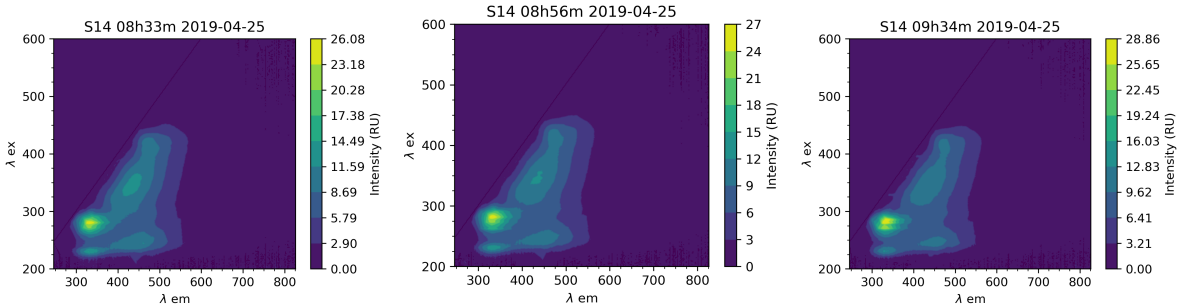
S14 08h33m 2019-04-25
S14 08h56m 2019-04-25
S14 09h34m 2019-04-25
λ ex
λ em
Intensity (RU)

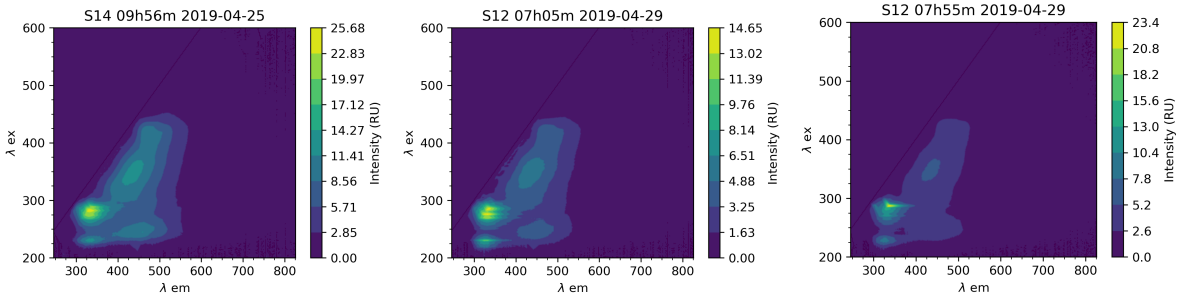
S14 09h56m 2019-04-25
S12 07h05m 2019-04-29
S12 07h55m 2019-04-29
λ ex
λ em
Intensity (RU)

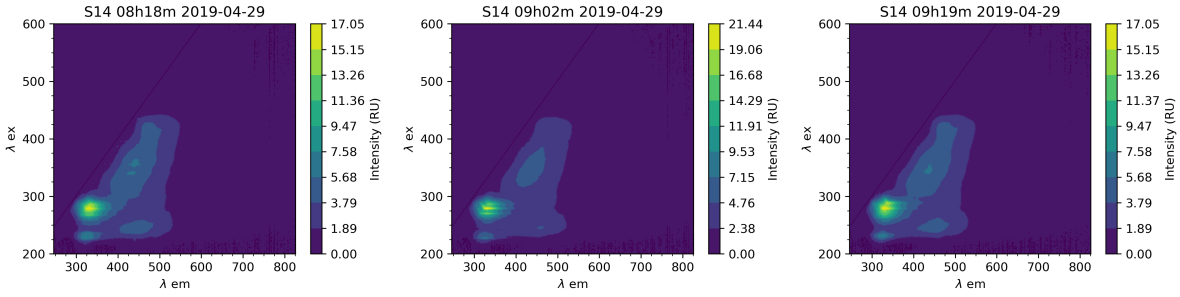
S14 08h18m 2019-04-29
S14 09h02m 2019-04-29
S14 09h19m 2019-04-29
λ ex
λ em
Intensity (RU)

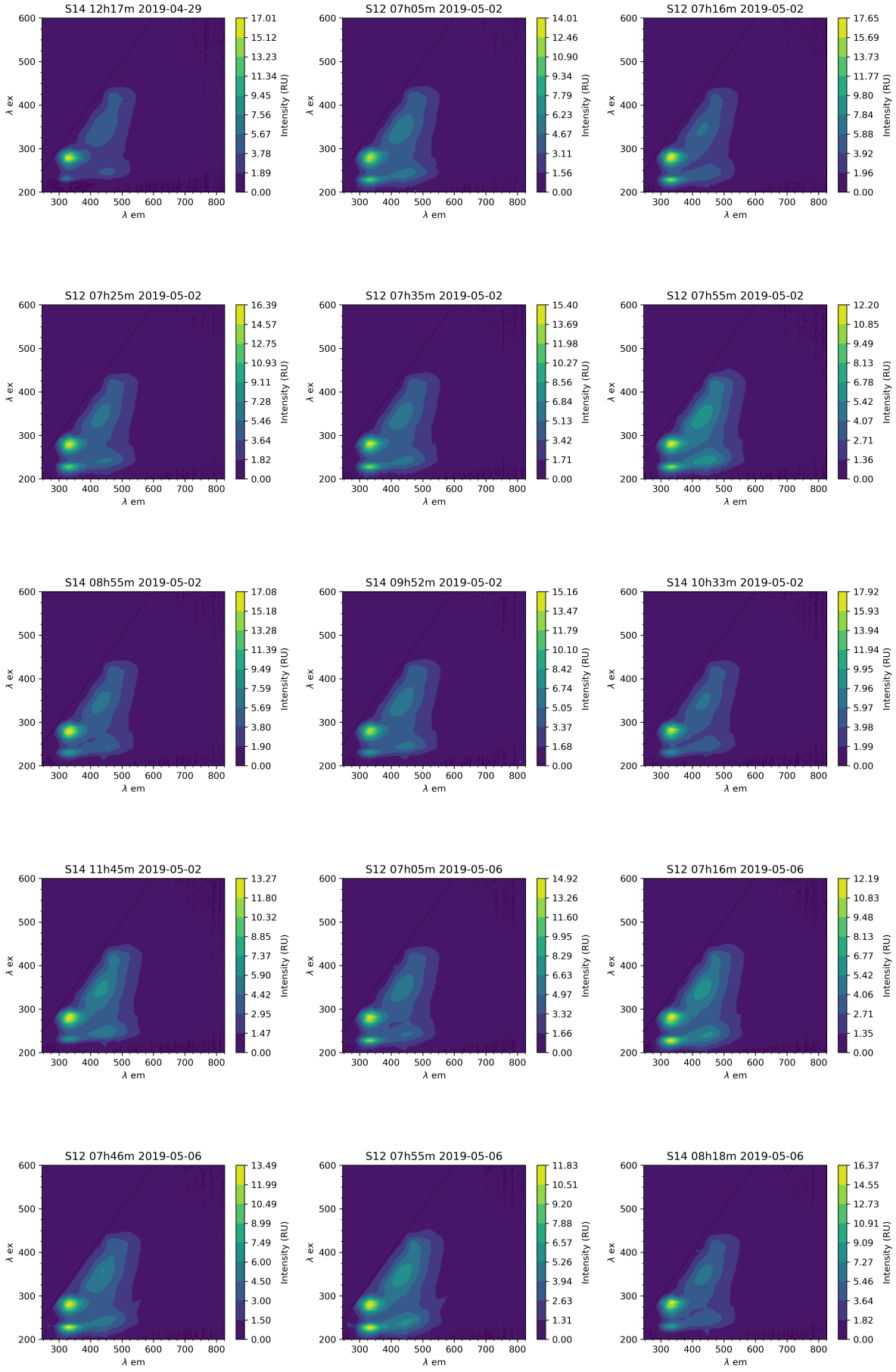
S14 12h17m 2019-04-29
S12 07h05m 2019-05-02
S12 07h16m 2019-05-02
S12 07h25m 2019-05-02
S12 07h35m 2019-05-02
S12 07h55m 2019-05-02
S14 08h55m 2019-05-02
S14 09h52m 2019-05-02
S14 10h33m 2019-05-02
S14 11h45m 2019-05-02
S12 07h05m 2019-05-06
S12 07h16m 2019-05-06
S12 07h46m 2019-05-06
S12 07h55m 2019-05-06
S14 08h18m 2019-05-06
λ ex
λ em
Intensity (RU)

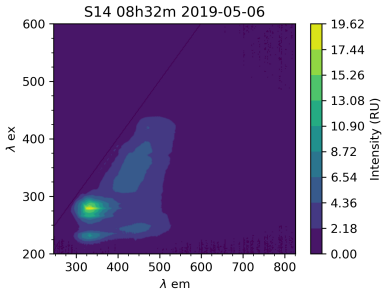
S14 08h32m 2019-05-06
λ ex
λ em
Intensity (RU)
600
500
400
300
200
300 400 500 600 700 800
19.62 17.44 15.26 13.08 10.90 8.72 6.54 4.36 2.18 0.00

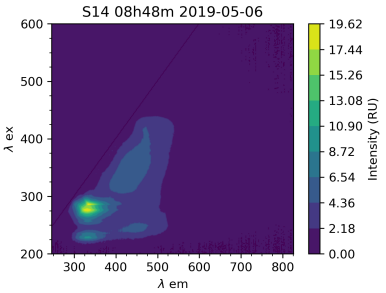
S14 08h48m 2019-05-06
λ ex
λ em
Intensity (RU)
600
500
400
300
200
300 400 500 600 700 800
19.62 17.44 15.26 13.08 10.90 8.72 6.54 4.36 2.18 0.00

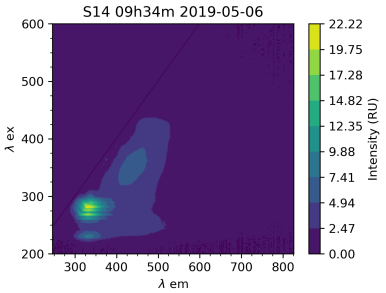
S14 09h34m 2019-05-06
λ ex
λ em
Intensity (RU)
600
500
400
300
200
300 400 500 600 700 800
22.22 19.75 17.28 14.82 12.35 9.88 7.41 4.94 2.47 0.00

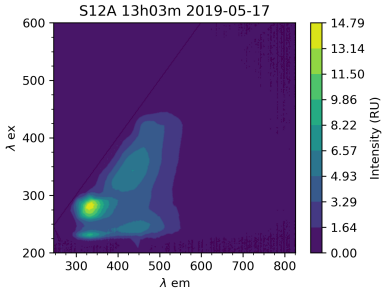
S12A 13h03m 2019-05-17
λ ex
λ em
Intensity (RU)
600
500
400
300
200
300 400 500 600 700 800
14.79 13.14 11.50 9.86 8.22 6.57 4.93 3.29 1.64 0.00

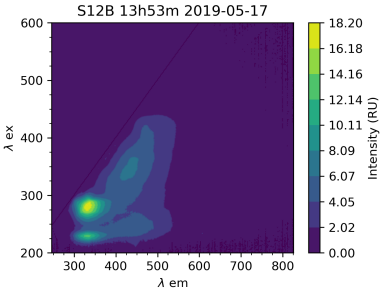
S12B 13h53m 2019-05-17
λ ex
λ em
Intensity (RU)
600
500
400
300
200
300 400 500 600 700 800
18.20 16.18 14.16 12.14 10.11 8.09 6.07 4.05 2.02 0.00

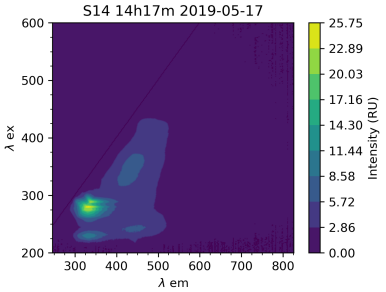
S14 14h17m 2019-05-17
λ ex
λ em
Intensity (RU)
600
500
400
300
200
300 400 500 600 700 800
25.75 22.89 20.03 17.16 14.30 11.44 8.58 5.72 2.86 0.00

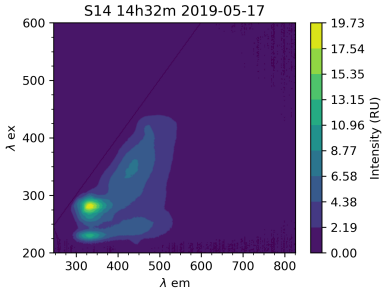
S14 14h32m 2019-05-17
λ ex
λ em
Intensity (RU)
600
500
400
300
200
300 400 500 600 700 800
19.73 17.54 15.35 13.15 10.96 8.77 6.58 4.38 2.19 0.00

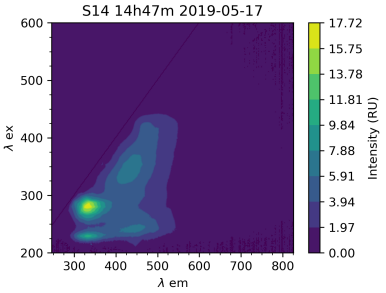
S14 14h47m 2019-05-17
λ ex
λ em
Intensity (RU)
600
500
400
300
200
300 400 500 600 700 800
17.72 15.75 13.78 11.81 9.84 7.88 5.91 3.94 1.97 0.00

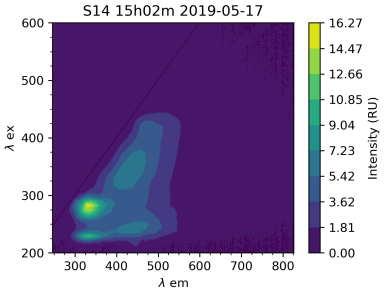
S14 15h02m 2019-05-17
λ ex
λ em
Intensity (RU)
600
500
400
300
200
300 400 500 600 700 800
16.27 14.47 12.66 10.85 9.04 7.23 5.42 3.62 1.81 0.00

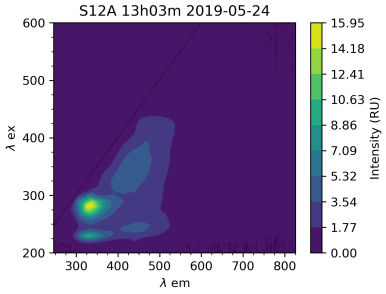
S12A 13h03m 2019-05-24
λ ex
λ em
Intensity (RU)
600
500
400
300
200
300 400 500 600 700 800
15.95 14.18 12.41 10.63 8.86 7.09 5.32 3.54 1.77 0.00

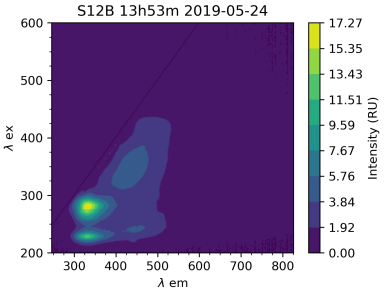
S12B 13h53m 2019-05-24
λ ex
λ em
Intensity (RU)
600
500
400
300
200
300 400 500 600 700 800
17.27 15.35 13.43 11.51 9.59 7.67 5.76 3.84 1.92 0.00

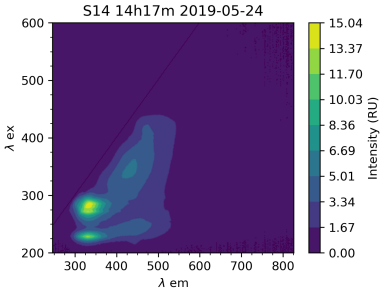
S14 14h17m 2019-05-24
λ ex
λ em
Intensity (RU)
600
500
400
300
200
300 400 500 600 700 800
15.04 13.37 11.70 10.03 8.36 6.69 5.01 3.34 1.67 0.00

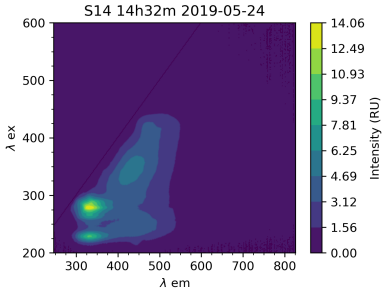
S14 14h32m 2019-05-24
λ ex
λ em
Intensity (RU)
600
500
400
300
200
300 400 500 600 700 800
14.06 12.49 10.93 9.37 7.81 6.25 4.69 3.12 1.56 0.00

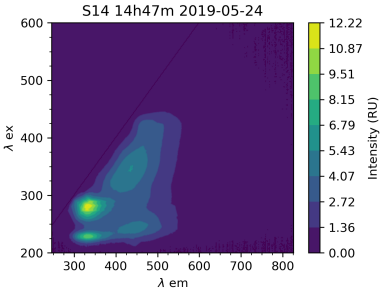
S14 14h47m 2019-05-24
λ ex
λ em
Intensity (RU)
600
500
400
300
200
300 400 500 600 700 800
12.22 10.87 9.51 8.15 6.79 5.43 4.07 2.72 1.36 0.00

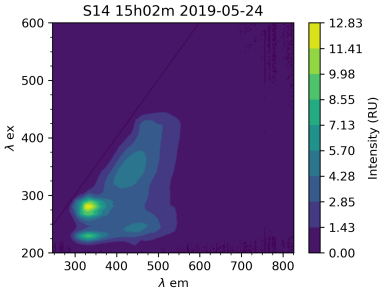
S14 15h02m 2019-05-24
λ ex
λ em
Intensity (RU)
600
500
400
300
200
300 400 500 600 700 800
12.83 11.41 9.98 8.55 7.13 5.70 4.28 2.85 1.43 0.00

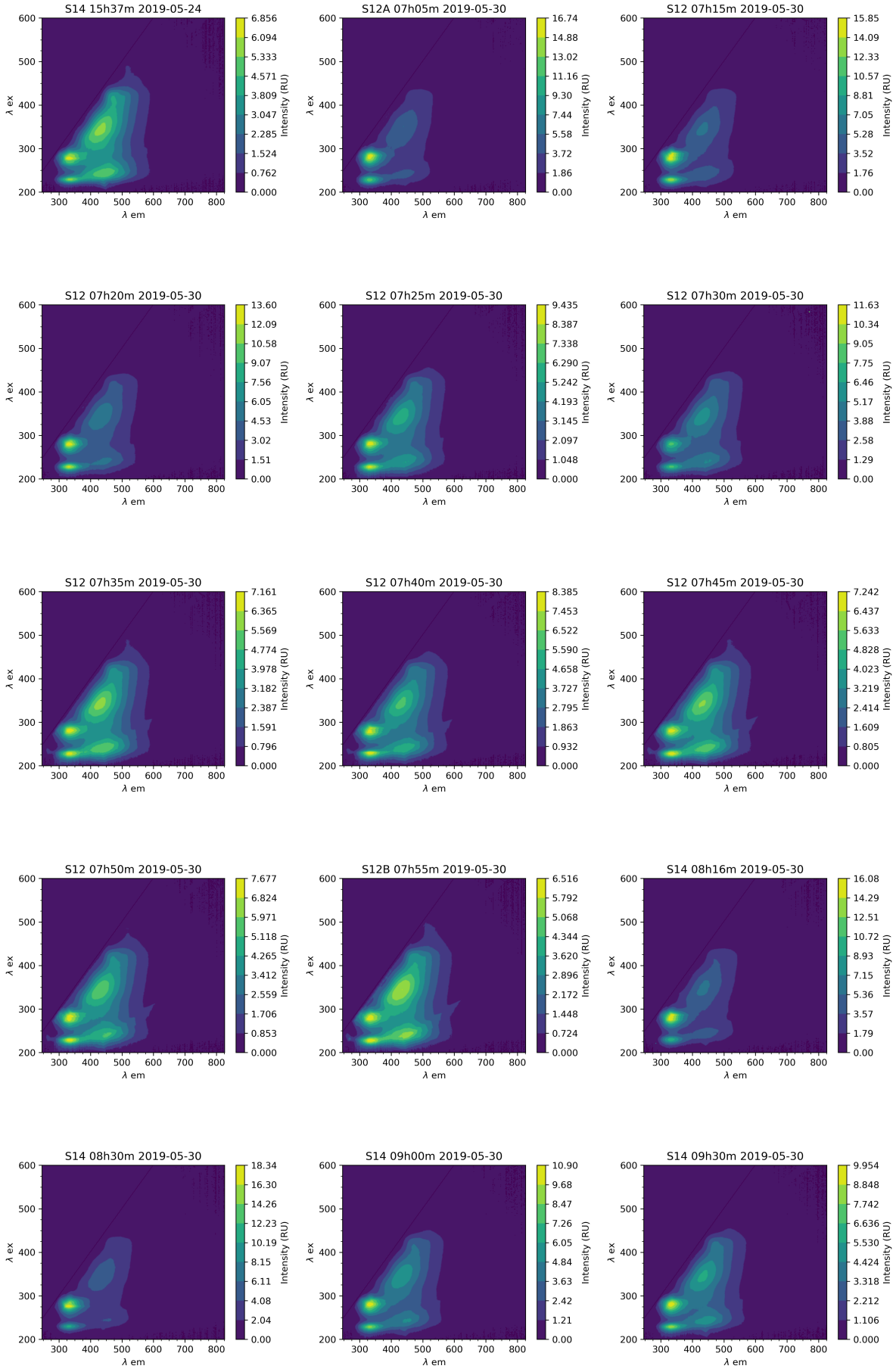
S14 15h37m 2019-05-24
S12A 07h05m 2019-05-30
S12 07h15m 2019-05-30
S12 07h20m 2019-05-30
S12 07h25m 2019-05-30
S12 07h30m 2019-05-30
S12 07h35m 2019-05-30
S12 07h40m 2019-05-30
S12 07h45m 2019-05-30
S12 07h50m 2019-05-30
S12B 07h55m 2019-05-30
S14 08h16m 2019-05-30
S14 08h30m 2019-05-30
S14 09h00m 2019-05-30
S14 09h30m 2019-05-30
λ ex
λ em
Intensity (RU)

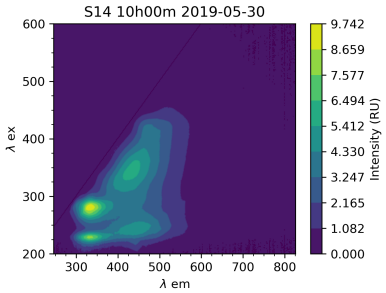
S14 10h00m 2019-05-30
λ ex
λ em
Intensity (RU)
9.742
8.659
7.577
6.494
5.412
4.330
3.247
2.165
1.082
0.000

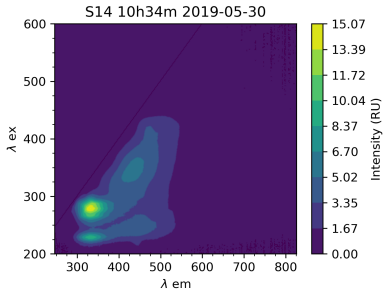
S14 10h34m 2019-05-30
λ ex
λ em
Intensity (RU)
15.07
13.39
11.72
10.04
8.37
6.70
5.02
3.35
1.67
0.00

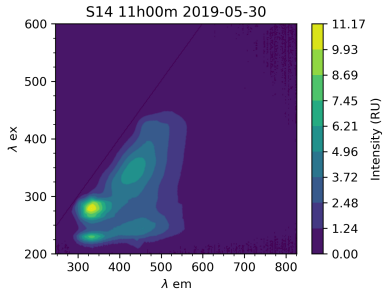
S14 11h00m 2019-05-30
λ ex
λ em
Intensity (RU)
11.17
9.93
8.69
7.45
6.21
4.96
3.72
2.48
1.24
0.00

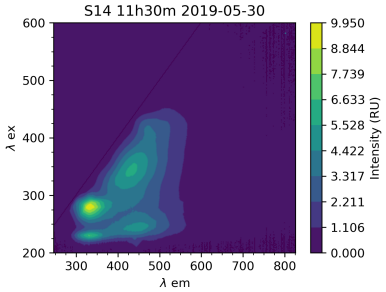
S14 11h30m 2019-05-30
λ ex
λ em
Intensity (RU)
9.950
8.844
7.739
6.633
5.528
4.422
3.317
2.211
1.106
0.000

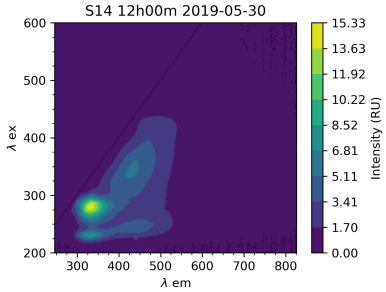
S14 12h00m 2019-05-30
λ ex
λ em
Intensity (RU)
15.33
13.63
11.92
10.22
8.52
6.81
5.11
3.41
1.70
0.00

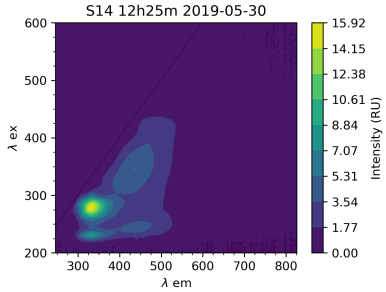
S14 12h25m 2019-05-30
λ ex
λ em
Intensity (RU)
15.92
14.15
12.38
10.61
8.84
7.07
5.31
3.54
1.77
0.00

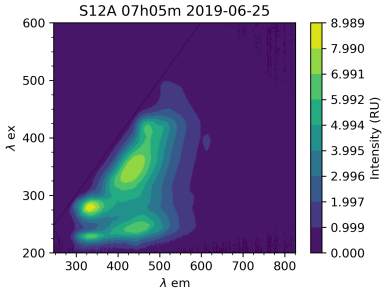
S12A 07h05m 2019-06-25
λ ex
λ em
Intensity (RU)
8.989
7.990
6.991
5.992
4.994
3.995
2.996
1.997
0.999
0.000

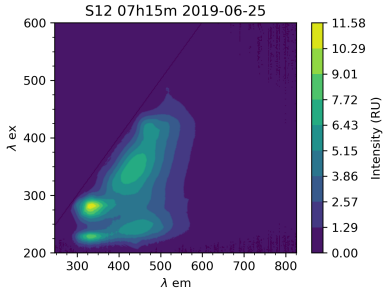
S12 07h15m 2019-06-25
λ ex
λ em
Intensity (RU)
11.58
10.29
9.01
7.72
6.43
5.15
3.86
2.57
1.29
0.00

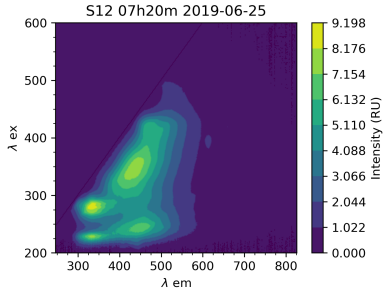
S12 07h20m 2019-06-25
λ ex
λ em
Intensity (RU)
9.198
8.176
7.154
6.132
5.110
4.088
3.066
2.044
1.022
0.000

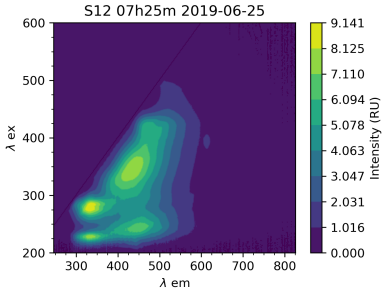
S12 07h25m 2019-06-25
λ ex
λ em
Intensity (RU)
9.141
8.125
7.110
6.094
5.078
4.063
3.047
2.031
1.016
0.000

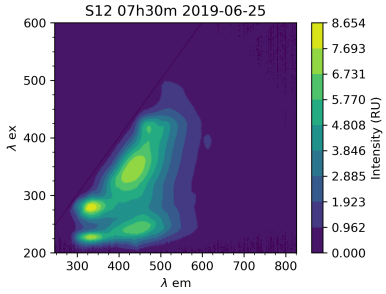
S12 07h30m 2019-06-25
λ ex
λ em
Intensity (RU)
8.654
7.693
6.731
5.770
4.808
3.846
2.885
1.923
0.962
0.000

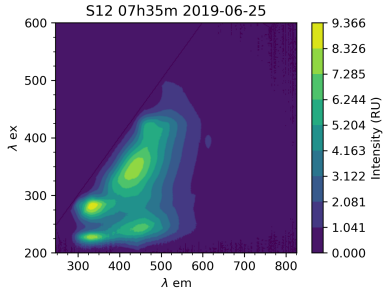
S12 07h35m 2019-06-25
λ ex
λ em
Intensity (RU)
9.366
8.326
7.285
6.244
5.204
4.163
3.122
2.081
1.041
0.000

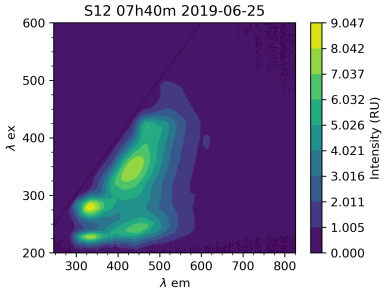
S12 07h40m 2019-06-25
λ ex
λ em
Intensity (RU)
9.047
8.042
7.037
6.032
5.026
4.021
3.016
2.011
1.005
0.000

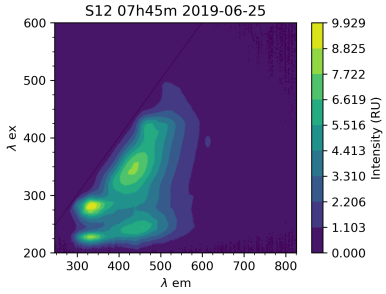
S12 07h45m 2019-06-25
λ ex
λ em
Intensity (RU)
9.929
8.825
7.722
6.619
5.516
4.413
3.310
2.206
1.103
0.000

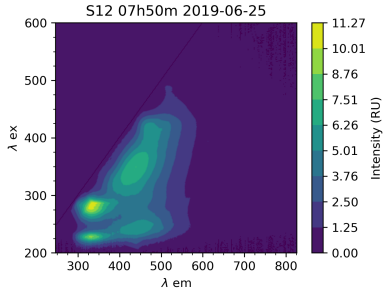
S12 07h50m 2019-06-25
λ ex
λ em
Intensity (RU)
11.27
10.01
8.76
7.51
6.26
5.01
3.76
2.50
1.25
0.00

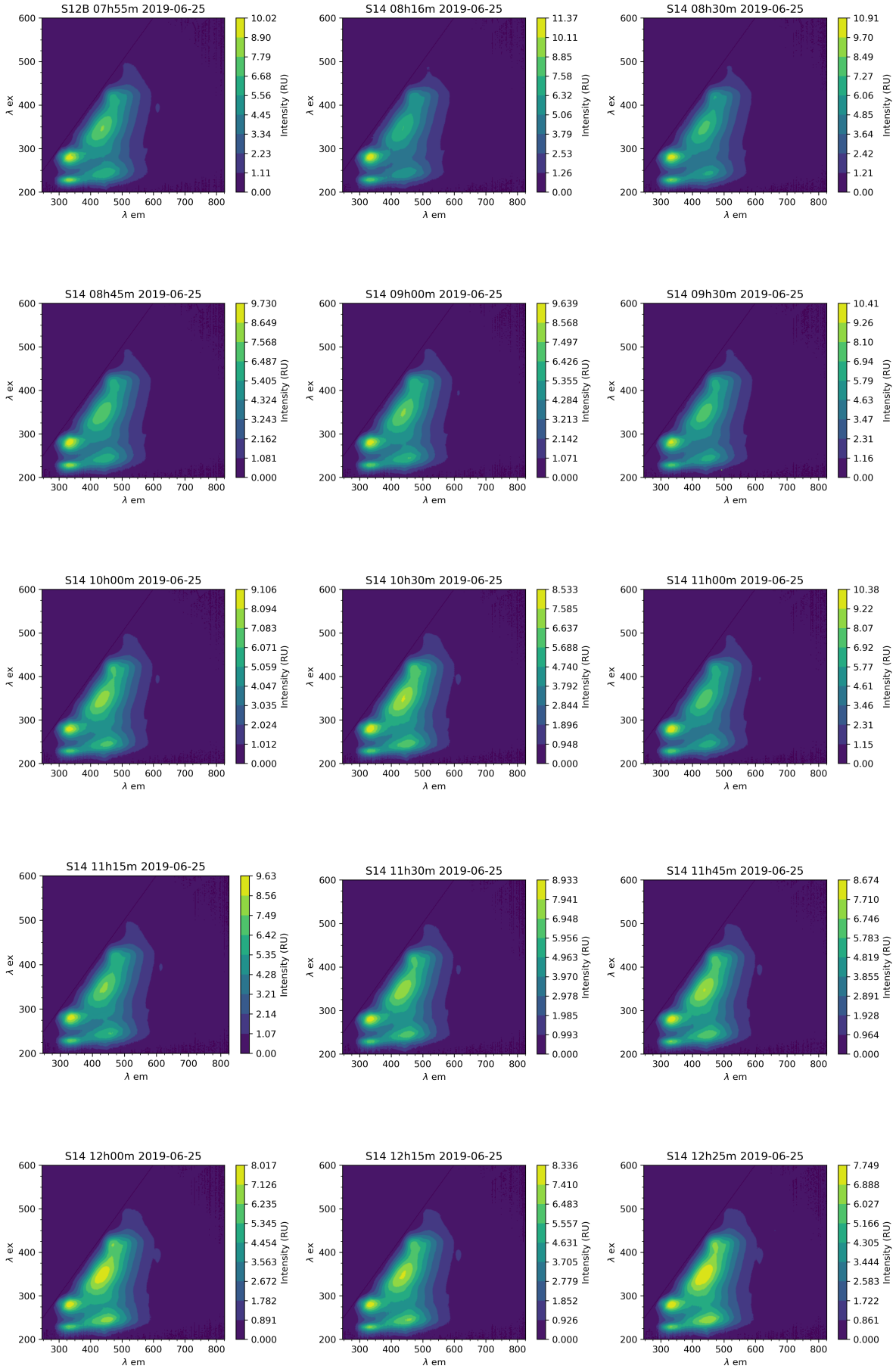
S12B 07h55m 2019-06-25
S14 08h16m 2019-06-25
S14 08h30m 2019-06-25
S14 08h45m 2019-06-25
S14 09h00m 2019-06-25
S14 09h30m 2019-06-25
S14 10h00m 2019-06-25
S14 10h30m 2019-06-25
S14 11h00m 2019-06-25
S14 11h15m 2019-06-25
S14 11h30m 2019-06-25
S14 11h45m 2019-06-25
S14 12h00m 2019-06-25
S14 12h15m 2019-06-25
S14 12h25m 2019-06-25
λ ex
λ em
Intensity (RU)

Appendix B. FRI intensities and nutrient values

Table B.1: 2019-03-07 anaerobic FRI intensities and nutrient values

Time	PO4-P (mg/L)	$\Phi_{\mathrm{I+II},n}$	$\Phi_{\mathrm{III},n}$	$\Phi_{\mathrm{IV},n}$	$\Phi_{\mathrm{V},n}$	$\Phi_{\mathrm{T},n}$
07:05:00	6.80	358338.03	357623.77	230472.22	145611.93	1092045.95
07:10:00	49.11	456177.33	375749.17	239310.82	147247.19	1218484.52
07:15:00	120.16	540755.87	391454.30	237207.34	146604.38	1316021.90
07:20:00	190.17	556278.21	393144.66	244623.45	147648.27	1341694.59
07:25:00	265.10	567846.39	396163.29	245463.37	148141.74	1357614.80
07:30:00	303.98	567687.00	399195.84	243318.94	148807.30	1359009.08
07:35:00	349.12	595470.70	396036.35	259329.01	151237.41	1402073.47
07:40:00	383.86	572336.98	393942.78	249936.74	148798.03	1365014.53
07:45:00	379.27	587178.22	394537.93	257199.00	150238.13	1389153.28
07:55:00	376.3	586596.32	390737.08	264715.11	151219.65	1393268.16

Table B.2: 2019-03-07 aerobic FRI intensities and nutrient values

Time	PO4-P (mg/L)	NH3-N (mg/L)	NO3-N (mg/L)	NO2-N (mg/L)	$\Phi_{\mathrm{I+II},n}$	$\Phi_{\mathrm{III},n}$	$\Phi_{\mathrm{IV},n}$	$\Phi_{\mathrm{V},n}$	$\Phi_{\mathrm{T},n}$
08:16:00	167.3	100.9	0.3	0.6	702634.70	450383.85	328509.66	171411.02	1652939.23
08:45:00		89.1	0.9	1.2	622474.99	431524.07	310809.28	167322.90	1532131.24
09:01:30	128	87.1	0.9	1.2	612652.79	424510.45	315851.96	166746.70	1519761.90
09:30:00	98.8	74.6	1.3	1.3	564218.43	429919.06	284447.68	166134.05	1444719.21
10:00:00	80.1	66.8	1.4	1.6	580960.71	426742.94	303531.56	168094.21	1479329.42
10:30:00	55	54.7	2.6	2.1	540080.46	418223.08	294703.46	166034.73	1419041.74
11:00:00	34.3	44.6	2.7	2.3	538853.82	414429.66	303628.50	166541.90	1423453.89
11:15:00		38.7	3.7	2.7	496647.22	410257.88	289057.56	165142.86	1361105.52
11:30:00		32.0	4.4	3.0	473903.80	401161.20	290821.60	163885.99	1329772.59
11:45:00		26.9	5.5	3.7	414523.87	386245.58	278093.03	160424.59	1239287.08
12:00:00	3.2	21.9	5.9	3.5	391503.19	382854.81	275015.73	160228.21	1209601.94
12:15:30		16.7	7.5	3.9	369165.08	377592.22	262884.87	158030.55	1167672.72
12:25:00	0.4	13.5	8.3	3.9	393290.61	366894.33	298111.21	158278.85	1216575.00

Table B.3: 2019-05-30 anaerobic FRI intensities and nutrient values

Time	PO4-P (mg/L)	$\Phi_{\mathrm{I+II},n}$	$\Phi_{\mathrm{III},n}$	$\Phi_{\mathrm{IV},n}$	$\Phi_{\mathrm{V},n}$	$\Phi_{\mathrm{T},n}$
07:05:00	19.04	1089257.03	326642.35	667668.33	171166.32	2254734.04
07:15:00	152.00	1159647.81	357285.39	664563.68	174675.02	2356171.90
07:20:00	220.24	1076920.70	368062.54	558735.12	169395.39	2173113.75
07:25:00	263.37	869473.76	390481.76	427272.12	162088.22	1849315.85
07:30:00	300.43	822840.27	386825.38	406801.30	160271.52	1776738.47
07:35:00	303.60	762275.17	402828.55	359383.41	160615.54	1685102.66
07:40:00	303.51	821636.69	389156.99	404097.87	163620.05	1778511.60
07:45:00	308.80	773190.82	391136.58	369475.90	160454.65	1694257.96
07:50:00	308.33	785662.77	388758.34	397053.93	163145.00	1734620.04
07:55:00	311.15	737517.43	394237.56	355528.62	160621.56	1647905.17

Table B.4: 2019-05-30 aerobic FRI intensities and nutrient values

Time	PO4-P (mg/L)	NH3-N (mg/L)	NO3-N (mg/L)	NO2-N (mg/L)	$\Phi_{\mathrm{I+II},n}$	$\Phi_{\mathrm{III},n}$	$\Phi_{\mathrm{IV},n}$	$\Phi_{\mathrm{V},n}$	$\Phi_{\mathrm{T},n}$
08:16:30	152.47	71.35	0.06	0.09	947209.49	331252.37	664202.57	177372.61	2120037.05
08:30:00	140.94	65.58	0.34	0.79	932356.08	315401.05	687040.27	174773.66	2109571.07
09:00:00	106.15	56.29	0.25	0.52	853693.59	367970.37	487040.14	167839.36	1876543.46
09:30:00	71.99	48.64	0.31	0.70	807214.78	365901.49	455655.17	164408.95	1793180.39
10:00:00	46.11	41.44	0.40	0.79	785501.42	373624.07	446232.35	164382.97	1769740.81
10:34:00	18.83	32.90	0.70	1.36	871379.06	344361.82	629106.89	173112.28	2017960.05
11:00:00	3.67	28.32	0.79	1.53	772453.81	353899.26	509337.51	165229.20	1800919.78
11:30:00	0.29	21.73	1.47	2.47	673715.23	344537.56	456167.70	159434.46	1633854.95
12:00:00	0.24	15.16	1.95	2.71	771061.72	308466.19	632457.22	165658.79	1877643.92
12:25:00	0.29	10.16	2.28	2.53	771512.98	300987.59	660721.20	165259.75	1898481.52

Table B.5: 2019-06-25 anaerobic FRI intensities and nutrient values

Time	PO4-P (mg/L)	$\Phi_{\mathrm{I+II},n}$	$\Phi_{\mathrm{III},n}$	$\Phi_{\mathrm{IV},n}$	$\Phi_{\mathrm{V},n}$	$\Phi_{\mathrm{T},n}$
07:05:00	105.83	768859.87	490880.40	456627.89	220420.70	1936788.85
07:15:00	159.80	879925.29	464748.25	521289.02	214844.65	2080807.21
07:20:00	169.66	803811.08	485600.19	456538.50	217105.03	1963054.80
07:25:00	194.96	827227.76	484854.66	470073.81	219645.24	2001801.47
07:30:00	188.63	828791.25	482871.79	443649.88	212291.58	1967604.50
07:35:00	199.23	852385.12	484993.23	469385.41	219635.43	2026399.20
07:40:00	249.33	843145.75	483648.57	463868.15	218667.73	2009330.20
07:45:00	230.52	867650.49	482068.74	484225.06	221027.88	2054972.17
07:50:00	244.00	894781.33	452572.98	523004.09	214294.33	2084652.74
07:55:00	226.56	886780.91	482218.38	491760.61	221262.89	2082022.79

Table B.6: 2019-06-25 aerobic FRI intensities and nutrient values

Time	PO4-P (mg/L)	NH3-N (mg/L)	NO3-N (mg/L)	NO2-N (mg/L)	$\Phi_{\mathrm{I+II},n}$	$\Phi_{\mathrm{III},n}$	$\Phi_{\mathrm{IV},n}$	$\Phi_{\mathrm{V},n}$	$\Phi_{\mathrm{T},n}$
08:16:30	142.19	214.91	0.06	0.13	890857.76	449632.70	535980.03	218515.51	2094986.01
08:30:00	135.69	212.04	0.08	0.13	896332.18	464415.83	505740.77	217559.69	2084048.46
08:45:00	131.29	209.04	0.07	0.12	872138.28	455598.92	482775.75	209908.30	2020421.26
09:00:00	128.76	205.61	0.13	0.29	797238.12	464265.92	469158.52	215061.67	1945724.24
09:30:00	124.43	201.97	0.11	0.29	802501.84	455742.75	482302.94	215318.72	1955866.25
10:00:00	100.42	190.69	0.11	0.34	745466.64	465846.34	447869.48	214561.86	1873744.32
10:30:00	90.24	195.50	0.14	0.41	715516.78	458989.07	440684.98	213710.88	1828901.70
11:00:00	80.02	190.28	0.13	0.33	827921.94	461662.05	499478.09	217844.20	2006906.28
11:15:00	74.05	190.38	0.14	0.38	790417.73	463948.97	470093.28	216002.88	1940462.85
11:30:00	92.93	190.69	0.13	0.42	738449.52	465195.03	446068.59	213948.09	1863661.23
11:45:00	66.42	187.11	0.17	0.46	757933.85	471380.61	439065.52	214700.65	1883080.64
12:00:00	62.94	186.48	0.18	0.56	708170.09	471469.24	417120.97	213354.10	1810114.39
12:15:00	67.77	186.12	0.16	0.43	746581.97	467993.36	424281.56	208843.73	1847700.63
12:25:00	54.47	185.89	0.17	0.47	704723.55	475371.65	410278.91	212542.30	1802916.40

Table B.7: Mini-series anaerobic FRI intensities and nutrient values

Date	Time	PO4-P (mg/L)	$\Phi_{\mathrm{I+II},n}$	$\Phi_{\mathrm{III},n}$	$\Phi_{\mathrm{IV},n}$	$\Phi_{\mathrm{V},n}$	$\Phi_{\mathrm{T},n}$
2019-04-25	07:05:00	50.64	1519926.70	759362.04	1109943.76	373782.99	3763015.49
2019-04-25	07:55:00	348.05	1492625.23	750778.11	1015421.24	353039.72	3611864.30
2019-04-29	07:05:00	11.31	752677.55	325627.63	586922.74	178102.16	1843330.08
2019-04-29	07:55:00	321.06	761616.80	328053.38	635785.40	180647.02	1906102.60
2019-05-02	07:05:00	12.24	1006130.94	399057.51	594641.07	182449.25	2182278.77
2019-05-02	07:55:00	353.22	993197.11	450447.65	536436.63	193485.88	2173567.27
2019-05-06	07:05:00	8.34	1076840.12	382743.36	617626.96	187193.87	2264404.30
2019-05-06	07:55:00	352.90	1103301.94	415974.25	542306.89	186910.59	2248493.66
2019-05-09	07:05:00	1.74	728052.51	365923.06	555099.82	182213.17	1831288.57
2019-05-09	07:55:00	333.74	1219660.52	365541.64	678696.17	191969.76	2455868.10
2019-05-17	13:03:00	8.91	805468.69	411683.89	667223.47	200353.70	2084729.74
2019-05-17	13:53:00	401.80	1190876.43	427900.93	780965.21	209639.75	2609382.31
2019-05-24	13:03:00	6.48	807413.14	298400.21	628879.11	163158.74	1897851.21
2019-05-24	13:53:00	324.04	1043766.92	312743.78	687338.15	170725.63	2214574.49

Table B.8: Mini-series aerobic FRI intensities and nutrient values

Date	Time	NH3-N (mg/L)	$\Phi_{\mathrm{I+II},n}$	$\Phi_{\mathrm{III},n}$	$\Phi_{\mathrm{IV},n}$	$\Phi_{\mathrm{V},n}$	$\Phi_{\mathrm{T},n}$
2019-04-25	08:33:00	135.25	849785.87	464117.37	631569.36	243847.32	2189319.92
2019-04-25	08:56:00	121.74	1500461.64	787173.87	1157031.49	384889.19	3829556.20
2019-04-25	09:34:00	113.65	1394228.67	759112.83	1208904.98	392024.04	3754270.52
2019-04-25	09:56:00	105.47	1371429.77	776928.85	1096485.20	384913.37	3629757.20
2019-04-29	08:18:00	87.72	693573.34	344947.27	664871.80	188134.17	1891526.58
2019-04-29	09:02:00	72.47	673260.09	341692.46	717700.21	191678.90	1924331.65
2019-04-29	09:19:00	65.37	598261.08	332473.93	671061.53	187160.69	1788957.24
2019-04-29	12:17:00	6.79	503193.27	302250.67	628961.29	177580.36	1611985.59
2019-05-02	08:55:30	80.25	961958.33	411147.68	718329.63	206686.86	2298122.50
2019-05-02	09:52:30	58.17	809677.66	406594.26	603983.21	194646.16	2014901.29
2019-05-02	10:33:30	43.62	870905.39	400709.67	701545.67	205335.16	2178495.89
2019-05-02	11:45:40	17.37	717406.00	397443.66	602407.18	196027.49	1913284.33
2019-05-06	08:18:30	83.77	902753.23	384377.74	673044.59	195790.70	2155966.25
2019-05-06	08:32:45	77.97	863075.3	361423.98	693840.02	192979.33	2111318.62
2019-05-06	08:48:00	73.48	870505.44	362071.44	741430.83	199709.71	2173717.41
2019-05-06	09:34:00	52.74	758531.99	329792.85	802462.89	200691.55	2091479.28
2019-05-09	08:24:00	83.96	864519.62	380835.50	662718.00	195735.39	2103808.51
2019-05-09	08:54:35	64.27	659958.18	329507.94	675115.77	192760.73	1857342.62
2019-05-09	09:17:00	52.37	786274.51	335479.46	715719.82	190831.67	2028305.46
2019-05-09	09:56:00	30.14	583536.65	320391.39	696216.40	191733.68	1791878.12
2019-05-17	14:17:00	111.70	1035518.79	438409.15	910168.03	223986.74	2608082.72
2019-05-17	14:32:00	109.06	1107023.21	426627.81	773580.94	215218.86	2522450.83
2019-05-17	14:47:00	105.14	986067.99	450166.03	719489.10	212323.39	2368046.51
2019-05-17	15:02:00	99.69	987696.08	452638.04	670219.09	208682.11	2319235.33
2019-05-24	14:17:00	61.85	984027.13	328013.91	618342.66	167489.70	2097873.40
2019-05-24	14:32:00	75.84	880744.65	345021.41	553686.46	166592.25	1946044.77
2019-05-24	14:47:00	78.11	842578.22	348694.76	528869.70	164992.05	1885134.74
2019-05-24	15:02:00	71.25	805238.16	345074.75	531535.31	164053.57	1845901.79
2019-05-24	15:37:00	61.37	600815.79	372881.95	334474.98	154428.60	1462601.31

Appendix C. PARAFAC model

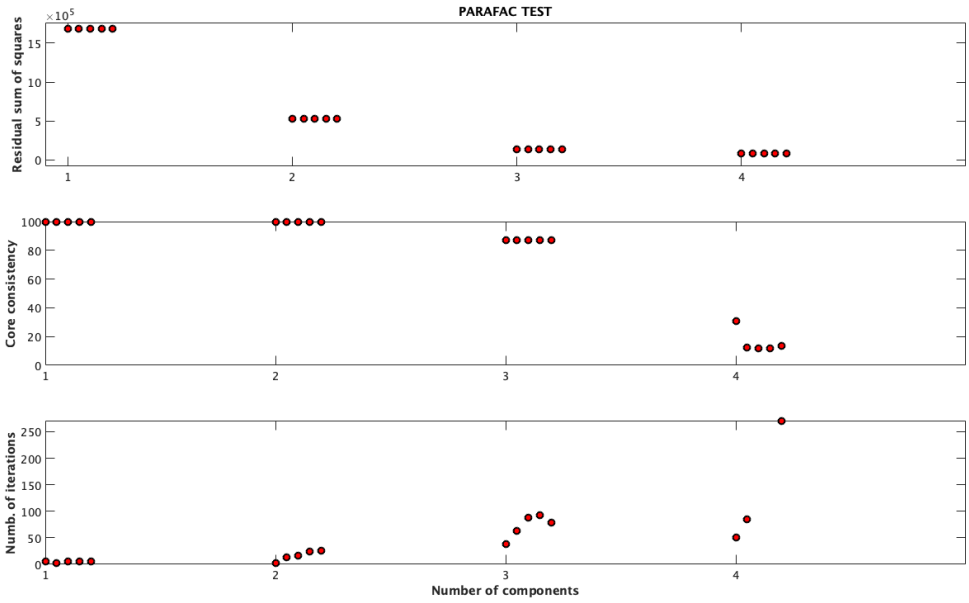

Figure C.1: Selection parameters for anaerobic PARAFAC model

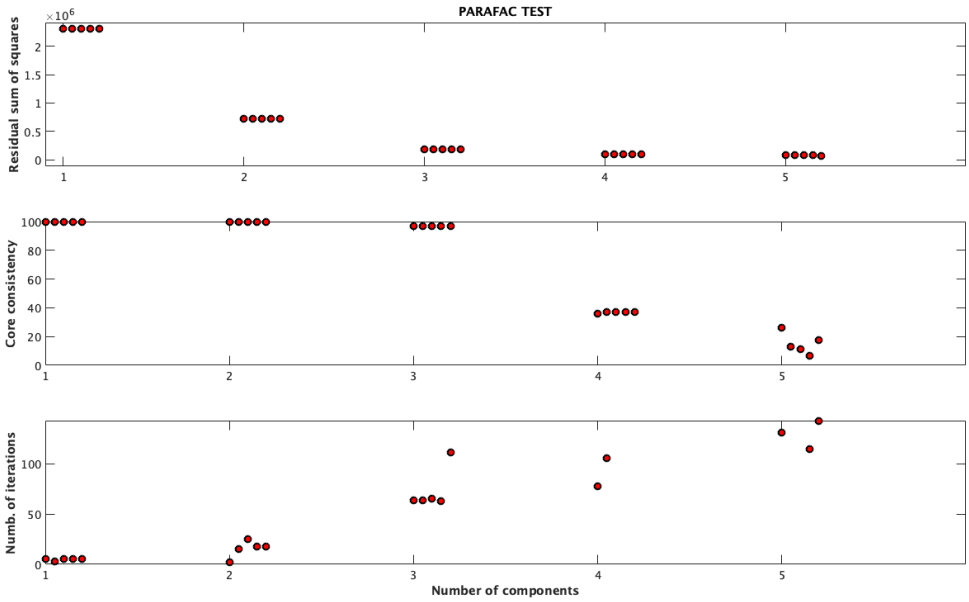

Figure C.2: Selection parameters for aerobic PARAFAC model

Table C.1: Anaerobic PARAFAC model component 1 and component 2 score

Sample	C1 - Score	C2 - Score
S12 2019-03-07 07h05m	388.9312808	121.6766047
S12 2019-03-07 07h10m	398.3995717	139.0156823
S12 2019-03-07 07h15m	404.730608	152.8447153
S12 2019-03-07 07h20m	406.0893553	158.2277034
S12 2019-03-07 07h25m	408.2425748	160.6989983
S12 2019-03-07 07h30m	411.0971733	159.6210772
S12 2019-03-07 07h35m	409.21532	164.1223738
S12 2019-03-07 07h40m	407.3535475	162.631021
S12 2019-03-07 07h45m	409.0270386	167.5618618
S12 2019-03-07 07h55m	406.5860305	165.9002399
S12 2019-05-30 07h05m	373.2030107	411.9366508
S12 2019-05-30 07h15m	389.9384147	418.2543315
S12 2019-05-30 07h20m	398.9149571	362.3948742
S12 2019-05-30 07h25m	410.9905633	277.288264
S12 2019-05-30 07h30m	407.31174	258.5949523
S12 2019-05-30 07h35m	419.5003667	229.0055155
S12 2019-05-30 07h40m	413.2247587	255.6394672
S12 2019-05-30 07h45m	411.2712963	232.7790723
S12 2019-05-30 07h50m	412.0473285	246.6389608
S12 2019-05-30 07h55m	413.9128	220.6245776
S12 2019-06-25 07h05m	559.0397096	268.2853051
S12 2019-06-25 07h15m	528.1462623	312.1265174
S12 2019-06-25 07h20m	549.1499996	272.4433885
S12 2019-06-25 07h25m	553.0147967	281.6809537
S12 2019-06-25 07h30m	540.7980678	270.2165964
S12 2019-06-25 07h35m	553.6238131	284.6883128
S12 2019-06-25 07h40m	551.7554722	281.3150117
S12 2019-06-25 07h45m	553.2774062	293.9927732
S12 2019-06-25 07h50m	523.0574516	315.1257565
S12 2019-06-25 07h55m	552.3455545	299.095492

Table C.2: Aerobic PARAFAC model component 1 and component 2 score

Sample	C1 - Score	C2 - Score
S14 2019-03-07 08h16m	464.6418694	202.1416319
S14 2019-03-07 08h45m	451.0850045	184.4604444
S14 2019-03-07 09h01m	446.5289777	186.3317717
S14 2019-03-07 09h30m	450.730046	165.99895
S14 2019-03-07 10h00m	451.3871685	176.7461664
S14 2019-03-07 10h30m	445.0872519	168.6990741
S14 2019-03-07 11h00m	443.8262885	172.1674169
S14 2019-03-07 11h15m	441.4628981	161.0921592
S14 2019-03-07 11h30m	435.4839933	159.5806385
S14 2019-03-07 11h45m	424.7652624	147.8518127
S14 2019-03-07 12h00m	423.9310216	144.4342486
S14 2019-03-07 12h15m	419.0058294	136.4206692
S14 2019-03-07 12h25m	411.2206239	156.2335369
S14 2019-05-30 08h16m	393.0652785	392.6879354
S14 2019-05-30 08h30m	377.7245333	403.3778292
S14 2019-05-30 09h00m	409.3225748	297.0200332
S14 2019-05-30 09h30m	405.7686251	276.4937212
S14 2019-05-30 10h00m	409.6595541	270.1018206
S14 2019-05-30 10h34m	392.8783784	365.7656585
S14 2019-05-30 11h00m	396.3849459	296.5557549
S14 2019-05-30 11h30m	388.6593349	260.0990193
S14 2019-05-30 12h00m	364.4409907	356.0795533
S14 2019-05-30 12h25m	356.8608432	370.4126434
S14 2019-06-25 08h16m	535.8740747	321.011461
S14 2019-06-25 08h30m	543.3035576	307.3462346
S14 2019-06-25 08h45m	526.674937	293.5801571
S14 2019-06-25 09h00m	541.8578301	277.9149989
S14 2019-06-25 09h30m	538.0194698	284.9348718
S14 2019-06-25 10h00m	543.8436362	261.5517894
S14 2019-06-25 10h30m	540.6247514	255.1340054
S14 2019-06-25 11h00m	542.8284826	295.4913175
S14 2019-06-25 11h15m	543.8931411	277.5454562
S14 2019-06-25 11h30m	542.7651896	259.7593864
S14 2019-06-25 11h45m	547.8565197	258.5955391
S14 2019-06-25 12h00m	547.5414654	242.2170323
S14 2019-06-25 12h15m	536.3721254	250.5811238
S14 2019-06-25 12h25m	547.8860391	238.8827435

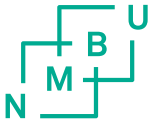

Norges miljø- og biovitenskapelige universitet
Noregs miljø- og biovitskapelege universitet
Norwegian University of Life Sciences

Postboks 5003
NO-1432 Ås
Norway